POLITECNICO DI TORINO

Collegio di Ingegneria Chimica e dei Materiali

Master of Science Course
in Materials Engineering

Master of Science Thesis

Carbon-ceramic composite material characterization for car brake disk application

Thesis supervisors

Monica Ferraris

Stefano De La Pierre Des Ambrois

Candidate

Matteo Fastampa

AY 2023/2024

CONTENTS

LIST OF FIGURES

LIST OF TABLES

1. INTRODUCTION

1.1 AIM OF THE THESIS

This thesis aims to provide a characterization of the properties of composite materials, specifically focusing on studying the mechanical characteristics of innovative brake discs used in the automotive field. An overview of the world of composite materials will be provided, with a specific focus on those with a ceramic matrix reinforced with carbon fibers, such as the CCB (carbo-ceramic brakes) discs developed by BSCCB, which are analyzed in this study. The increasingly prevalent use of composite materials stems from the ability to combine properties of different materials into a single device according to its intended use, and the automotive sector is one of the industries where they are increasingly utilized. The considered discs are made of CMCs (ceramic matrix composites). The matrix is composed of silicon carbide (SiC) while the reinforcing component consists of short carbon fibers. The properties and main production methods of the two components of the brake discs will be described to demonstrate their effectiveness for the intended use. Experimental data from various types of tests will be presented to compare different testing methodologies and validate the nature of the results, as well as study the material's behavior at different temperatures to derive useful information. In the specific case of brake discs, the required properties undoubtedly include considerable resistance to external stresses and temperatures generated during use due to friction between the brake pad and the disc. The materials must allow for good heat dissipation during operation and consequently excellent thermal conductivity linked to good mechanical resistance. All of this must be coupled with as low as possible weight to allow better performance. Especially in racing, weight is a fundamental and impactful factor in vehicle performance.

This thesis will specifically analyze the stiffness of the material composing the brake discs and its evolution based on the temperatures imposed by various tests. In particular, Young's modulus (E) and storage modulus (E') of the material will be evaluated, describing in detail the differences and relationships between them for the material analyzed in this study. The Young's modulus of the material was studied using static tests in frequency, based on an impulse excitation technique (IET), performed using the RFDA HT 1600, and through three-point bending tests conducted with the Instron 5965. The IET tests were carried out at the J-tech laboratory located at the Polytechnic University of Turin. They rely on exploiting the vibration frequencies of the sample to estimate its stiffness, made possible by mathematical relationships derived from specific standards. The tests were conducted at room temperature and also with temperature gradients up to 600 °C. On the other hand, the storage modulus (E') was obtained from dynamic tests both at room temperature and with a temperature up to 250 °C. The Instron 8802 was used for these analyses.

Furthermore, the effectiveness of a customized testing system developed at the BSCCB laboratory (Brembo headquarters in Stezzano) will be demonstrated by comparing the data obtained through its use with those derived from machinery provided by companies in the sector. This experimental method is based on the same principles as the IET technique; that is, the stiffness of the material is obtained from the vibration frequencies caused by an instantaneous impact. The differences lie in the instrumentation used, but the applied setup is derived from the same standards.

Finally, considerations will be made on the experimental data collected, also comparing the results derived from different testing methods.

2. COMPOSITE MATERIALS

2.1 DEFINITION

The precise definition of composite material is still debated, as even various traditional materials could be considered composites. An example is metallic alloys, which are the combination of multiple components to create a unique material with specific properties, such as carbon steel. Another example are copolymers, which consist of different types of polymers blended together. However, the differences between traditional materials and composites can be significant: they consist of two different materials and are often synthesized separately or in different steps before forming the composite; they are the result of design, aiming to achieve a combination of properties that make them perform for the desired end-use.

Composite materials are formed by a "main" phase called the matrix, in which the reinforcing phase is dispersed, often synthesized separately as mentioned earlier, and which can take particulate or elongated forms such as fibers or flakes [1].

The design of a composite material starts with the study of the required properties for the objective and the identification of suitable materials to achieve them. To compare the characteristics of different materials, reference is often made to Ashby maps (**Figure 2.1**), which are graphs where various types of materials are depicted in areas with specific properties.

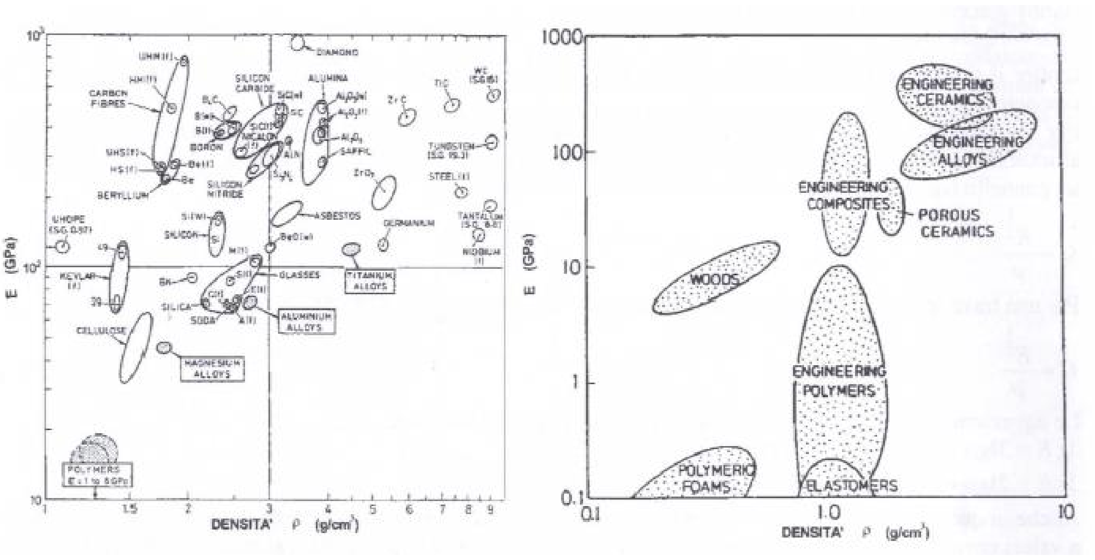

Figure 2.1. Ashby map of Young Modulus and density [1].

In **Figure 2.1**, there is an example of an Ashby map comparing Young's Modulus with material density. Based on the specific modulus value (E/ρ) required by the design objectives, a 45° line representing this value can be plotted in the Ashby map. This line will intersect the various areas representing materials, identifying which materials are equivalent and meet the required specific modulus value. This is just one example, but various properties can be analyzed, such as specific strength, speed of sound wave propagation within the material, thermal conductivity; these are the so-called merit indices related to different properties. The higher the value of the merit index, the more the representation line will be shifted upward on the Ashby map. The slope of the line varies depending on the geometry of the designed element, which also depends in this case on the intended use.

For example, it is possible to obtain the merit index for a lightweight and rigid panel subjected to bending at the center (2.1) through simple calculations on the geometry and the applied stresses:

$$C = \frac{E^{\frac{1}{3}}}{\rho} \tag{2.1}$$

With:

C = merit index

E = Young’s modulus

ρ = Density

While in the case of a rigid beam subjected to bending at the center, the merit index will be:

$$C = \frac{E^{\frac{1}{2}}}{\rho} \tag{2.2}$$

In general, the matrices used are the materials whose properties are desired to be modified or reinforced. They are mainly of three types:

- Polymer matrix (both thermoplastic and thermosetting)
- Metallic matrix
- Ceramic matrix

The reinforcing material can be of different nature, but mainly fiber materials are used, such as:

- Ceramic fibers

- Glass fibers
- Aramid fibers (Kevlar)
- Carbon fibers

In the present study, a ceramic matrix composite with carbon fiber reinforcement will be analyzed.

2.2 CERAMIC MATRIX COMPOSITE (CMC)

Ceramic materials have very important properties derived from the nature of the chemical bonds, which are predominantly covalent or partially covalent ionic bonds. Therefore, they exhibit strong bonds that confer high melting temperatures, high elastic modulus, high hardness, and chemical inertness. These characteristics make ceramics very suitable for applications where high temperatures and strong mechanical resistance are required, such as in the aerospace or automotive sectors. The main drawback of ceramic materials is certainly their low toughness, which is greatly reduced due to their inherently brittle nature. Fracture occurs without plastic deformation, but rather with rapid propagation of a crack until failure.

This is precisely why CMCs have been studied and developed; indeed, the role of the reinforcement is to improve the fracture toughness of the matrix in which it is dispersed, creating a final material that is less brittle. In particular, in SiC/SiC or C/SiC composites, where the dispersed phase consists of fibers of highly resistant materials, fracture toughness values greater than 30 MPa $m^{1/2}$ for the final composite can be achieved, which corresponds to about six times the typical toughness values of the SiC matrix ranging from 3 to 6 MPa m1/2. Below, in **Figure 2.2**, the difference in behavior between a ceramic and a CMC is shown [2].

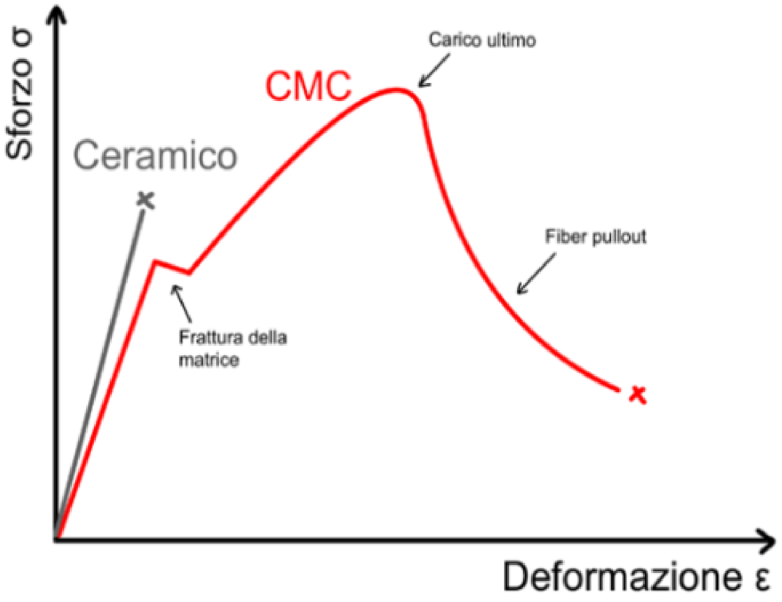

Figure 2.2. Stress-deformation curves for ceramic material vs CMC material [2].

There are several mechanisms that cause this behavior, depending on the fiber-matrix interaction in the composite. In particular, the first step of the fracture mechanism involves the formation of a crack in the matrix. Without the reinforcement, the crack would propagate undisturbed, leading to the typically observed brittle fracture in traditional ceramics. However, the presence of the reinforcement, particularly a fiber, imposes a more tortuous path on the crack, thus imposing a loss in its propagation energy. The crack will then tend to propagate along the fiber-matrix interface, but this is only possible if the interface is weak; indeed, if there is a strong interface bond between matrix and reinforcement, the crack would propagate directly within the reinforcement, promoting brittle fracture and thus undermining the use of the reinforcement itself. This phenomenon is generally called "debonding" and is achieved by applying specific coatings on the fibers; for carbon fibers immersed in SiC, a thin layer of pyrolytic carbon is usually used for this purpose.

As the stress on the system increases further, the fiber will eventually break, leading to "fiber pullout," indicating complete separation of the fiber from the matrix. Below is a schematic representation of the fracture mechanisms in a fiber-reinforced CMC (**Figure 2.3**) [2].

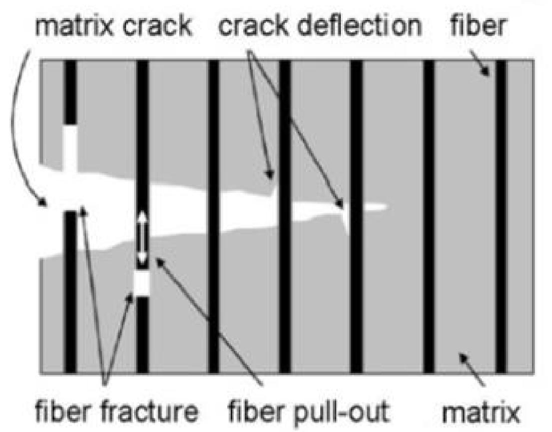

Figure 2.3. Representation of different fracture mechanisms [2].

Traditional ceramic materials are often produced by the combination of a forming phase of the so-called "green" state, which corresponds to the state where the material is still in the form of a powder mixture or a paste containing the material components, and a subsequent sintering phase, which involves densification of the green state towards the final state of the piece. In this phase, high temperatures are reached, which then confer the structure and final properties of the material. To create a ceramic matrix composite, the production processes of ceramic materials can be used, but they are poorly suited to achieve high homogeneity between the matrix and the dispersed phase. For this reason, processes based on matrix infiltration into a preform consisting of the reinforcement have been developed, which is the case for the composite material featured in this study.

In any case, the temperatures developed in the production processes easily exceed 1000°C, and consequently, the reinforcement must also be able to withstand such temperatures. Therefore, not all materials can be incorporated into matrices of this type. Another important element in the production of CMCs (ceramic matrix composites) is the difference between the coefficients of thermal expansion of the matrix and the reinforcement, which must be minimized to avoid the development of residual stresses at the matrix-reinforcement interface, both during production and during operation, which would compromise the performance of the component.

2.2.1 CERAMIC MATRIX – SiC

The ceramic matrices most commonly used in CMCs are alumina, silicon nitride, zirconia, and silicon carbide.

The latter is the primary material constituting the matrix of innovative brake discs that will be analyzed. Silicon carbide is a compound of Si and C atoms, bonded together by covalent bonds with sp3 hybridization to form a tetrahedral structure, schematically depicted in **Figure 2.4** [3].

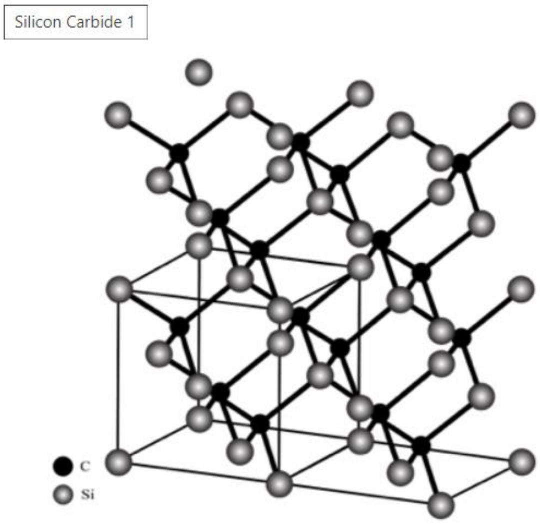

Figure 2.4. SiC crystalline structure [3].

Silicon carbide exists in two possible crystalline structures:

- β-SiC: It has a cubic lattice, with a typical zinc-blende structure, where the basic unit consists of three layers arranged in an ABC sequence.
- α-SiC: This terminology identifies all over 200 polytypes with hexagonal or rhombohedral shapes that can be formed. The constituent layers of the different types of α-SiC have different lengths and stacking sequences depending on the formation conditions and the presence of impurities in the material.

  The simplest form of α-SiC is formed by two layers with an ABAB sequence, resembling the zig-zag structure of wurtzite. The β phase is stable at room temperature until around 2000°C, beyond which the transition to the α phase occurs, which is the most widely used form.

In nature, SiC is not present except in very small quantities in certain types of meteorites found throughout history and is therefore almost entirely produced artificially. The main production methods of SiC are [4]:

- **The Acheson process**: It is the oldest method, involving a solid-state reaction between silica (SiO_2) and carbon derived from petroleum processes (carbon coke) in a furnace heated by graphite resistance heaters, reaching high temperatures (around 2500°C). The reaction is (2.3):

  $$SiO_2(s) + 3C(s) \rightarrow SiC(s) + 2CO(g) \tag{2.3}$$

  The quality of the carbide obtained by this method is generally not high in relation to the energy required. Additionally, the nature of the reaction products depends on the distance from the resistances, leading to the formation of different SiC polytypes. This method is typically used to obtain products used for abrasive or cutting tools where high quality is not required.

- **Physical Vapor Transport (PVT)**: It is an evolution of the Lely method, involving growth mediated by sublimation. In practice, it consists of a system comprising a polycrystalline SiC seed and a substrate in a graphite container where the seed is heated in an inert atmosphere (argon) to about 2500 °C, causing it to sublimate. By subsequently imposing a lower temperature on the substrate, the sublimation products condense on it, leading to the formation of a SiC crystal. Although the final carbide quality is good, limitations such as limited crystal size and difficulty in controlling nucleation speed and modes have led to the development of the PVT method. It is based on the same principles but differs in that the SiC source and growing seed are placed very close together, allowing a true passage of material in vapor form to the seed, governed by the imposed temperature gradient. Additionally, introducing a gas flow into the growth chamber has greatly increased control over nucleation and subsequent crystal development.

- **Chemical Vapor Deposition (CVD)**: This method relies on high-temperature reactions leading to the formation of the desired material from its gaseous precursors inside a chamber where a substrate is placed for growth. Reactions often occur directly on the substrate surface, or sometimes in the reaction chamber atmosphere, with the products being absorbed by the substrate where they diffuse and nucleate. This method allows for a wide range of SiC forms, such as thin films, whiskers, nanowires, and crystals.

- **Sol-gel process**: This process is based on two main steps: hydrolysis and polycondensation. The first step involves creating a silica-glass solution containing alkoxide precursors mixed with water and a solvent. Following hydrolysis and condensation, a silica gel is formed, consisting of very small pores and polymer chains with Si-O-Si bonds. Depending on how the solvent is removed, different structures are obtained. Using a typical drying process causes densification and shrinkage of the material, resulting in a xerogel, whereas removing the solvent under supercritical conditions produces an aerogel, which is a highly porous structure with low density due to minimal densification. Finally, silica reduction is carried out at temperatures reaching around 1600 °C. The quality and properties of the resulting material mainly depend on the types of precursors used and the reduction temperature. Over time, various precursors for silica and different carbon sources for synthesizing SiC have been used. For example, typical silicon precursors used in this context are simple silica (SiO2), tetraethoxysilane (TEOS), and methyltriethoxysilane (MTES). Carbon sources have ranged from sucrose to phenolic resins, ethylcellulose, and polyacrylonitrile (PAN). Generally, after hydrolysis, the sol undergoes gelation and then carbothermal reduction of silica to synthesize SiC. This method allows SiC to be synthesized in various forms. For example, nanoparticles or mesoporous structures can be produced, creating highly reactive structures suitable for catalytic processes or as adsorbents. In general, the sol-gel process tends to create highly porous components due to gas development during the sol drying phase and carbothermal reduction of the gel, resulting in a much lower density than the theoretical density of SiC, which is around 3.2 g/cm3 (typically reaching a maximum density of 1.86 g/cm3).

- **Liquid phase sintering (LPS) technique**: This method involves the fusion of a powder recipe containing varying amounts of α-SiC and β-SiC, along with sintering additives aimed at lowering process temperatures and improving the quality of the final sintered product by enhancing densification and microstructure. Various research efforts over the years have led to the conclusion that using specific oxide additives such as alumina (Al_2O_3) and yttria (Y_2O_3) allows for high densification at relatively low temperatures (1850-2000°C). Additionally, performing LPS in a controlled atmosphere using different gases such as nitrogen or argon influences the final product; for example, with N_2, the transformation between α-SiC and β-SiC is suppressed, while with Ar, the opposite is obtained.

- **Reaction Bonding or Reaction Sintering**: this method is based on the reaction between a solid and other species, which can be liquid, gas, or another solid. In the case of a gas-phase reaction, the solid must have a highly porous structure to allow the reaction and subsequent production of SiC directly within the pores of the preform.
  In the case of reaction bonding with a liquid phase, the process relies on the infiltration of a preform with which the liquid material will then react to form the final SiC structure. Typical of this method is the infiltration of a SiC-C or C preform with molten silicon to create a dense SiC structure (2.4).

  $$Si + C \longrightarrow SiC \qquad (2.4)$$

  This principle is used in the production of disks for braking systems made of carbon-ceramic material with a SiC matrix, which are the focus of this research; in this case, the preform is made up of short carbon fibers arranged randomly and porous carbon to form a disk that is then infiltrated with molten silicon. The reaction between silicon and the carbon in the preform will result in the SiC matrix. The entire process will be specifically addressed in Chapter 3.

Focusing on the main properties of SiC, below are images of graphs comparing the main characteristics of various materials, including SiC (**Figure 2.5-2.9**) [5].

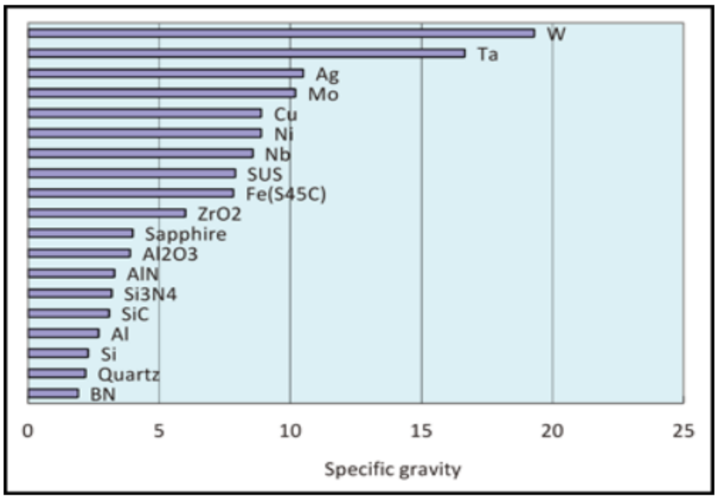

Figure 2.5. Specific gravity of different materials [5].

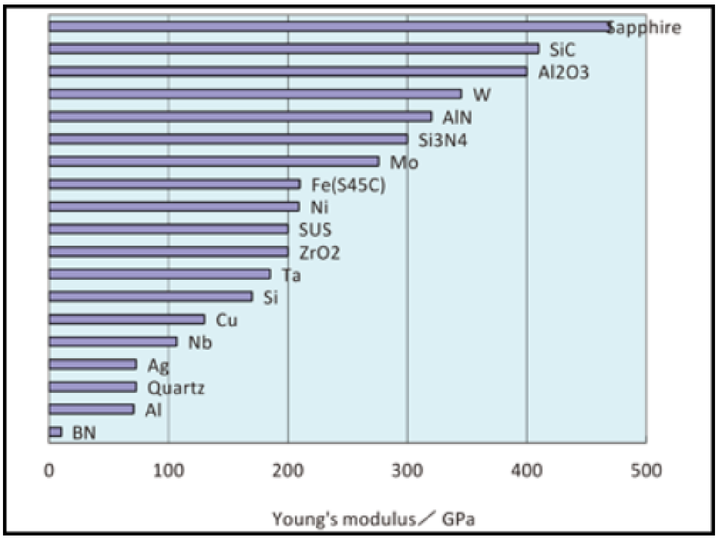

Figure 2.6. Young’s Modulus of different materials [5].

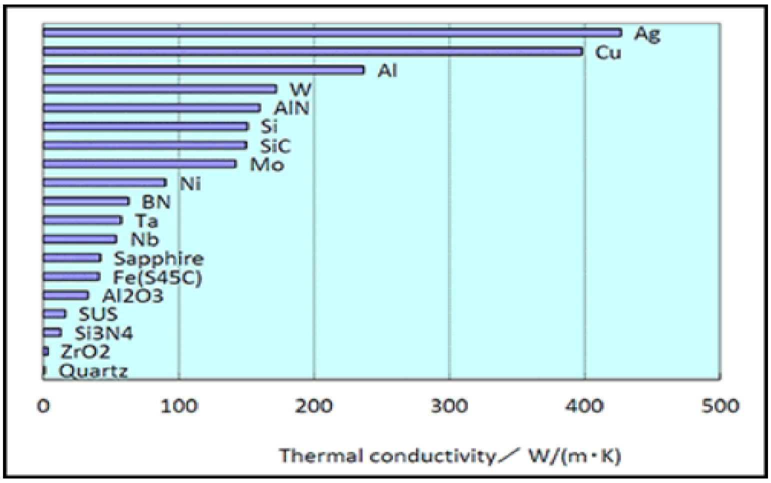

Figure 2.7. Thermal conductivity of different materials [5].

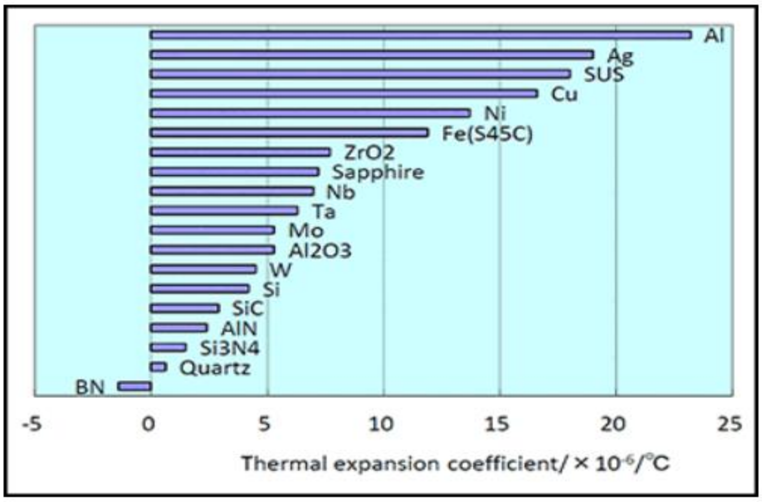

Figure 2.8. Thermal expansion coefficient of different materials [5].

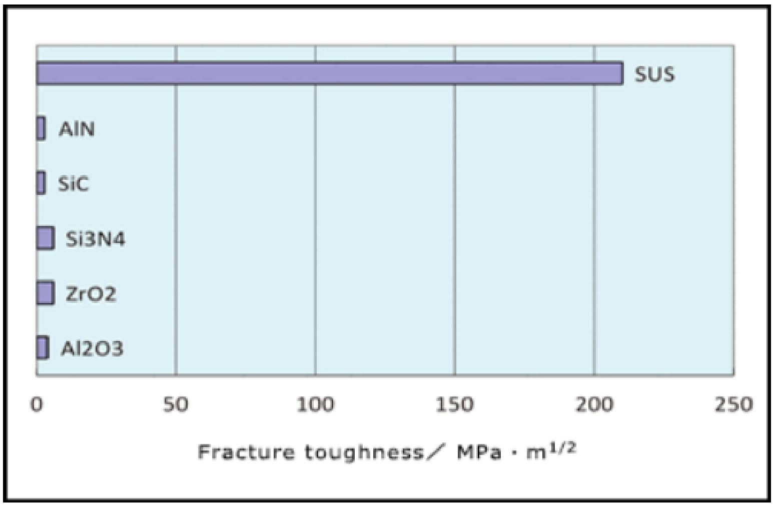

Figure 2.9. Fracture toughness of different materials [5].

As can be seen from the presented graphs, SiC manages to combine very high thermomechanical properties such as a high Young's modulus, excellent thermal conductivity, with a much lower density compared to many metallic materials. This makes this material suitable for working in areas where high operating temperatures are required in combination with high strength. In addition, it guarantees these properties with a low density (around 3.2 g/cm^3), which is crucial in the automotive sector, especially for braking systems of high-performance vehicles, where weight is a determining factor. From the graph in **Figure 2.8**, it is also noticeable that SiC also possesses a relatively low coefficient of thermal expansion, especially compared to metallic materials, an important characteristic for the brake discs under consideration as it is necessary to maintain the geometric characteristics during operation and also to avoid developing excessive residual stresses both on the braking system and within the composite material itself between the SiC matrix and the carbon fiber reinforcement.

The most critical characteristic of silicon carbide is its low toughness, as can be seen in **Figure 2.9**, which is why SiC matrix are often reinforced with carbon fibers to help improve this aspect.

2.2.2 REINFORCING MATERIAL – CARBON FIBER

The reinforcing phase can vary in nature and form, but the most commonly used in composite materials structure is the fiber. Specifically, carbon fibers are gaining increasing importance in this field due to their high properties, especially in applications requiring high mechanical strength even at high temperatures.

The properties of carbon fibers depend closely on the manufacturing process, and for this reason, a wide range of fibers can be synthesized [1]:

- UHM (ultra-high modulus): with Young's modulus values exceeding 500 GPa.
- HM (high modulus): having E > 300 GPa and a tensile strength-to-modulus ratio of less than 1%.
- HT (high tensile strength): specialized to provide tensile strengths greater than 3 GPa and a strength-to-modulus ratio between 1.5 and 2%.
- IM (intermediate modulus): with modulus values below 300 GPa and a strength-to-modulus ratio greater than 1%.
- LM (low modulus): with modest modulus values (around 100 GPa).

In any case, carbon fibers are composed of structural units based on graphite. Graphite is one of the allotropes of carbon that is stable under standard environmental conditions. The typical graphite structure consists of graphene sheets bonded together by weak van der Waals bonds (**Figure 2.10**) [6].

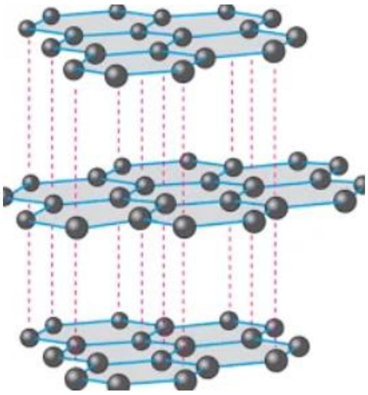

Figure 2.10. Schematic structure of graphite [6].

Each layer is formed by carbon atoms covalently bonded together to form hexagonal meshes with each one sp2 hybridized. The unhybridized electron, which is delocalized in the p orbital, accounts for the high electrical conductivity of graphite.

The mixed nature of the bonds holding the graphite structure together makes the material highly anisotropic. The van der Waals bonds between graphene layers make the material weak to shear stresses or transversal to the fiber axis, whereas the covalent bonds within the individual layers impart high tensile and compressive strength perpendicular to them.

Carbon fibers can be synthesized from three main precursors: cellulose or rayon fibers, pitch, or PAN (polyacrylonitrile). The production from cellulose fibers has been quickly replaced by processes based on PAN and pitch as the latter yield fibers with better properties.

Starting from pitch, a carbon-rich material derived from petroleum refining, fibers with high modulus, reaching even beyond 800 GPa, and variable tensile strength between 1000 and 3000 MPa can be obtained. The production steps from pitch are as follows:

- Heating to between 300 and 500°C to obtain the so-called mesophase pitch, a structure with a liquid crystalline order. Additionally, mesophase pitch is spun to align the lamellae along the fiber axis.
- Oxidation of mesophase fibers at 250-350°C.
- Carbonization treatment at approximately 2000°C.
- Final graphitization at temperatures ranging from 2500 to 3000°C.

On the other hand, carbon fibers derived from PAN tend to have lower modulus but higher strength. PAN is a linear atactic polymer obtained from the polymerization of acrylonitrile and the base chemical formula of polyacrylonitrile (PAN) is represented below (**Figure 2.11**) [7].

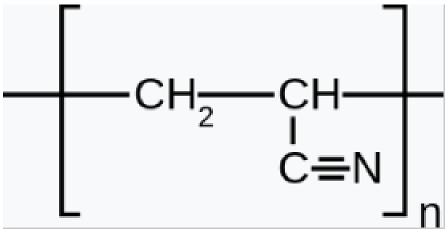

$$\left[-CH_2-\underset{\underset{C\equiv N}{|}}{CH}- \right]_n$$

Figure 2.11. Chemical structure of polyacrylonitrile [7]

The transformation process of PAN into carbon fibers also involves several phases [8]:

- **Heating up to 300-400°C**, during which the triple bond between carbon and nitrogen breaks, resulting in a ring structure (**Figure 2.12**).

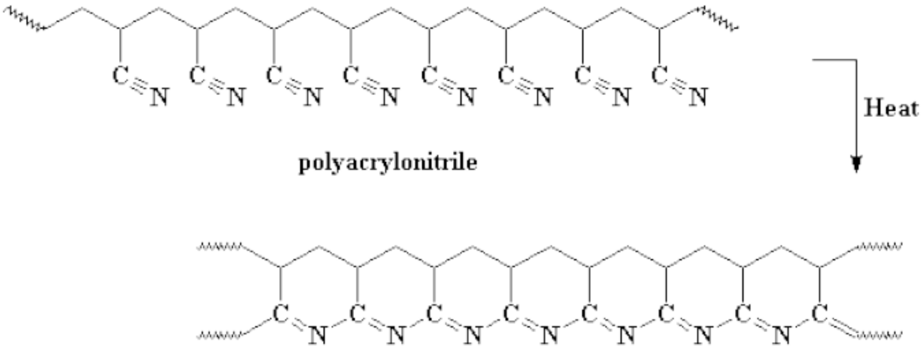

Figure 2.12. Schematic view of the first step of heating in carbon fiber production from PAN [8].

- **Oxidation**, conducted in air or oxygen at temperatures ranging from 200 to 250 °C, resulting in a structure formed by aromatic rings due to dehydrogenation, i.e., hydrogen release following the breaking of C-H bonds (**Figure 2.13**). This step renders the polymer more thermally stable, preparing it for subsequent heat treatments.

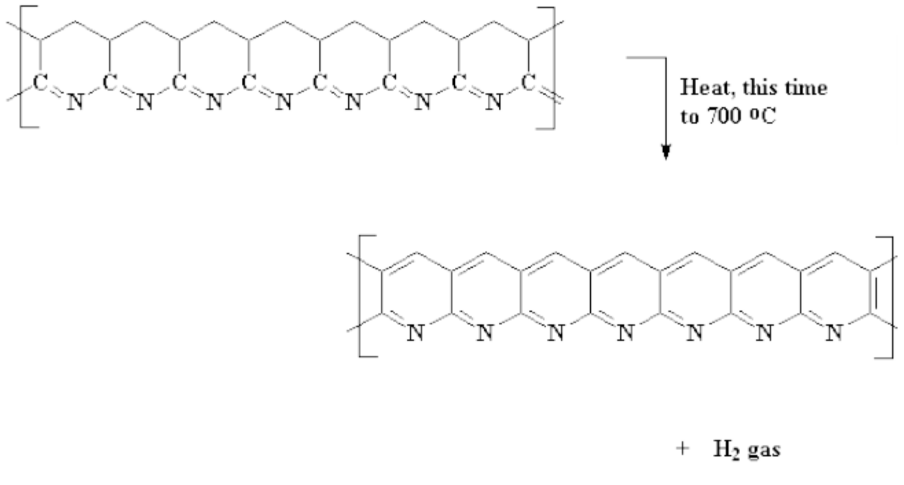

Figure 2.13. Schematic view of oxidation step in carbon fiber production from PAN [8].

- **Carbonization phase**, which can occur in two steps, both operated in an inert atmosphere:

  1st step: heating between 400 and 600 °C causes the aromatic chains formed in the previous phase to join together, leading to the expulsion of gaseous hydrogen atoms. The structure after this process is a ribbon polymer with chains that only have nitrogen atoms at the ends (**Figure 2.14**).

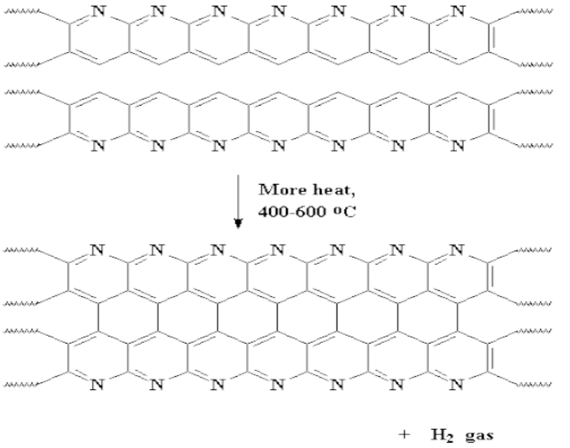

Figure 2.14. First carbonization step of PAN [8].

  2nd step: The temperature is increased up to 1500 °C to promote the expulsion of nitrogen atoms and the fusion of additional aromatic chains to increase the size of the structure, eventually forming a graphite-like structure (**Figure 2.15**).

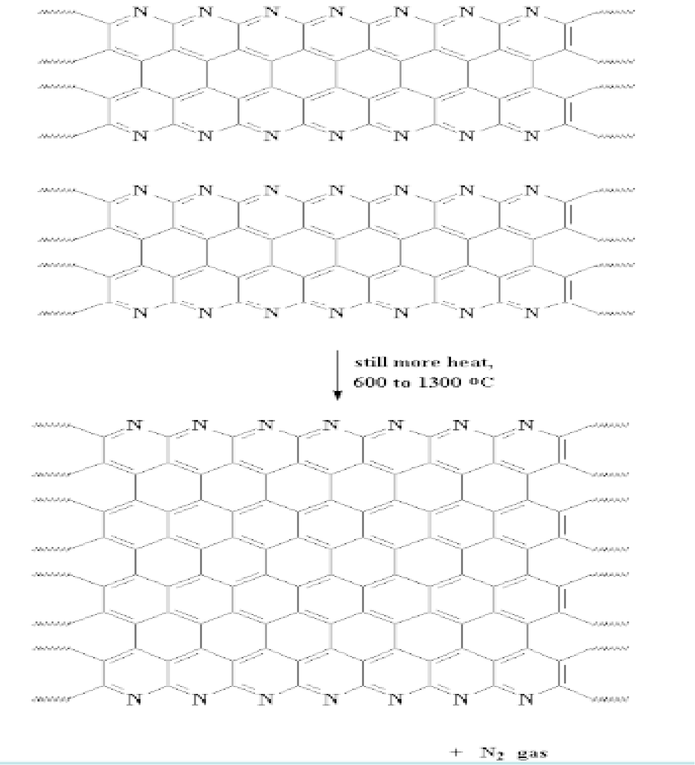

Figure 2.15. Second carbonization step of PAN [8].

- Final **graphitization phase**, in which the fibers are subjected to heat treatment in an inert atmosphere up to approximately 2800 °C while applying tensile stress. This phase promotes the orientation of aromatic rings along the fiber axis, significantly increasing tensile strength and Young's modulus. An increase in the process temperature leads to greater orientation and a higher Young's modulus, but at the same time, it tends to decrease tensile strength.

Following the production process, fibers with crystalline structures are obtained, with the hexagonal planes of graphite randomly oriented relative to each other, resulting in a non-ordered lamellar structure.

The composite material under study consists of short carbon fibers derived from the conversion of PAN.

2.2.3 PRODUCTION PROCESSES OF C/SiC COMPOSITES

Ceramic matrix composite materials can be produced using manufacturing processes that mimic those used for the creation of classic ceramic materials [1]. For example:

- Powder sintering: This method involves the mixing of matrix and reinforcing powders followed by subsequent pressing and densification through firing. The issue with this production method is the final homogeneity of the composite, as simple mechanical mixing may not achieve a uniform dispersion of reinforcing particles within the matrix.

- Slurry-based sintering: Starting with a suspension of matrix and reinforcing particles, this method involves mechanical mixing and agitation to more evenly disperse the two components (homogenization phase). Subsequently, the solvent is removed, either through simple drying or slip casting, which involves pouring the solution into a draining material mold (such as gypsum). Finally, pressing and sintering phases, which can occur simultaneously, take place. The use of a suspension of matrix and reinforcing powder instead of simple dry powder mixing, as in the previous method, significantly improves the homogeneity and uniformity of the final composite.

- Sol-gel method: This method, as described previously for the production of SiC, involves using a sol with matrix precursors to impregnate a preform made of the toughening agent or disperse reinforcing particles in the sol to obtain a mixture of toughening agent and matrix particles after removing the solvent.

- Infiltration: In this method, a porous preform made of the reinforcing material is infiltrated with a precursor of the matrix, creating the final matrix through chemical reactions that surround the reinforcing material, forming an interface with it. The matrix precursor can be in either gas or liquid phase.

Focusing on SiC-based composites with carbon fiber reinforcement, the most commonly used methods for their production are based on infiltrating a preform consisting of fibers with liquid, solid, or gaseous SiC precursors. The main methods are three:

- **Polymer impregnation and pyrolysis (PIP)** [9]: A porous preform made of carbon fibers is infiltrated by polymeric precursors of the ceramic matrix in solid or liquid phase, which upon heat treatment decompose and promote SiC formation. The main phases of this process typically include:
  1. Preform fabrication with fibers.
  2. Preform impregnation by precursors.
  3. Consolidation phase: the preform is immobilized in a specific mold, and heating is carried out up to softening and crosslinking temperatures of the precursor, assisted by unidirectional pressure.
  4. Pyrolysis phase: the sample resulting from consolidation undergoes pyrolysis treatment in an inert atmosphere and at high temperatures, usually around 1100-1200°C, where the final SiC matrix is formed.
  5. Repetition of the infiltration and pyrolysis cycle: multiple infiltration and subsequent pyrolysis phases are needed to densify the matrix and fill all the preform's pores until the composite's overall weight increases by more than 1%.

  Typically, between the first and second steps, a coating is applied to the preform fibers to facilitate subsequent interaction with the forming SiC matrix and improve the composite's properties, which are closely related to the matrix-reinforcement interface. The most commonly used precursors for SiC matrix are polycarbosilane (PCS), polymethylsilane (PMS), or the more recent low molecular weight polycarbosilane (LPVCS). Adjusting the precursor mixture and pyrolysis temperature regulates the final characteristics of the composite, with higher process temperatures achieving a better level of matrix crystallinity and overall superior properties. This method is advantageous for large-scale component production, including complex shapes, and for process cost-effectiveness. However, disadvantages lie in the final quality of the composite, which tends to be low density with an amorphous matrix.

- **Chemical vapor infiltration (CVI)** [1]: this method involves infiltrating a porous preform consisting of reinforcing fibers with gaseous precursors of the SiC matrix, which react to produce the final matrix material. Three types of CVI have been developed based on the infiltration conditions, as depicted in **Figure 2.16**.

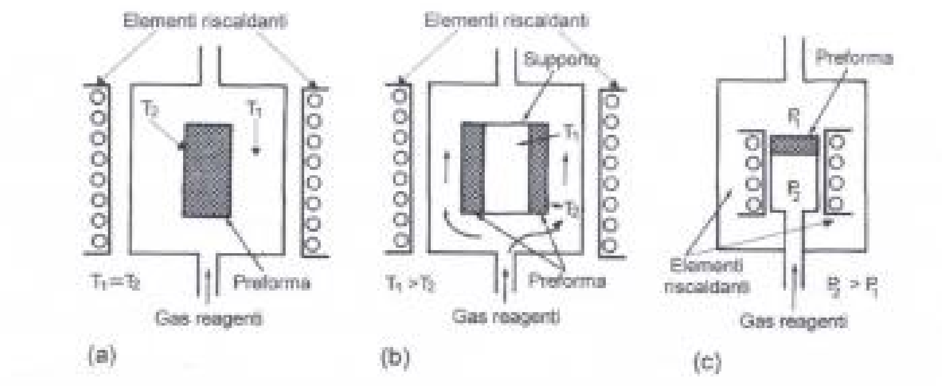

Figure 2.16. CVI processes: (a) Isothermic CVI; (b) Temperature gradient CVI; (c) Pressure gradient CVI.

a) Isothermal CVI: This method involves applying a temperature of approximately 1100°C and a pressure between 5 and 50 Torr. In this case, attention must be paid to the amount of deposition that occurs on the sample, as it can obstruct the entry of pores in the preform, preventing their complete filling. Therefore, it is necessary to periodically interrupt deposition and remove the surface material that blocks the pores.

b) Temperature gradient CVI: The preform to be infiltrated is brought into contact with heated support, creating a temperature gradient between the contact area, which will be hotter and thus cause a higher deposition rate of the reaction product compared to the non-contact zone. This results in a direction of infiltration and deposition dictated by the temperature gradient.

c) Pressure gradient CVI: In this case, a preferential infiltration direction is created thanks to a pressure gradient established within the preform between two faces in contact with environments at different temperatures.

Regarding the production of the SiC matrix with this method, a mixture of trichloromethylsilane (MTS - CH_3 $SiCl_3$) and hydrogen is typically used as a precursor. Although CVI yields high-quality composites, it undoubtedly requires a more significant economic effort compared to the previous PIP method.

- **Liquid silicon infiltration (LSI)** [1]**:** this method follows similar principles as the previous ones, relying on infiltration, but the difference lies in the precursor used, which is simply molten silicon, a material that is very economical and easy to obtain. Initially, a component is created consisting of a carbon fiber preform with a porous carbon matrix formed using PIP or CVI techniques. This component is then infiltrated by molten silicon, which has a very high temperature (above 1400 °C), interacting with the carbonaceous matrix and reacting to create SiC, which becomes the new final matrix of the composite. This method, besides being quite economical, allows the production of composites with low residual porosity but of slightly lower quality compared to PIP and CVI techniques.

The following table (**Table 2.1**) shows the different impacts of the various previously described techniques on the final properties of the composite [1].

Table 2.1. Properties of C/SiC composites (Carbon fiber-reinforced silicon carbide matrix) produced using different methods [1].

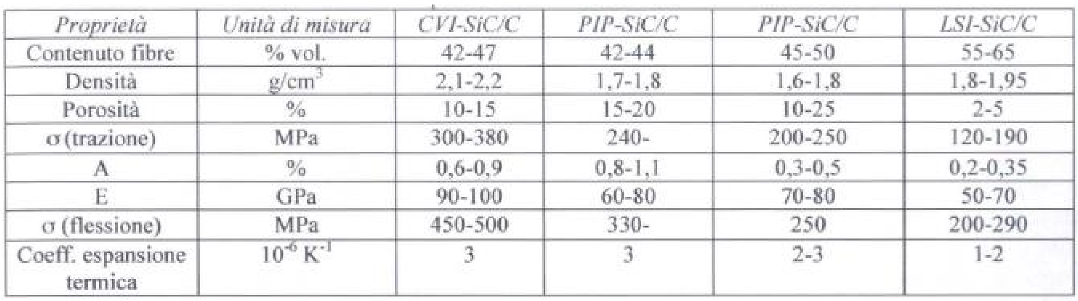

Proprietà	*Unità di misura*	*CVI-SiC/C*	*PIP-SiC/C*	*PIP-SiC/C*	*LSI-SiC/C*
Contenuto fibre	% vol.	42-47	42-44	45-50	55-65
Densità	g/cm^3	2,1-2,2	1,7-1,8	1,6-1,8	1,8-1,95
Porosità	%	10-15	15-20	10-25	2-5
σ (trazione)	MPa	300-380	240-	200-250	120-190
A	%	0,6-0,9	0,8-1,1	0,3-0,5	0,2-0,35
E	GPa	90-100	60-80	70-80	50-70
σ (flessione)	MPa	450-500	330-	250	200-290
Coeff. espansione termica	10^{-6} K^{-1}	3	3	2-3	1-2

The data in the table are only indicative, as the mechanical properties of CMC materials are highly dependent on the specific microstructure and also on the geometric characteristics.
The brake discs under study are produced using the LSI method.

3. BRAKE DISKS

3.1 CHARACTERISTICS OF A BRAKING SYSTEM AND BRAKING CONDITIONS

Throughout the history of automotive engineering, two types of braking systems have followed one another: drum brakes and disc brakes. Nowadays, the former has become obsolete, making way for disc brakes. The typical braking system used today consists of [10]:

- Brake caliper
- Piston(s) and related seals
- Brake disc
- Brake pads
- Brake fluid

In a wheeled vehicle, the purpose of the braking system is to convert kinetic energy into thermal energy by applying force between the brake pads and the brake disc. The braking force originates from the brake caliper, which is powered by one or more pistons connected to a hydraulic circuit containing brake fluid. The brake fluid serves to amplify the pressure exerted by the driver on the brake pedal. The caliper then converts this pressure into force, pushing the brake pads against the disc. Therefore, the interaction between the pad and the disc is crucial, making the selection of suitable materials essential. Two elements are central during braking, closely related to each other: the coefficient of friction between the pads and the disc, and the temperature generated due to frictional forces. In particular, the coefficient of friction tends to decrease with temperature, making braking less efficient. This is the so-called "fading" phenomenon. Experimental data indicate that the coefficient of friction typically remains constant until about 350°C before decreasing with increasing temperature (see **Figure 3.1**).

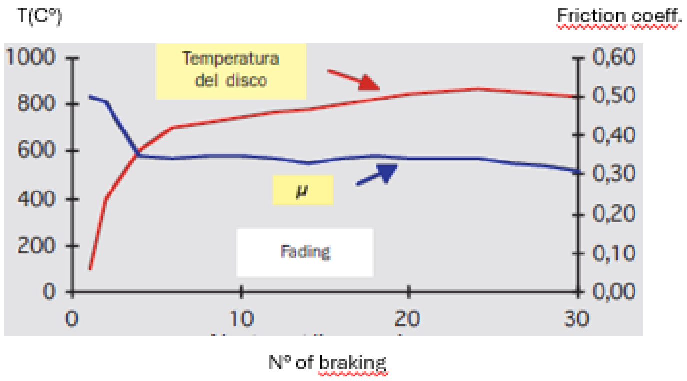

Figure 3.1. Friction coefficient (μ) and temperature with increasing number of brakings [10].

Of course, this depends on the materials used both in the disc and in the pads. Considering this, it is important that the disc is able to dissipate heat very easily. This is ensured both by the intrinsic properties of the disc and in particular by the thermal conductivity of the material used, and by the structure of the disc. To get an idea of the energies involved, a practical example can be showed [10]. With the following braking conditions:

- Vehicle weight at full load = 1560 kg
- Front/rear distribution = 56%
- Radius under load = 27.5 cm
- Disc diameter = 238 mm
- Pad surface area = 35 cm2
- Vehicle speed = 150 km/h
- Deceleration during braking = 0.6 g

The following values are obtained:

- Arrest time = 7.05 s
- Thermal power released at the beginning of braking = 106.6 kW
- Thermal energy released in 7 seconds = 377 kJ, equivalent to 90.2 kcal

The reported thermal power is relative to the first moments of braking; subsequently, it will decrease linearly. In any case, these are very important thermal energies, of which it has been seen that 80% is absorbed by the disc rather than by the pad, confirming the fundamental role of the disc in braking efficiency.

Therefore, the structure of the disc is of vital importance, especially the shape, which influences thermal dissipation. In general, a disc is composed of:

- The friction surface: it is the surface on which the pads rub, which is sized according to the desired braking power.
- The bell area: it is the central part of the disc where there are holes that allow the passage of screws used for screwing onto the hub and wheel fastening bolts.

If the energies and temperatures involved are low, the simple airflow imposed by the disc motion is sufficient to ensure adequate heat dissipation. But if the energies at play are very high, as in the case of high-performance vehicles, it is necessary to impose additional ventilation by creating cavities within the disc itself; these are the so-called ventilated discs. Ventilated discs are brake discs composed essentially of two surfaces connected by bridges arranged in various ways that create ventilation ducts between the central and peripheral parts of the disc; these are the fins. In **Figure 3.2**, a sectional view shows the difference between a ventilated and a solid disc, and a representation of a ventilated carbon-ceramic disc.

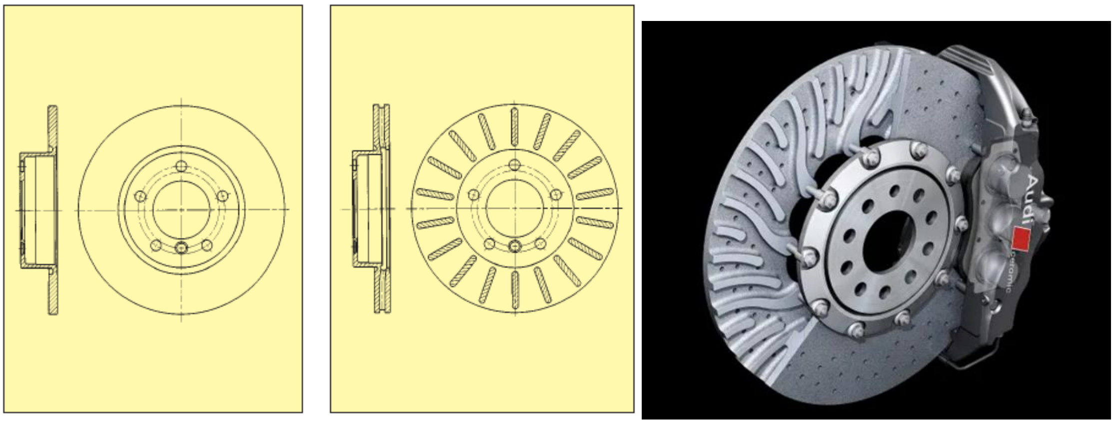

Figure 3.2. Section of a full disk (left); section of a ventilated disk (center) [10]; an example of carbon ceramic disk (right) [11].

In addition to having good properties in terms of heat dissipation, the disc must be able to withstand the typical loads of braking. Referring back to the numerical example previously proposed and performing some calculations, the stresses experienced by the disc are as follows:

- Stresses due to centrifugal force = 0.73 N/mm^2
- Compression force per pad = 7193 N
- Compression stress = 2.05 N/mm^2
- Braking force at the center of pressure = 7182 N
- Tensile stress due to friction = 12.2 N/mm^2, equivalent to 12.2 MPa

Neglecting the compression stress imposed by the pad and the stresses due to the centrifugal force of the disc, the most significant stress component is the tensile stress. The friction induced by the pad-disc contact induces a tensile stress, which in this case is around 12 MPa, which must be compared with the tensile strength of the material composing the discs; for example, cast iron has a tensile strength of approximately 200 MPa.

Therefore, in conclusion, a brake disc must possess the following properties:

- Excellent thermal dissipation capacity and resistance to high temperatures
- High mechanical strength.
- Low strength-to-density ratio: hence, materials with low density and high mechanical strength are preferred.
- High wear resistance.

The most commonly used materials in this field that guarantee these properties are gray cast iron, carbon, and carbon-ceramic composites.

3.2 FROM IRON TO CARBON CERAMIC DISKS

The most commonly used material for disc brakes is undoubtedly cast iron. It is an iron-carbon alloy with a carbon content exceeding 2%. During cooling, zones form in which carbon particles precipitate, which can either form small clusters (nodular or spheroidal cast iron) or lamellae (lamellar cast iron). The latter structure is also called gray cast iron (**Figure 3.3**) and is primarily used for the brake discs of common automobiles.

Figure 3.3. Picture of a common gray cast iron internal microstructure [10].

The properties of gray cast iron have proven to be suitable for application in brake discs because this material exhibits excellent tensile strength, ranging from 200 to 250 MPa, high hardness, ranging from 170 to 250 HB (Brinell hardness) [10], and an elastic modulus of around 200 GPa, accompanied by good thermal conductivity, approximately 50 W/mK [12].

The main issue with gray cast iron is that this material does not provide high resistance to fading, meaning that the friction coefficient supplied by discs composed of this material tends to decrease once temperatures exceed 200 °C, resulting in decreased braking efficiency. This is why carbon discs have been used in the field of racing cars. In Formula 1, for instance, the high temperatures generated during braking (up to 800 °C) would significantly reduce the friction coefficient in cast iron discs, whereas carbon has the particular property of increasing the friction coefficient with temperature. However, the drawback of pure carbon discs is that their braking efficiency is high only at high temperatures, above 400 °C, which are temperatures rarely reached in normal road use. Therefore, an intermediate solution has been developed, suitable for high-performance and luxury cars: the carbon-ceramic disc.

By using a composite material with a SiC matrix reinforced with carbon fibers, superior hardness, thermal conductivity, mechanical strength, and resistance to fading compared to cast iron are achieved. The main advantage lies in the lower density, which allows for both a lighter braking system (up to 50% less weight compared to cast iron discs) and the possibility of increasing the dimensions of the brake discs (from 330mm to 350-380mm and even 440mm in diameter), thereby providing a larger braking surface and ensuring greater braking power. Additionally, there is a lower coefficient of thermal expansion compared to cast iron, which allows for better geometric stability of the disc, avoiding surface deformations that could lead to improper pad-to-disc contact [13].

Brembo SGL Carbon Ceramic Brakes (BSCCB) is one of the world's leading companies in the production of carbon-ceramic discs. The main types of discs produced by BSCCB are two: CCB (Carbon Ceramic Brakes) and CCM (Ceramic Composite Material).

The CCB is produced at the Brembo plant in Meitingen, Germany, while the CCM is produced in Stezzano, Italy. Both types are composed of a composite material with a SiC matrix and carbon fibers as reinforcement. The main difference between the discs is the presence of a protective layer of material, composed of approximately 20% silicon and 80% SiC, on both sides of the disc in CCB. Furthermore, they differ in terms of the average carbon fiber content, with CCB ranging from 46% to 56%, while for CCM, it ranges from 52% to 62%. They also differ in the shape and arrangement of the vanes and thus in the structure of the ventilation system. However, both undergo an anti-oxidation treatment using phosphate salts, which provide greater resistance to oxidation, especially for carbon fibers. Without this treatment, oxidation of the carbon fibers would begin at around 350/400 °C, leading to the conversion of carbon into carbon dioxide and consequent weakening of the composite.

In this study, samples from CCB brake discs without applied antioxidants were analyzed.

3.3PRODUCTION PROCESS OF CARBON CERAMIC BRAKE DISKS

3.3.1 ELEMENTS OF THE PROCESS

The production of carbon ceramic discs is based on the Liquid Silicon Infiltration (LSI) process discussed earlier, and it requires three main ingredients:

- Carbon fibers
- Phenolic resin
- Silicon

The processes and typical characteristics of carbon fibers have already been extensively discussed, so it is appropriate to focus on the other elements of the production process.

Phenol-formaldehyde resin, also known as phenolic resin, is a type of synthetic polymer produced by the reaction between phenol (an aromatic alcohol derived from benzene) and formaldehyde (a reactive gas derived from methane).

In practical industrial processes, phenolic resins are typically manufactured using two main methods. In one approach, an excess of formaldehyde is mixed with phenol in the presence of a base catalyst in an aqueous solution, yielding a low-molecular-weight prepolymer known as a resole. This resole, often in liquid form or solution, can be cured into a solid thermosetting polymer network by, for example, sandwiching it between layers of wood veneer and then subjecting the assembly to heat and pressure to form plywood.

Alternatively, the other method involves reacting formaldehyde with an excess of phenol, using an acid catalyst. This process produces a solid prepolymer referred to as a novolac, which closely resembles the final polymer but possesses much lower molecular weight and remains thermoplastic (i.e., it can be softened by reheating without undergoing chemical decomposition). Curing novolacs typically involves grinding them into powder, mixing them with fillers such as wood flour, minerals, or glass fibers, and then heating the mixture in a pressurized mold. To complete the curing process and transform novolacs into thermosetting resins, additional formaldehyde or compounds that release formaldehyde upon heating are commonly added [14].

In the production process for carbon ceramic discs, novolak phenolic resins are preferred, as they lend themselves very well as a support material to a solid particulate or fibrous structure.

The last ingredient involved in the production process is silicon, which can be obtained by the reduction of silica (SiO_2), readily available in nature, by carbon in electric furnaces heated to over 1900°C using graphite electrodes. The following reaction (3.1) occurs:

$$SiO_2 + 2C \rightarrow Si + 2CO \qquad (3.1)$$

This process yields silicon with a purity level of up to 98%, known as metallurgical-grade silicon (MGS), which possesses sufficient quality for the intended purpose.

3.3.2 PRODUCTION PROCESS

The production process of carbon ceramic brake discs begins with the mixing of phenolic resin powders with carbon fibers in specific ratios. This solid resin-fiber mixture is then introduced into an aluminum mold that replicates the shape of the disc (**Figure 3.4**) [15].

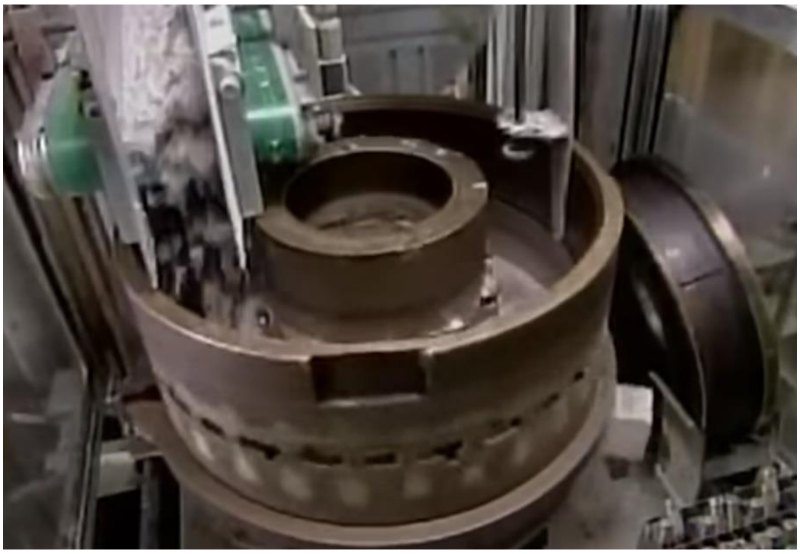

Figure 3.4. Introduction of the resin-fiber mixture into the mold [15].

In the first filling station, the solid mixture is inserted to fill the bottom half of the mold. Subsequently, aluminum pieces are radially arranged in cavities along the circumference of the mold, forming the ventilation channels of the disc (**Figure 3.5**).

Figure 3.5. Insertion of aluminum cores to create the ventilation channels [15].

Once all aluminum pieces are installed, the upper part of the mold is also filled, and the surface is leveled with a rotating cylinder (**Figure 3.6**).

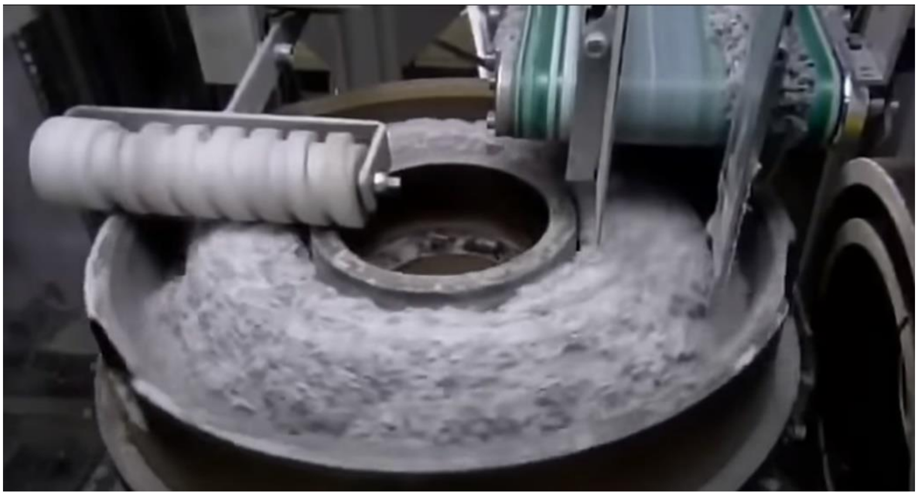

Figure 3.6. Final filling of the mold [15].

And finally, the mold is closed and moved to the next pressing phase. This is carried out using a press that applies a pressure of 2000 kg while heating the mold to 200 °C. Under these conditions, the resin undergoes cross-linking, creating the so-called CFRP (carbon fiber reinforced plastic), which already has the shape of the final disc but is only a preform. The mold containing the CFRP is then extracted from the press and subsequently cooled in cold water for 5 to 8 minutes to allow for the subsequent removal of the aluminum blocks used to create the ventilation channels.

The disc preform is then extracted from the mold, and any imperfections and surface roughness are smoothed before being inserted into a furnace, where it is heated for two hours at a temperature of 1000°C (**Figure 3.7**).

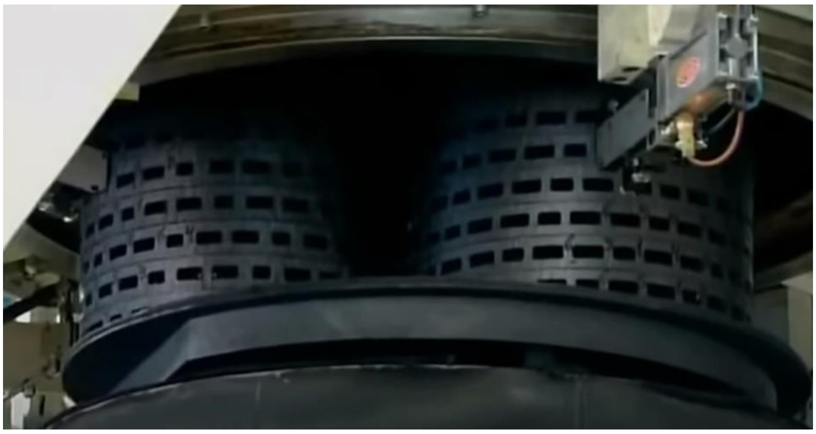

Figure 3.7. Pyrolysis treatment in the oven [15].

In this way, the pyrolysis of the disc occurs, which is the transformation of the chemical structure of the resin into a porous matrix rich in carbon in which the carbon fibers are immersed. Then, the disc is placed inside a crucible made of refractory material (alumina) and is supported by 5 stands to keep it in position (**Figure 3.8**)

Figure 3.8. Alumina crucible used for the silicon infiltration phase [15].

Silicon powder is then introduced into the central cavity of the disc (**Figure 3.9**).

Figure 3.9. Introduction of silicon powder into the crucible [15].

After the crucible is placed in the furnace, it undergoes a 24-hour heat treatment at a temperature of 1700 °C. This process leads to the melting of silicon, which then infiltrates the porous carbon disk and reacts with it, forming a dense SiC matrix.

Following the heat treatment, the disk proceeds to a station where an automated software controls a drilling machine to create ventilation holes on the disk's upper surface, which were previously sealed by the infiltration of liquid silicon.

Subsequently, the disk is immersed in a chamber containing an antioxidation solution to protect the carbon fibers, which are highly susceptible to oxidation once temperatures exceed 400 °C. This oxidation phenomenon could potentially compromise the component's performance (see **Figure 3.10**).

Figure 3.10. Anti-oxidation treatment [15].

Finally, the surface of the disk is polished by an automated robot that brings the disk into contact with rotating strips equipped with an abrasive surface (**Figure 3.11**).

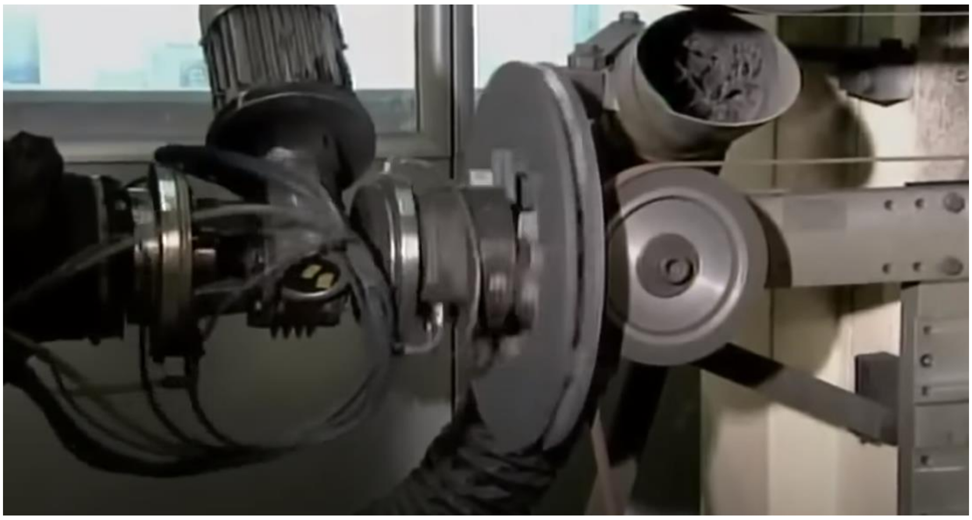

Figure 3.11. Final polishing and refining stage [15].

Before the bell assembly stage, a detailed laser scan is conducted using software to meticulously analyze the disc to ensure its quality. The final product is a high-quality carbon ceramic disc, as exemplified in **Figure 3.12** [16].

Figure 3.12. Carbon ceramic brake disk produced by BSCCB [16].

4. IMPULSE EXCITATION TECHNIQUE (IET)

4.1 INTRODUCTION

The Impulse Excitation technique (IET) consists in analyzing how a test sample or component vibrates after receiving a gentle tap or impulse.

The high temperature unit is a furnace designed for conducting impulse excitation measurements at temperatures up to 1600 °C. Integrated with a Resonant Frequency and Damping Analyser (RFDA, **Figure 4.1**), this setup offers a comprehensive analysis of damping alongside resonant frequencies.

Figure 4.1. RFDA-HT1600 instrument.

Elastic properties of a material are closely related to its mechanical resonance frequencies, while damping, represented by the Q-1 factor, indicates the material's energy absorption.

The RFDA triggers vibrations via mechanical impulses, a method known for its non-destructive test nature, applicable across various conditions like extreme temperatures and controlled humidity. It's even capable of testing specimens amidst thermal shock cycles to gauge the effects of aging.

Maintaining a vibration-optimized environment during measurements is crucial. Therefore, specialized sample holders and furnaces are utilized, equipped with automated impulse excitation devices.

The RFDA HT 1600 software manages the entire measurement process [17].

4.2 MEASURE PRINCIPLE

Vibrations induced by mechanical impulses dissipate energy into a frequency spectrum based on resonant frequencies, which in turn depend on material properties, geometry, and density. Each frequency experiences damping proportional to material energy absorption, influenced by various microstructural factors unique to different material classes.

Transducers detect these vibrations, converting them into electrical signals transmitted to the RFDA's electronic section. After amplification and adjustment, signals are sent to the computer for analysis.

A sophisticated mathematical algorithm developed specifically for this purpose calculates frequencies and damping from the detected spectrum, representing each frequency as a sinusoidal, damped vibration of the form as shown in the following figure (**Figure 4.2**) [17].

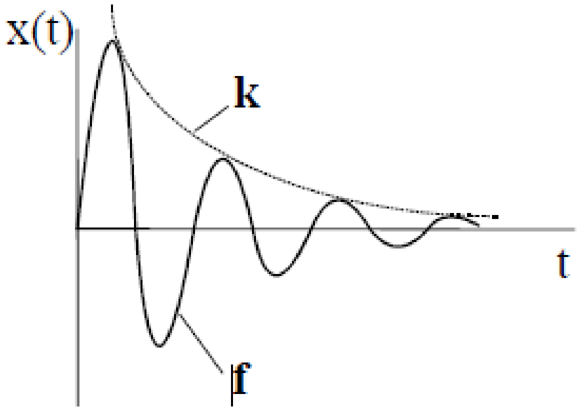

Figure 4.2. Sinusoidal damped vibration; k = Dumping capacity

f = Frequency [17] .

This curve is represented by the following relation:

$$x(t) = Ae^{-kt} \cdot sin(\omega t + \emptyset) \qquad (4.1)$$

With:

k = Dumping capacity

f = Frequency

For each ω the corresponding frequency is calculated as:

$$f = \frac{\omega}{2\pi} \tag{4.2}$$

Examining a specimen's vibration from a damping perspective reveals insights into internal friction mechanisms, such as the rearrangement of crystal defects under stress. This rearrangement dissipates energy in the form of heat and sound, termed damping or mechanical loss.

Damping capacity (k) is contingent upon specimen dimensions, while specific damping is a material property quantifying mechanical loss per unit of energy. The specific damping on the other hand is a material property defined as:

$$Q^{-1} = \frac{\Delta W}{2\pi W} \tag{4.3}$$

This mechanical loss manifests as a relative decrease in the measured vibration signal.

$$Q^{-1} = \frac{1}{\pi}\ln\left(\frac{x_1}{x_2}\right) = \frac{\delta}{\pi} \tag{4.4}$$

where:

x_1/x_2 = ratio of the amplitude of the signal in one period T

δ = the logarithmic decrement

From (4.3) and (4.1) the following equation:

$$Q^{-1} = \frac{kT}{\pi} = \frac{k}{\pi f} \tag{4.5}$$

can be derived.

In this way, the damping, an important property in characterizing the material is easily calculated from the measured damping and frequency.

For a prismatic beam, that is the representing form of the samples tested in this project, there are four vibration modes of interest:

- Out-of-plane flexural
- In-plane flexural
- Torsional
- Longitudinal

In this research we focus on out of plane flexural mode that is strictly dependent on the Young's modulus (E) of the sample. In order to obtain the fundamental frequency for the estimation of Young's Modulus it's important to respect some rules for the setup of the test.

The vibrating modes of a specimen depend on how and where the beam is supported and where the solicitation is applied to the specimen [18].

Focusing on a parallelepiped-shaped specimen, like those tested in the present study, there are specific positions where the natural frequencies (which are the fundamental ones) reach minimum and maximum values, which are respectively the nodes and antinodes. In order to stimulate the fundamental mode of vibration, the specimen needs to be positioned on the support at 0.223 of its length, starting from the ends (node positions), and the excitation needs to be applied at the center of the specimen (antinode position).

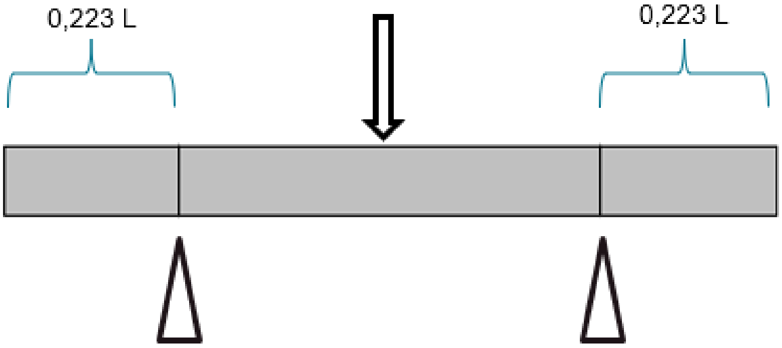

Figure 4.3. Schematic view of nodal position.

With this setup (**Figure 4.3**), vibrations are not significantly influenced by the contact between the specimen and the support. Another precaution is to minimize the contact area between the specimen and the supports, which could increase the damping of vibration frequencies. Furthermore, in order to derive Young's modulus from the frequencies, it's necessary first to identify the peaks of the fundamental frequencies which for a long and thin bar-shaped specimen, are related by these ratios:

1: 2.757: 5.404: 8.933 : 13.344 : 18.638 : .....

Once the fundamental frequency peaks are identified, it is possible to derive Young's modulus using this experimental formula shown in **Figure 4.4**, derived from ASTM E 1876 [19], applicable to a rectangular-shaped bar:

$$E = 0.9465 \cdot \left(\frac{m \cdot f_f^{\ 2}}{b} \right) \cdot \left(\frac{L^3}{t^3} \right) \cdot T_1$$

(ASTM E 1876)

E = Young's modulus, Pa,
m = Mass of the bar, g
b = Width of the bar, mm
L = Length of the bar, mm
t = Thickness of the bar, mm
f_f = Fundamental flexural resonant frequency of bar, Hz
T_1 = Correction factor for fundamental flexural mode to account for finite thickness of bar, Poisson's ratio, etc.

$$T1 = 1 + 6{,}585 \cdot \left(1 + 0.0752\nu + 0.8109\nu^2\right) \cdot \left(\frac{t}{L}\right)^2 - 0.868 \cdot \left(\frac{t}{L}\right)^4 - \left[\frac{8.340 \cdot \left(1 + 0.2023\nu + 2.173\nu^2\right) \cdot \left(\frac{t}{L}\right)^4}{1.000 + 6.338 \cdot \left(1 + 0.1408\nu + 1.536\nu^2\right) \cdot \left(\frac{t}{L}\right)^2} \right]$$

Figure 4.4. Relation for the determination of Young's Modulus for a rectangular-shaped bar based on flexural frequency (ASTM E 1876) [19].

It is noted how the geometry of the sample greatly influences the calculation of the modulus, particularly the thickness which has a cubic impact; therefore, it is necessary to ensure accuracy as much as possible in both the production phase of the sample and in the measurement of the geometric parameters inserted into the calculation software. The correction factor T1 is also strongly dependent on the geometry of the sample, as well as the material Poisson's ratio.

The RFDA HT1600 software automatically calculates E (Young's modulus) based on the detected frequencies using this formula (**Figure 4.4**). Input parameters include the geometric characteristics of the sample being analyzed. For each applied excitation that generates a specific frequency spectrum, the peak corresponding to the fundamental frequency will be chosen, and Young's modulus will then be calculated based on that frequency.

4.3 SET UP AND MACHINE STRUCTURE

To study the material's behavior under impulse loading conditions, various setups were utilized: one external to the RFDA HT1600, referred to as the RT setup (room temperature), and one internal to the machine primarily used for high-temperature tests, denoted as the HT setup (high temperature). The RT setup, depicted in the following image (**Figure 4.5**), consists of a support structure with graduated scales on its sides (**Figure 4.5** (1)), allowing adjustment of the distance between the wires (**Figure 4.5** (4)) serving as supports for the specimen. The wires need to be as thin as possible to minimize the contact area, which increases vibration damping. For this study, Nylon wires were used. As previously mentioned, the wire spacing is determined by calculating the correct position of nodes, which depends on the specimen's length and ensures proper vibration development. Once the specimen is positioned on the wires, a microphone (**Figure 4.5** (2)) is placed above it, at its center. The microphone captures an acoustic signal with a frequency determined by the material's characteristics and sends it to the calculation software. It's crucial for the microphone to not touch the specimen but to be sufficiently close to its surface (1 cm of distance). Impulse loading is induced using an automatic hammer (**Figure 4.5** (3)) connected to the RFDA software, positioned beneath the specimen to apply stress at its center. Through the software, it's possible to set a time interval between successive loading events and adjust the impact intensity based on the specimen's characteristics. Excessive impact intensity could alter the specimen's position, affecting both node spacing and impact point, thus reducing test accuracy. In this analysis, an intensity value of 40% was chosen after repeated tests.

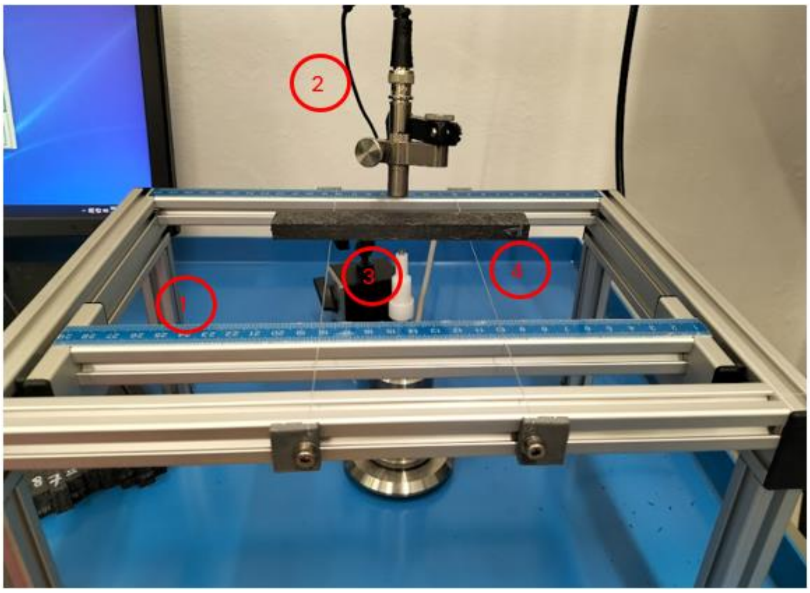

Figure 4.5. IET set-up for room temperature tests (RT set-up); (1) graduated scales, (2) microphone (3) automatic hammer (4) wires.

The second setup is within the RFDA HT1600 [17] and was used both for room and high-temperature specimen analysis. In this thesis, it is named HT set-up to better distinguish it from the RT set-up.

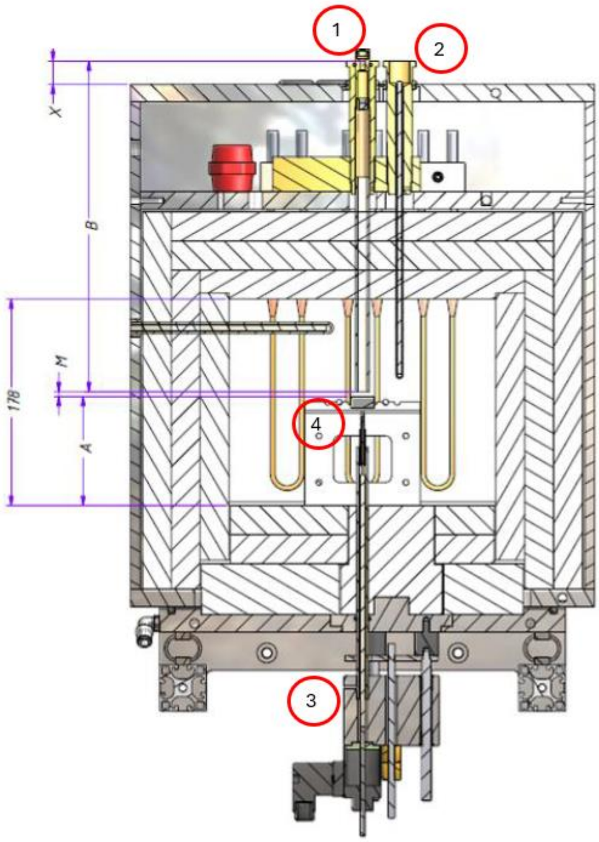

Figure 4.6. RFDA HT1600 schematic view of the furnace chamber; (1) microphone, (2) thermocouple (3) load cell (4) alumina-based support structure [17].

The specimen is placed on an alumina-based support structure (**Figure 4.6** (4) and 4.7) designed to withstand high temperatures. The alumina supports must only be in contact with the specimen at the nodes. Additionally, to reduce the contact area between the specimen and supports, thin steel wires were wrapped around the alumina support cylinders as shown in **Figure 4.7** (left).

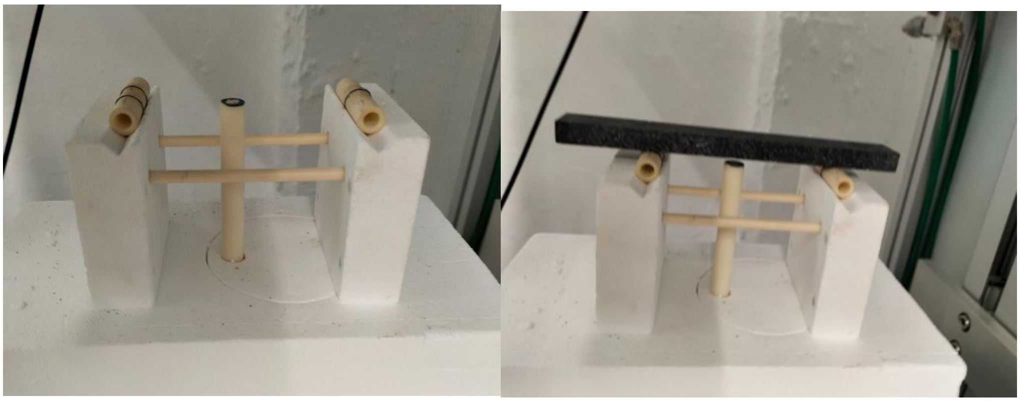

Figure 4.7. Support system of RFDA HT1600 with alumina cylinders .

At the center of the support structure, there is the solicitation system. In **Figure 4.7** it's possible to notice the alumina bar that protects the system used to hit the sample. They are linked to the load cell that is located under the support plane (**Figure 4.6** (3)). In Figure 4.8 it is possible to see the solicitation system and its components. The height of the bar has to be regulated depending on the structure and specimen used in the analysis.

Figure 4.8. Solicitation system in situ (left) and the single components of the solicitation system: load cell, loading projectile, and alumina guide (right) [17].

The entire support platform is movable and moving it upwards shifts the entire system inside the heating chamber. The chamber comprises internal resistors (**Figure 4.6** (4)) along its side walls for heating, a microphone (**Figure 4.6** (1)), and a thermocouple (**Figure 4.6** (2)). The microphone is housed within an alumina guide (**Figure 4.9**) to protect it from high temperatures and the thermocouple (**Figure 4.10**) is fundamental for controlling and regulating the chamber temperature.

Figure 4.9. Alumina guide inside which the microphone is inserted [17].

Figure 4.10. Thermocouple [17].

The positions of the microphone and thermocouple are related to the geometry of the chamber and the specimen that has to be tested. It is possible to regulate their position screwing or unscrewing the fixing bolts on the top of the chamber (**Figure 4.11**).

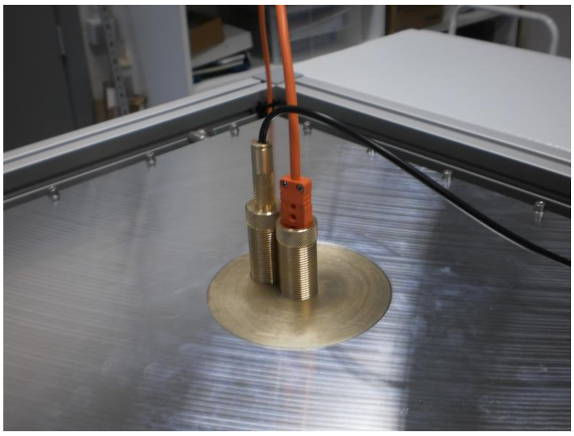

Figure 4.11. Fixing bolts of the microphone (black wire) and thermocouple (orange wire) [17].

The right positions are based on the specimen dimensions using relationships provided in the RFDA manual that are reported hereafter.

Specifically, for the thermocouple:

$$Y = A+C+T-363 \text{ (mm)} \tag{4.6}$$

Meanwhile for the microphone is:

$$X = A+B+M-363 \text{ (mm)} \tag{4.7}$$

Whit:

X = distance to set with adjustment (distance between the top of microphone brass mounting rod and the top cover of the furnace)

Y = distance to set with adjustment (distance between the top of thermocouple regulator and the top of the furnace)

A = distance between the top of the sample and the sample holder

C = total length of the used thermocouple pipe (= 284 mm)

T = required distance between thermocouple and sample (4 – 6 mm)

B = total length of the used signal pipe (= 289 mm)

M = required distance between signal pipe and sample (4 – 6 mm)

Once everything is adjusted and the chamber is closed, it's possible to create the desired analysis conditions. If the aim is making a hot temperature analysis it’s important to create a thermal profile and set the time interval between successive loading events and their intensity using the RFDA HT software. This enables conducting IET tests at high temperatures that are crucial for studying material stiffness evolution in various environmental conditions and, in the case of materials used in heat-generating applications, assessing their performance in situ.

This set up was also used for conducting room temperature tests.

4.1 EXPERIMENTAL TESTS

4.4.1 ROOM TEMPERATURE TEST (RT)

Once the analysis system used has been detailed, the tests performed using this machine will now be specified. The tested samples were obtained from plates produced for research purposes and made of the same material as the brake discs designed and developed by Brembo spa. The plates from which the specimens derive differ from the real brake disc material composition due to the absence of antioxidant and friction layer. In the course of this study, two types of plates and two types of samples will be observed. Some plates have a thickness of 10 mm, from which 9 samples measuring 160x20x10 mm were obtained (**Figure 4.12**, left), while other plates have a thickness of 12 mm, from which 6 specimens measuring 200x30x12 mm were cutted (Figure 4.12, right). The first type of specimen will be identified as "small" and the second one as "big".

Figure 4.12. Small geometry samples (160x20x10 mm) (left); big geometry samples (200x30x12 mm) (right).

The following table (**Table 4.1**) shows the names and characteristics of each plate and the related sample geometries tested with IET.

Table 4.1. Characteristics of tested samples, obtained from different plates

Plates	**5**	**6**	**7**	**10**	**12**	**18.1**	**18.2**	**18.3**	**18.4**
Length (mm)	160	160	160	160	160	200	200	200	200
Width (mm)	20	20	20	20	20	30	30	30	30
Thickness (mm)	10	10	10	10	10	12	12	12	12
Mass (g)	70	70	70	70	70	160	160	160	160
N° of samples	9	9	9	9	9	6	6	6	6

Firstly, IET tests were conducted at room temperature to gain an understanding of the material's Young's modulus value. For a comprehensive analysis, both RT and HT setups were used, both at room temperature; slightly different values were obtained with the HT setup, as a result of the fact that it is more insulated from the environmental conditions compared to RT setup. Only plates 10 and 12 were tested using both set-ups, then it was chosen to use only the HT set-up for the other plates. Another important point is that for plates 10 and 12 the results include data from previous tests conducted by another operator under the same operating conditions.

In the image below (**Figure 4.13**), the typical acquisition screen of the RFDA software is shown. The left screen measures damping, while the right screen displays the vibration frequency spectrum with various peaks corresponding to different vibration modes of the sample. The first frequency, with the highest peak, corresponds to the fundamental vibration modes of the material under bending stresses. Typical frequencies for the material under analysis are around 1500 Hz at room temperature conditions. Once the frequency is detected, the software automatically uses it to calculate Young's modulus. Between 7 and 10 excitations were applied to each sample, each corresponding to a specific stiffness value. From these results, the average modulus value at room temperature was obtained for each specimen in both setups, enabling estimation of the overall plate stiffness at room temperature.

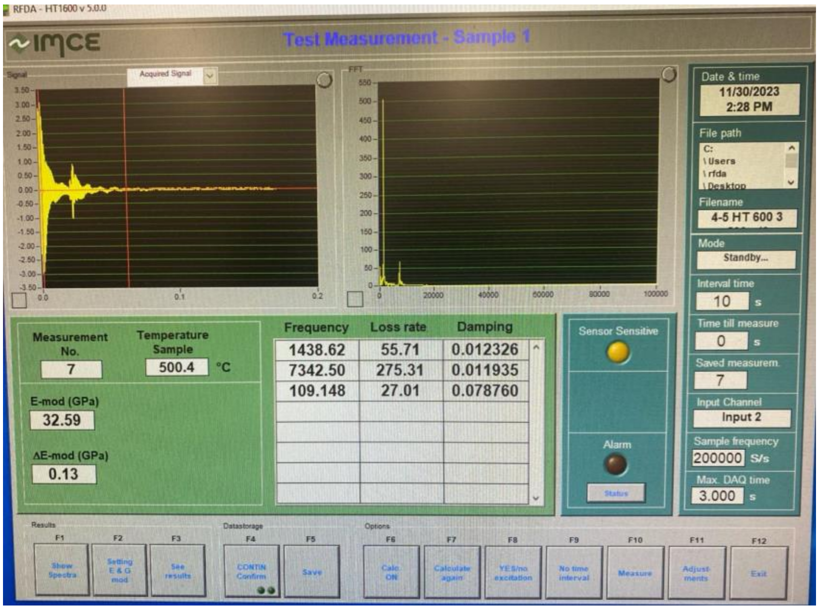

Date & time: 11/30/2023 2:28 PM

File path: C: \Users \rfda \Desktop

Filename: 4-5 HT 600 3

Mode: Standby...

Interval time: 10 s

Time till measure: 0 s

Saved measurem.: 7

Input Channel: Input 2

Sample frequency: 200000 S/s

Max. DAQ time: 3.000 s

Measurement No.: 7

Temperature Sample: 500.4 °C

E-mod (GPa): 32.59

ΔE-mod (GPa): 0.13

Frequency	Loss rate	Damping
1438.62	55.71	0.012326
7342.50	275.31	0.011935
109.148	27.01	0.078760

Figure 4.13. Data acquisition screen of the RFDA software.

In the following tables (**Table 4.2** and **Table 4.3**) are collected the results related to the RT tests conducted with both setups for the 10 and 12 plates. It is worth noting that they also include values from tests conducted previously by another operator.

Table 4.2. Test results of IET RT tests using RT and HT setups for samples of plate 10.

PLATE 10 SAMPLES	1	2	3	4	5	MEASURE UNIT
set up HT	45.0	34.4	36.0	37.6	38.6	GPa
standard deviation HT	1.2	3.3	1.0	1.0	0.9	GPa
set up RT	45.0	38.0	37.3	39.0	39.1	GPa
standard deviation RT	0.7	1.8	0.6	0.8	0.7	GPa

AVERAGE YOUNG MODULUS FOR PLATE 10	**39.0**					**GPa**
TOTAL STANDARD DEVIATION	**3.5**					**GPa**

Table 4.3. Test results of IET RT tests using RT and HT setups for samples of plate 12.

PLATE 12 SAMPLES	**1**	**2**	**3**	**4**	**5**	**6**	**MEASURE UNIT**
set up HT	34.3	33.1	41.0	36.6	36.6	34.7	GPa
standard deviation HT	1.1	0.8	0.7	1.5	0.7	1.0	GPa
set up RT	35.8	33.9	41.8	35.6	38.1	34.7	GPa
standard deviation RT	1.2	0.7	0.7	3.0	1.7	1.0	GPa
AVERAGE YOUNG MODULUS FOR PLATE 12	**36.3**						**GPa**
TOTAL STANDARD DEVIATION	**2.7**						**GPa**

Samples from 6 to 9 of plate 10 were not considered as they underwent some heat treatment at high temperature prior to the test, which drastically compromised their mechanical properties. Meanwhile, the values for the remaining plates are displayed in the tables below (**Tables 4.4 - 4.10**):

Table 4.4. Test results of IET RT tests using HT setup for samples of plate 5.

SAMPLES PLATE 5	**1**	**2**	**3**	**4**	**5**	**6**	**7**	**8**	**9**
Average Young Modulus (Gpa)	41.7	43.2	40.3	38.9	38.0	39.6	42.0	38.8	38.9
Standard Deviation	0.13	0.46	0.03	0.13	0.19	0.13	0.18	0.27	0.16

AVERAGE YOUNG MODULUS FOR PLATE 5 (GPa)	**40.2**
TOTAL STANDARD DEVIATION (GPa)	0.19

Table 4.5. Test results of IET RT tests using HT setup for samples of plate 6.

SAMPLES PLATE 6	**1**	**2**	**3**	**4**	**5**	**6**	**7**	**8**	**9**
Average Young Modulus (Gpa)	38.0	42.4	40.5	40.7	39.0	37.8	40.1	42.3	38.7
Standard Deviation	0.41	0.15	0.03	0.06	0.09	0.23	0.04	0.10	0.17

AVERAGE YOUNG MODULUS FOR PLATE 6 (GPa)	**39.9**
TOTAL STANDARD DEVIATION (GPa)	**0.14**

Table 4.6. Test results of IET RT tests using HT setup for samples of plate 7.

SAMPLES PLATE 7	**1**	**2**	**3**	**4**	**5**	**6**	**7**	**8**	**9**
Average Young Modulus (Gpa)	39.9	38.2	39.0	39.3	39.7	40.4	41.5	43.1	40.3
Standard Deviation	0.36	0.37	0.10	0.22	0.22	0.10	0.08	0.14	0.21

AVERAGE YOUNG MODULUS FOR PLATE 7 (GPa)	**40.2**
TOTAL STANDARD DEVIATION (GPa)	**0.20**

Table 4.7. Test results of IET RT tests using HT setup for samples of plate 18.1.

SAMPLES PLATE 18.1	**1**	**2**	**3**	**4**	**5**	**6**
Average Young Modulus (Gpa)	39.0	42.0	42.9	42.1	40.7	40.6
Standard Deviation	0.02	0.17	0.09	0.12	0.07	0.11
AVERAGE YOUNG MODULUS FOR PLATE 18.1 (GPa)				**41.2**		
TOTAL STANDARD DEVIATION (GPa)				**0.10**		

Table 4.8. Test results of IET RT tests using HT setup for samples of plate 18.2.

SAMPLES PLATE 18.2	**1**	**2**	**3**	**4**	**5**	**6**
Average Young Modulus (Gpa)	40.4	39.0	40.3	40.5	39.6	43.0
Standard Deviation	0.11	0.03	0.06	0.14	0.09	0.20
AVERAGE YOUNG MODULUS FOR PLATE 18.2 (GPa)			**40.5**			
TOTAL STANDARD DEVIATION (GPa)			**0.11**			

Table 4.9. Test results of IET RT tests using HT setup for samples of plate 18.3.

SAMPLES PLATE 18.3	**1**	**2**	**3**	**4**	**5**	**6**
Average Young Modulus (GPa)	43.2	41.9	43.7	45.5	42.8	45.1
Standard Deviation	0.07	0.21	0.10	0.25	0.24	0.27
AVERAGE YOUNG MODULUS FOR PLATE 18.3 (GPa)			**43.7**			
TOTAL STANDARD DEVIATION (GPa)			**0.19**			

Table 4.10. Test results of IET RT tests using HT setup for samples of plate 18.4.

SAMPLES PLATE 18.4	**1**	**2**	**3**	**4**	**5**	**6**
Average Young Modulus (Gpa)	39.9	39.9	41.8	40.0	37.2	39.1
Standard Deviation	0.15	0.32	0.28	0.36	0.15	0.25
AVERAGE YOUNG MODULUS FOR PLATE 18.4 (GPa)	**39.6**					
TOTAL STANDARD DEVIATION (GPa)	**0.25**					

As can be seen, the values of the elastic modulus are consistent with typical values for materials of this type at ambient temperature conditions.

4.4.2 HIGH TEMPERATURE TESTS (HT)

Once the stiffness at room temperature was determined, the RFDA HT1600 furnace was utilized to analyze the variation of material stiffness as a function of temperature. Various types of temperature tests (HT) were conducted for this purpose. All tests carried out are resumed below in **Table 4.11**. For each sample, it is possible to observe which test was done and how many times.

Table 4.11. IET HT test plan for all the plates

PLATES	SAMPLE	IET HT 250°C	IET HT 400°C	IET HT 600°C
10	5	\	\	\
	6	\	\	\
	7	4X	\	2X
	8	4X	\	2X
	9	4X	\	2X
12	7	4X	\	X
	8	4X	\	X
	9	4X	\	X
5	1	2X	\	\
	2	2X	\	\
	3	2X	\	\
	4	\	\	3X
	7	\	\	\
6	1	2X	\	\
	2	2X	\	\
	4	\	3X	\
7	1	2X	\	\
	2	2X	\	\
18.1	1	2X	\	\
	2	2X	\	\
18.2	1	2X	\	\
	2	2X	\	\
18.3	1	2X	\	\
	2	2X	\	\
	4	\	3X	\
18.4	1	2X	\	\
	2	2X	\	\
	4	\	3X	\

The tests up to 250 °C will be discussed. Data from Plates 10 and 12 are different compared to the others because high-temperature tests were also conducted before by another operator, and therefore, the final results are a combination of both measurement experiences.

Some samples from every plate underwent a heating cycle from room temperature up to 250 °C at least twice. From these tests, it is possible to analyze the trend of Young's modulus with increasing temperature. Repeating the same thermal cycle on the same sample demonstrates how it is irreversibly modified at the end of each cycle, providing valuable insights into how the material's stiffness changes after exposure to high temperatures.

The thermal cycle used for these tests involved a temperature increase at a rate of 10°C/min until reaching target temperatures of 100 °C, 150 °C, 200 °C, and 250 °C (**Figure 4.14**). A dwell of 10 minutes was set upon reaching each temperature, allowing the system to stabilize at the target temperature. Then, between 7 and 10 excitations were applied, to measure various Young's modulus values used to estimate the average modulus for each sample at each specific temperature. Furthermore, for these tests, a 40% impact power was used to avoid altering the sample's position, with a 10-second interval between consecutive impacts.

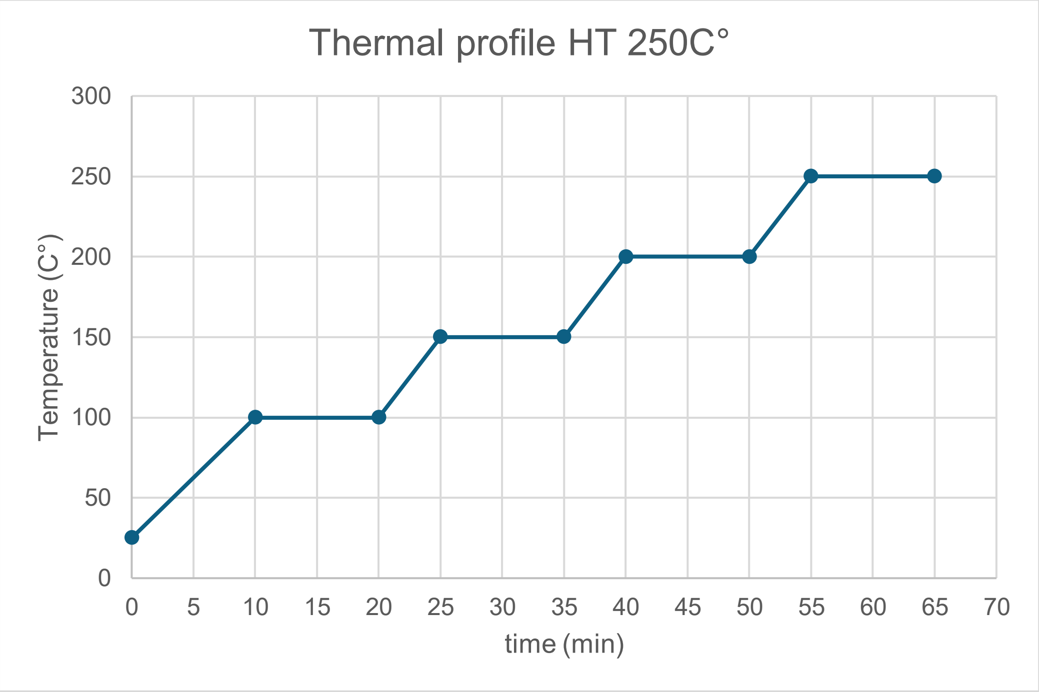

Figure 4.14 Thermal profile used for IET test till 250 °C.

Below are shown the graphs related to the samples from plates 10 (**Figure 4.15**) and 12 (**Figure 4.16**).

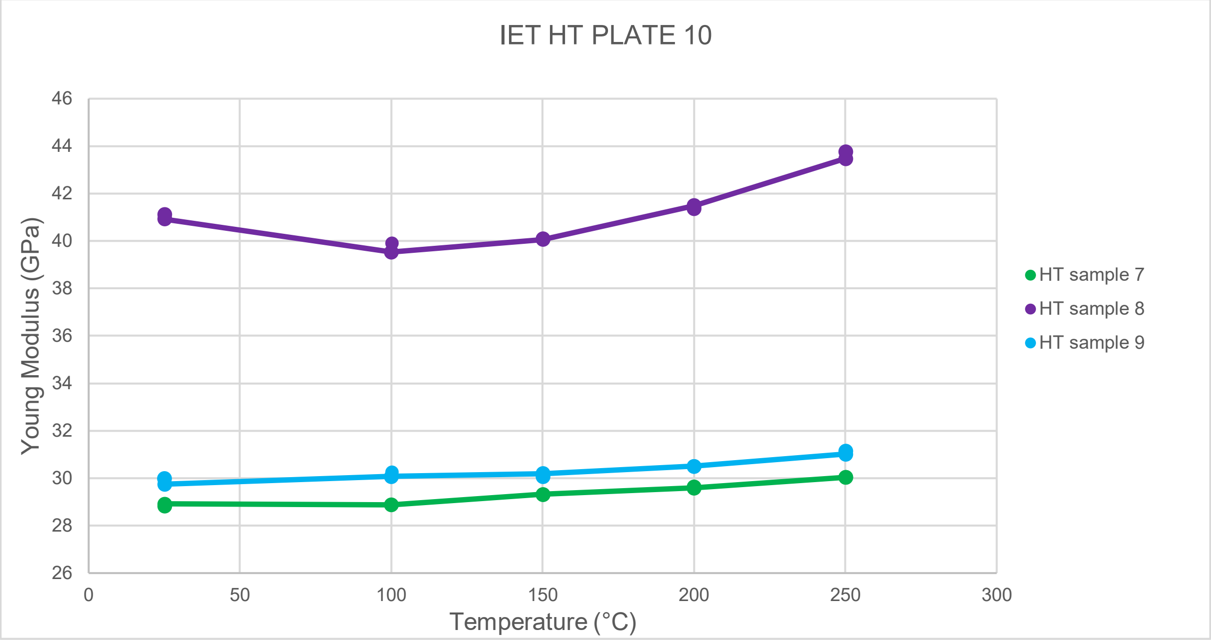

Figure 4.15. Variation of E (GPa) in HT 250 IET test for samples of plate 10.

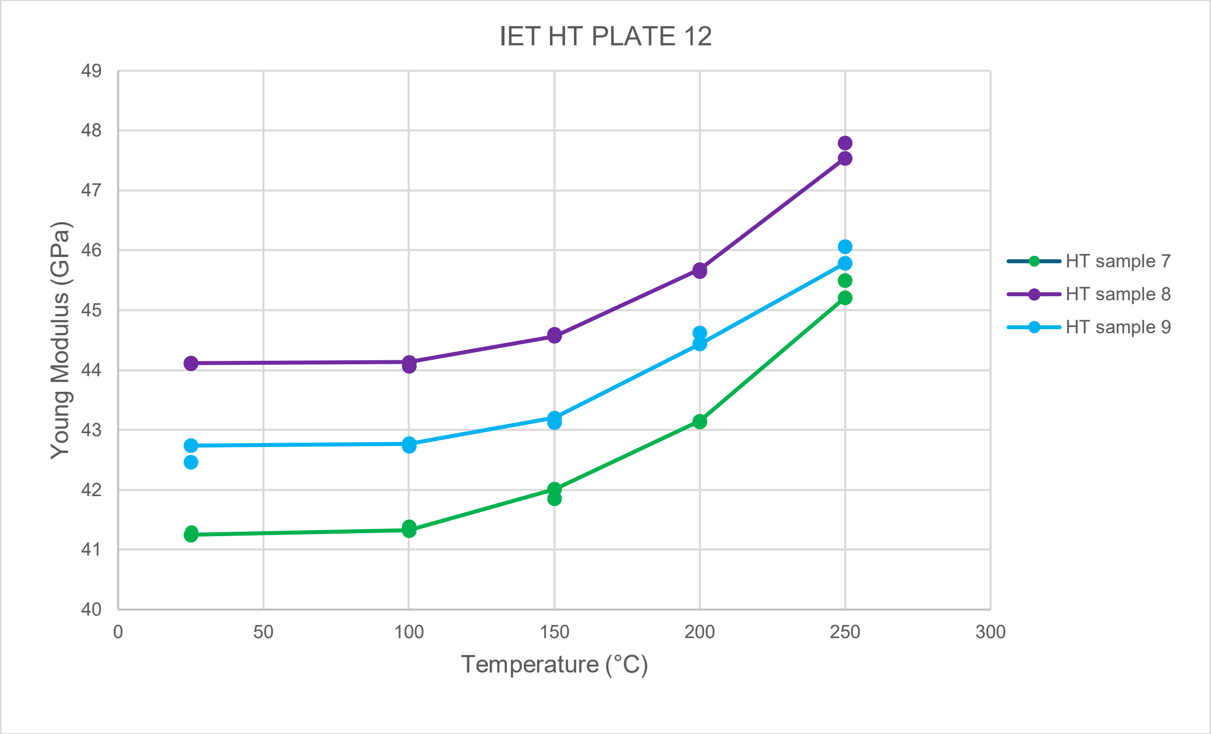

Figure 4.16. Variation of E (GPa) in HT 250 IET test for samples of plate 12.

From the graphs shown, several information can be derived. Firstly, it's crucial to specify that samples 7 and 9 from plate 10 underwent thermal cycling up to 250 °C by another operator before the test, as well as a cycle up to 600 °C, irreversibly compromising their modulus. Indeed, the behavior of these two samples is different from that of the other samples. From the curves, it is evident that for specimens not previously tested up to 600 °C, the modulus tends to increase with temperature.

Next, the graphs below show all tests up to 250 °C undergone by samples from plates 10 and 12 (**Figure 4.17 - 4.22**); gray lines represent curves from data previously collected by another operator who performed three thermal cycles up to 250 °C on the same sample, while the red line represents the curve related to measurements from this study, totaling four HT 250 IET tests for each sample. In the legend nomenclature, "HT sample 7.1" indicates Young's modulus data for the first repetition of the thermal cycle on sample 7.

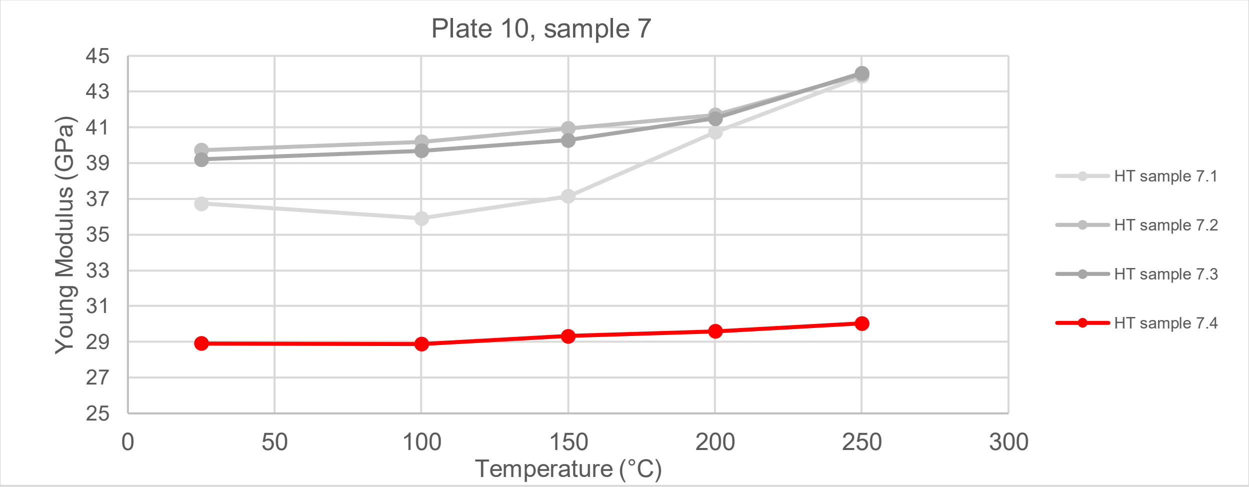

Figure 4.17. Variation of E (GPa) in repeated HT 250 tests for sample 7 of plate 10.

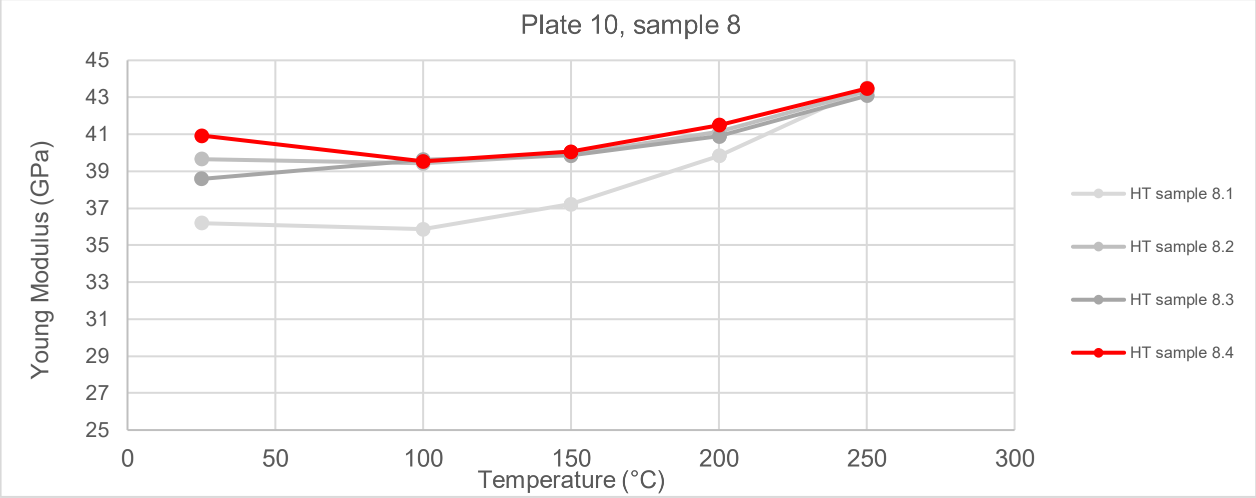

Figure 4.18. Variation of E (GPa) in repeated HT 250 tests for sample 8 of plate 10.

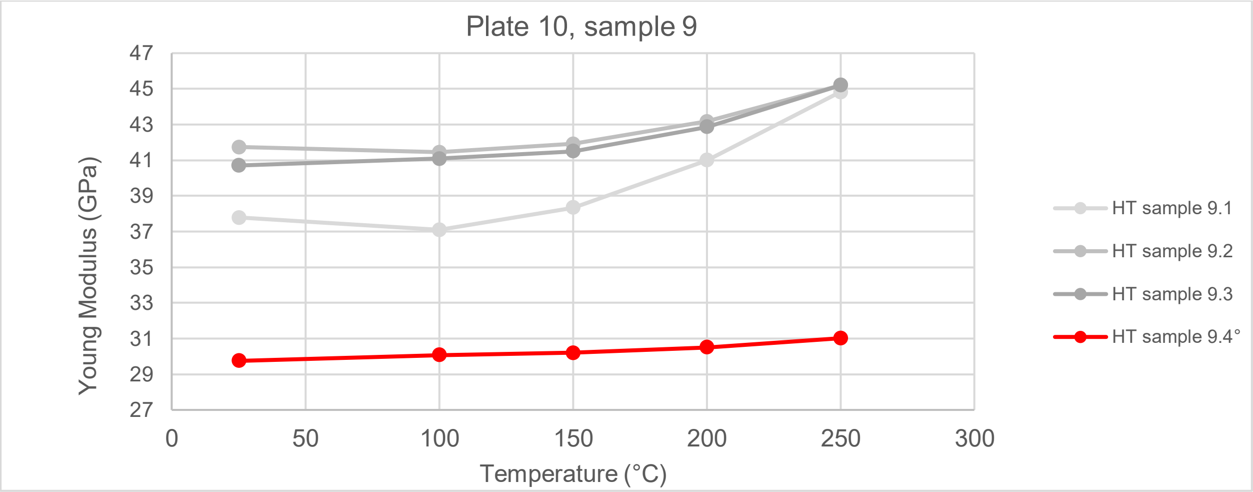

Figure 4.19. Variation of E (GPa) in repeated HT 250 tests for sample 9 of plate 10.

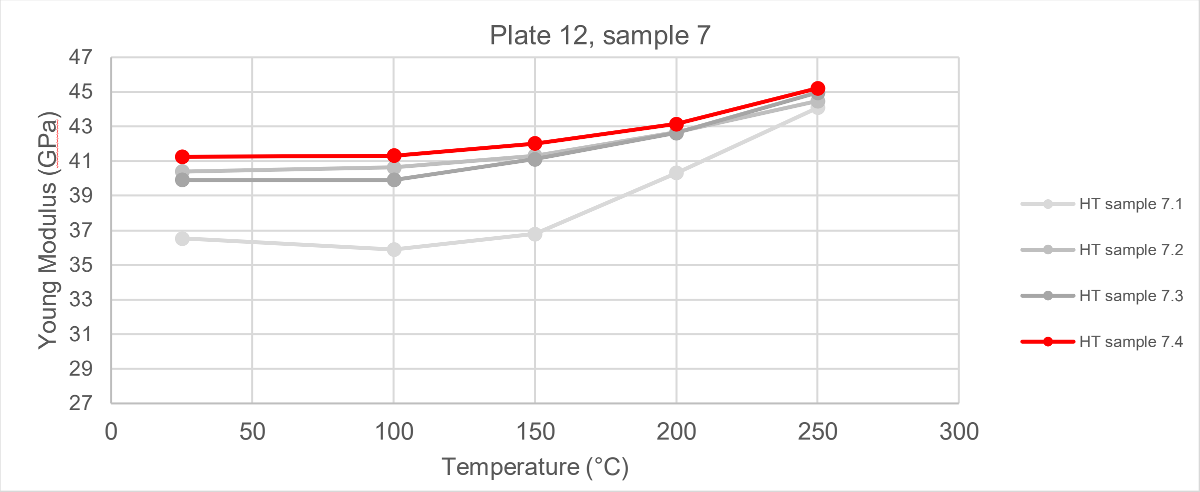

Figure 4.20. Variation of E (GPa) in repeated HT 250 tests for sample 7 of plate 12.

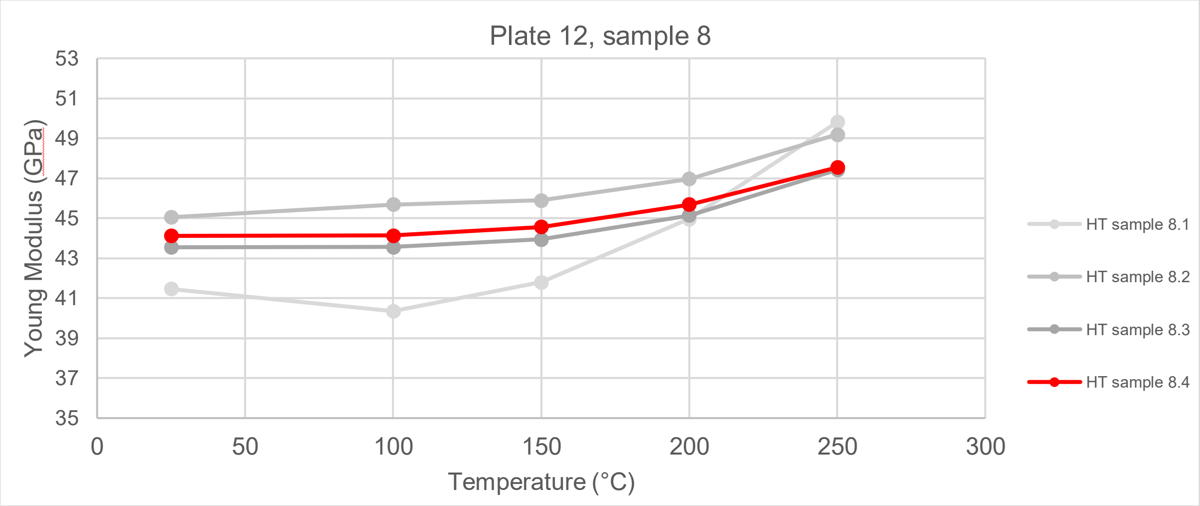

Figure 4.21. Variation of E (GPa) in repeated HT 250 tests for sample 8 of plate 12.

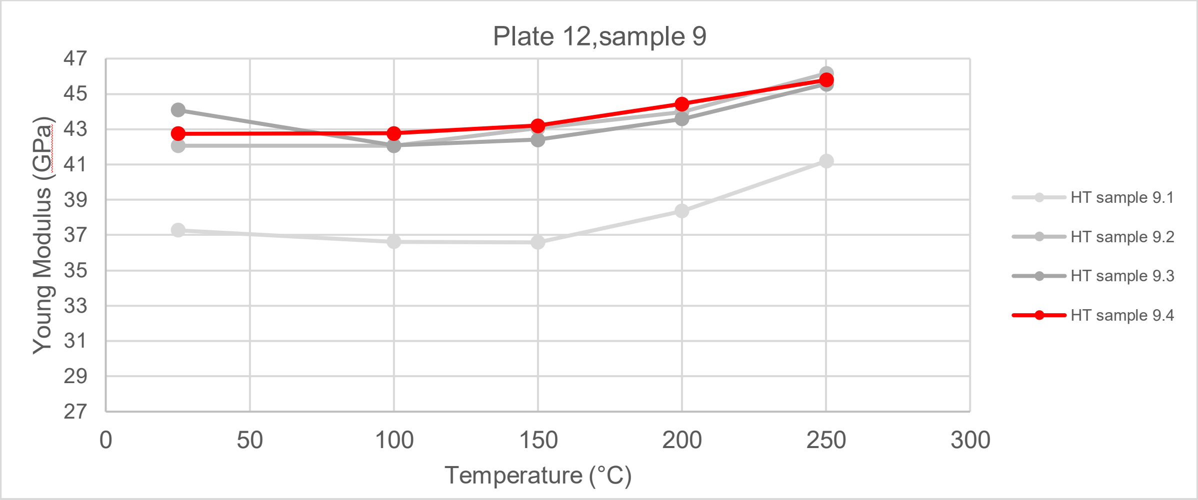

Figure 4.22. Variation of E (GPa) in repeated HT 250 tests for sample 9 of plate 12.

From the data, it is evident that the repetition of the cycle from RT to 250 °C tends to increase the starting modulus at RT, with the material stiffening after each cycle. Furthermore, the modulus also increases during the cycle itself, and the maximum modulus reached in the various cycles consistently ranges around the same value, typically between 45 and 50 GPa. This analysis excludes samples 7 and 9 from plate 10, which were irreversibly damaged by previous treatments up to 600 °C.

Continuing with the data report, the curves for the HT 250 tests of samples taken from the other plates (5, 6, 7, 18.1, 18.2, 18.3, 18.4) are presented (**Figure 4.23 - 4.26**). To avoid overloading the document, only curves for some plates are shown.

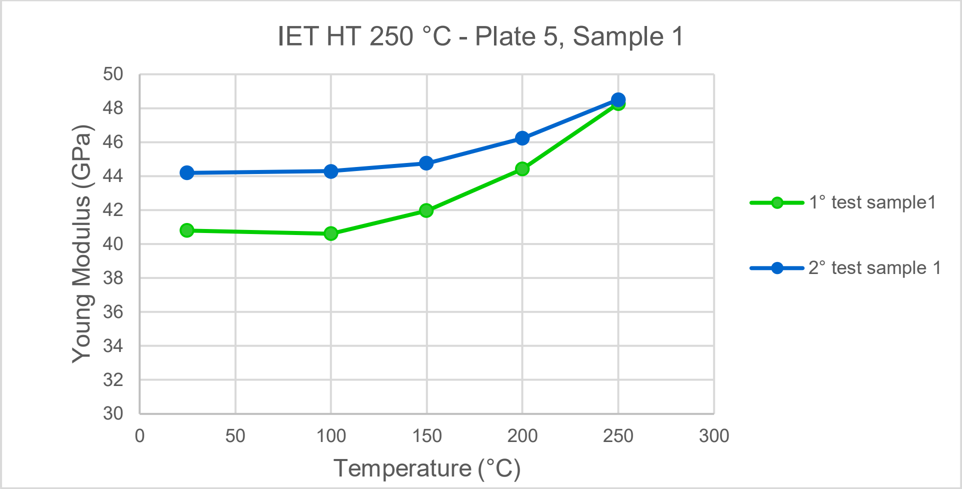

Figure 4.23. Variation of E (GPa) in repeated HT 250 tests for sample 1 of plate 5.

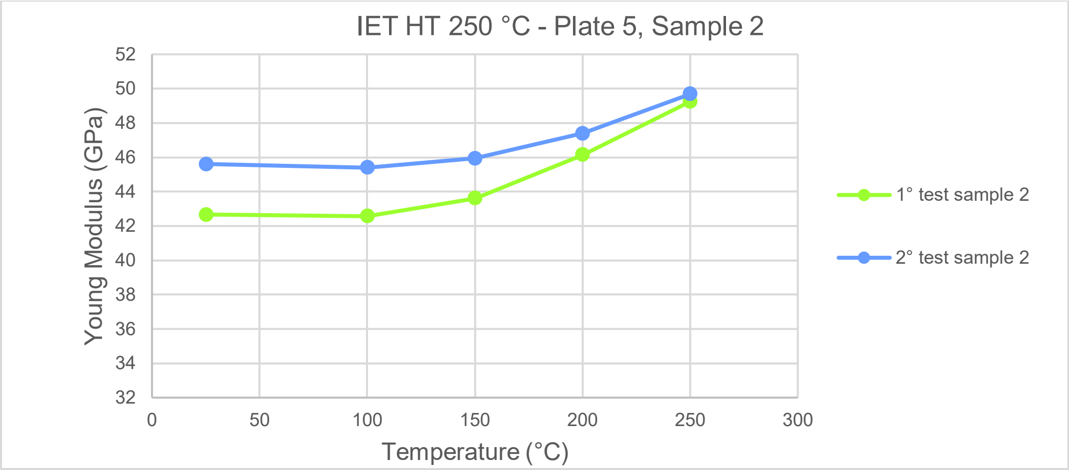

Figure 4.24. Variation of E (GPa) in repeated HT 250 tests for sample 2 of plate 5.

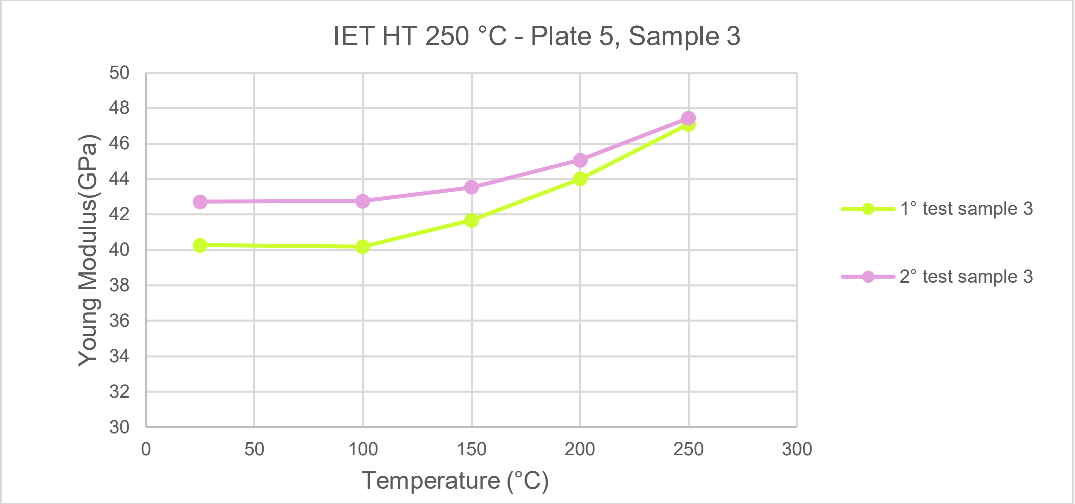

Figure 4.25. Variation of E (GPa) in repeated HT 250 tests for sample 3 of plate 5.

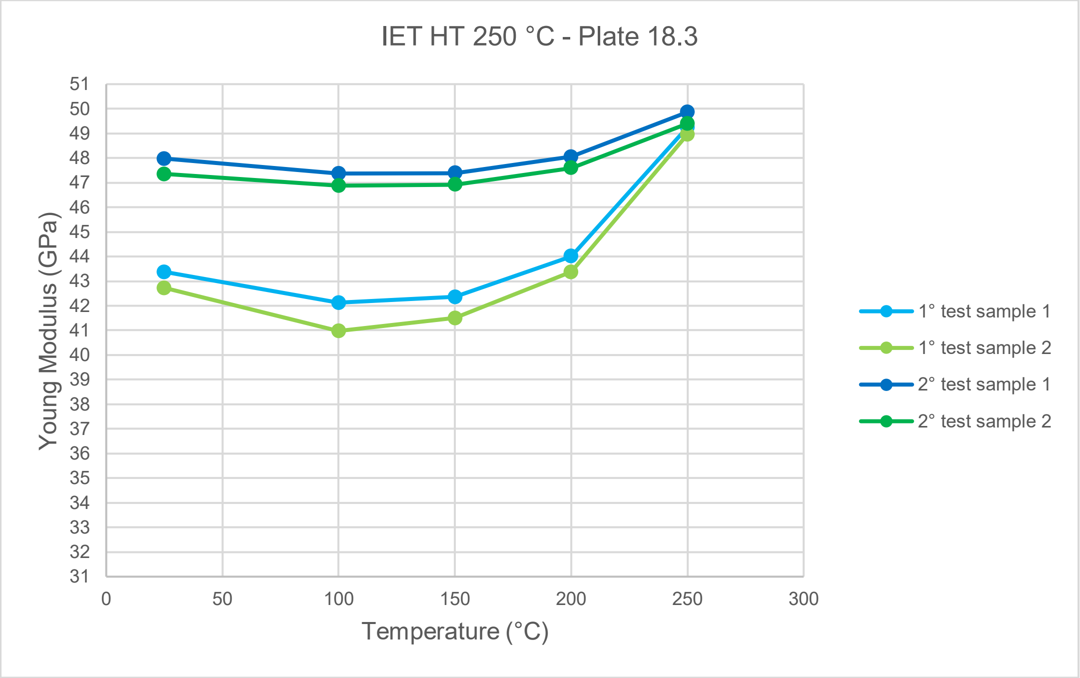

Figure 4.26. Variation of E (GPa) in repeated HT 250 tests for samples 1 and 2 of plate 18.3.

The trend of the curves for the other plates (**Figure 4.23 - 4.26**) confirms the increase of the modulus with temperature, which is much more evident at the end of the thermal cycle (between 200 and 250°C).

At this point, the data related to the IET tests up to 600 °C will be presented. The characteristics of the thermal profile used for these tests are the same as the test HT 250; only the final target temperature changes, which is 600 °C. As can be seen from Table 4.11, samples 7 and 9 from plate 10 were tested twice, but in this case, the first repetition of the test was conducted by another operator. In other cases, the measurement was performed by a single operator.

Below are the curves related to the HT 600 tests (**Figure 4.27 - 4.30**).

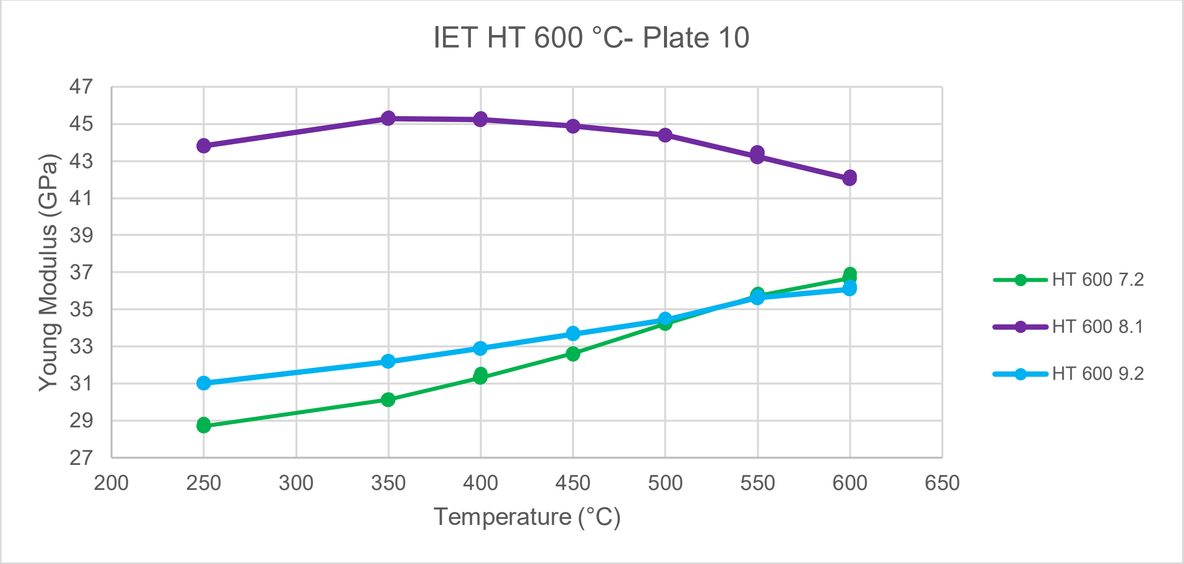

Figure 4.27. Variation of E (GPa) from HT 600 tests for samples 7,8,9 of plate 10.

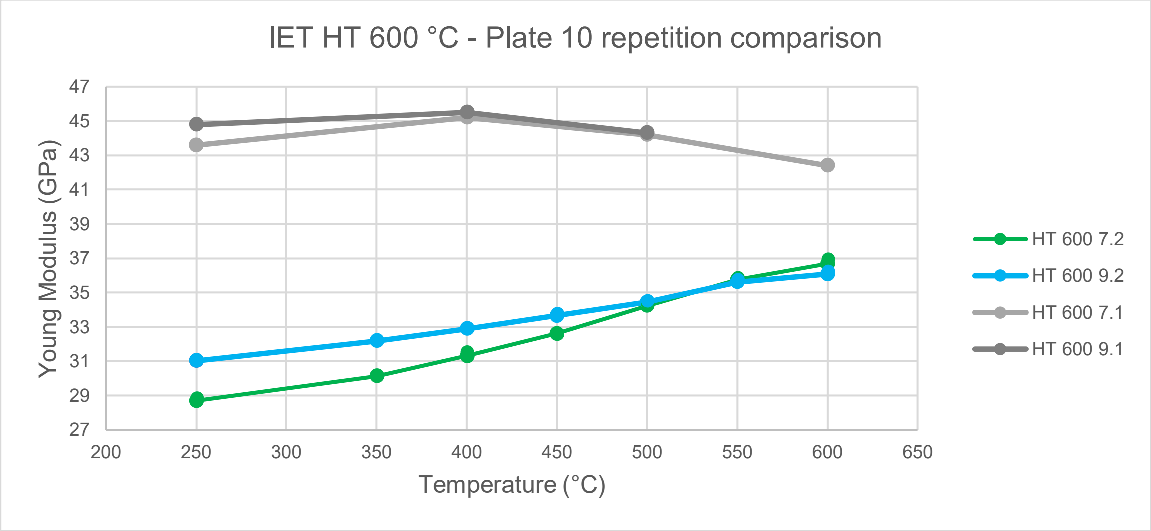

Figure 4.28. Comparison of variation of E (GPa) from repeated HT 600 tests for samples 7,9 of plate 10.

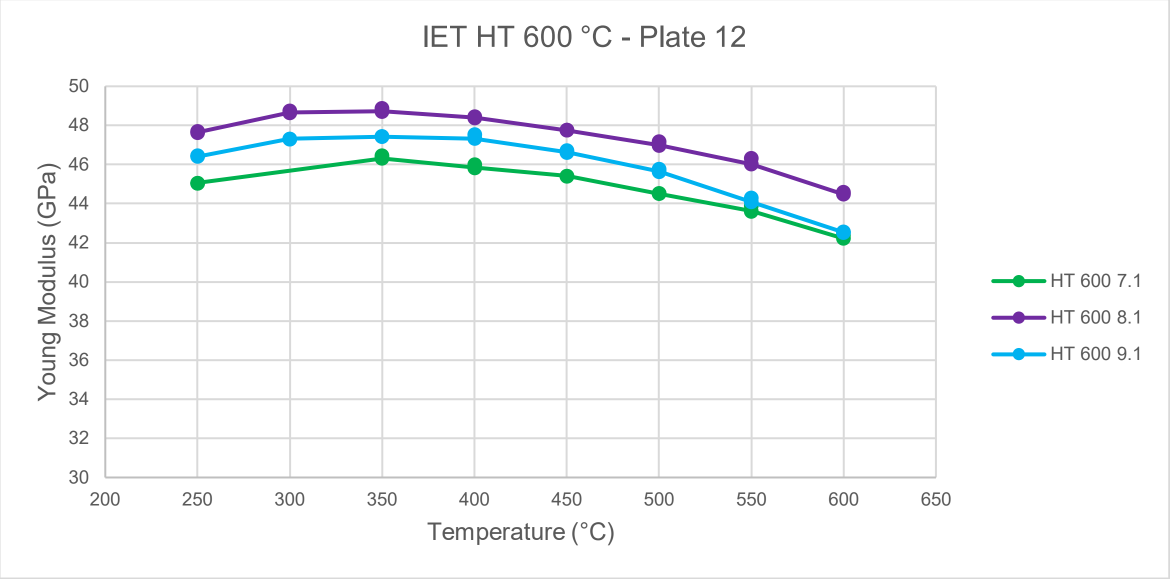

Figure 4.29. Variation of E (GPa) from HT 600 tests for samples 7,8,9 of plate 12.

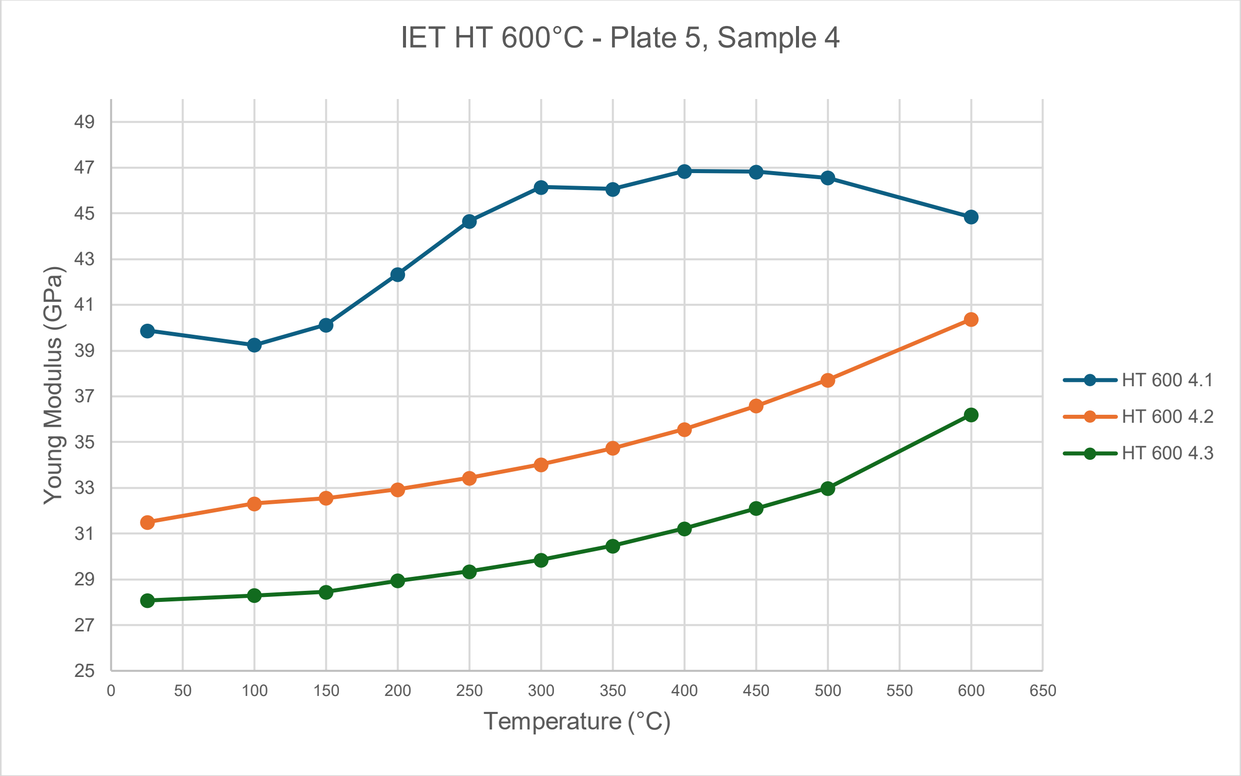

Figure 4.30. Variation of E (GPa) from HT 600 tests for sample 4 of plate 5 with 3 repetitions of the cycle.

From the reported elastic modulus data, it is observed that the trend characterizing the first cycle up to 600 °C shows an increasing trend until around 350/400 °C, where a peak modulus is reached, followed by a significant decrease towards 600 °C, that is caused by the degradation of the fibers imposed by an oxidation process. However, for samples 7 and 9 from plate 10, as well as sample 4 from plate 5, subsequent thermal cycle repetitions are heavily influenced by the first cycle, which drastically and irreversibly reduces the Young's modulus of the material at room temperature. As depicted in Figure 4.30, the modulus tends to decrease with the number of thermal cycle repetitions. Furthermore, another interesting observation can be made by analyzing the trend of the curves related to cycle repetitions; notably, the modulus tends to increase steadily with temperature rather than decreasing after 350/400 °C as observed in the initial test.

Another important information is the sample mass change after HT 600 tests. The data of mass are shown in **Table 4.12**.

Table 4.12. Mass variation of HT 600 tested samples

PLATE	SAMPLES	MASS (g)	MASS AFTER HT 600 (g)	MASS LOSS (%)
10	7	70.50	68.71	2.5%
	8	71.67	71.02	0.9%
	9	74.39	73.03	1.8%
12	7	71.40	70.85	0.8%
	8	71.52	71.01	0.7%
	9	71.11	70.6	0.7%

.

It is important to indicate that samples 7 and 9 of plate 10 have higher mass loss due to the fact they were tested twice while the other sample once.

Continuing with the results report, the results of IET tests up to 400 °C will now be presented. Once again, the thermal profile used for these tests follows the same pattern as the previously shown tests. The 400 °C tests were introduced to gain further insights into the material's behavior around the peak modulus observed in the 600 °C tests.

Examining **Figure 4.31**, **Figure 4.32**, and **Figure 4.33**, a trend is observed that confirms both the 250 °C and 600 °C tests; the maximum modulus is reached between 300 and 400 °C, followed by a small decrease, confirming the material's behavior when subjected to a high-temperature thermal cycle for the first time.

Regarding the material's behavior in response to subsequent cycles, there is a slight decrease in the initial modulus (at room temperature) compared to what the material would have if it had not been subjected to high temperatures, along with the same increase in E seen for repeated tests at 600 °C.

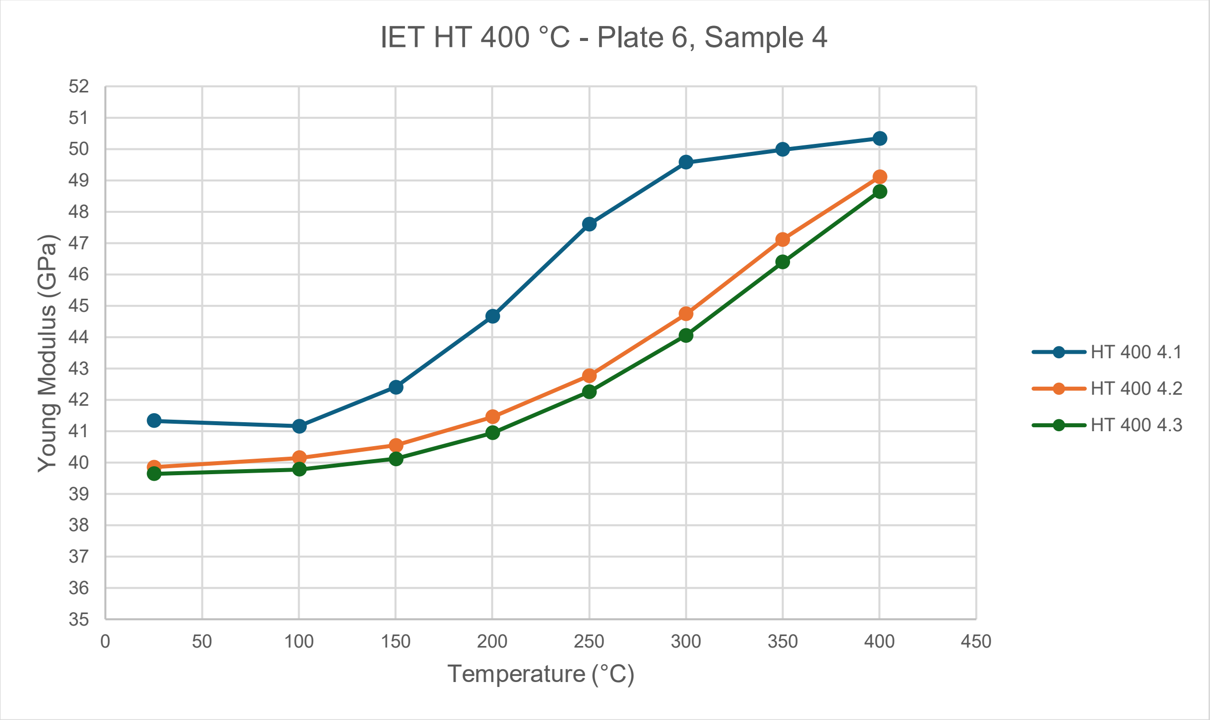

Figure 4.31. Variation of E (GPa) from HT 400 tests for sample 4 of plate 6.

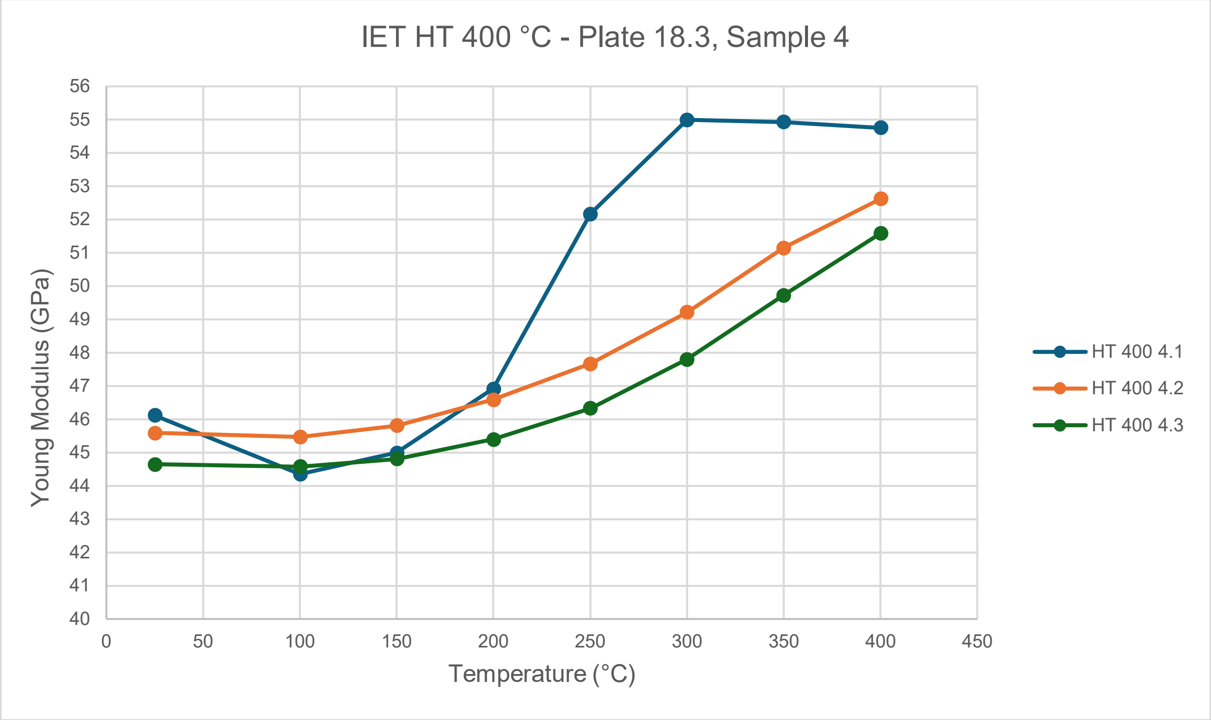

Figure 4.32. Variation of E (GPa) from HT 400 tests for sample 4 of plate 18.3.

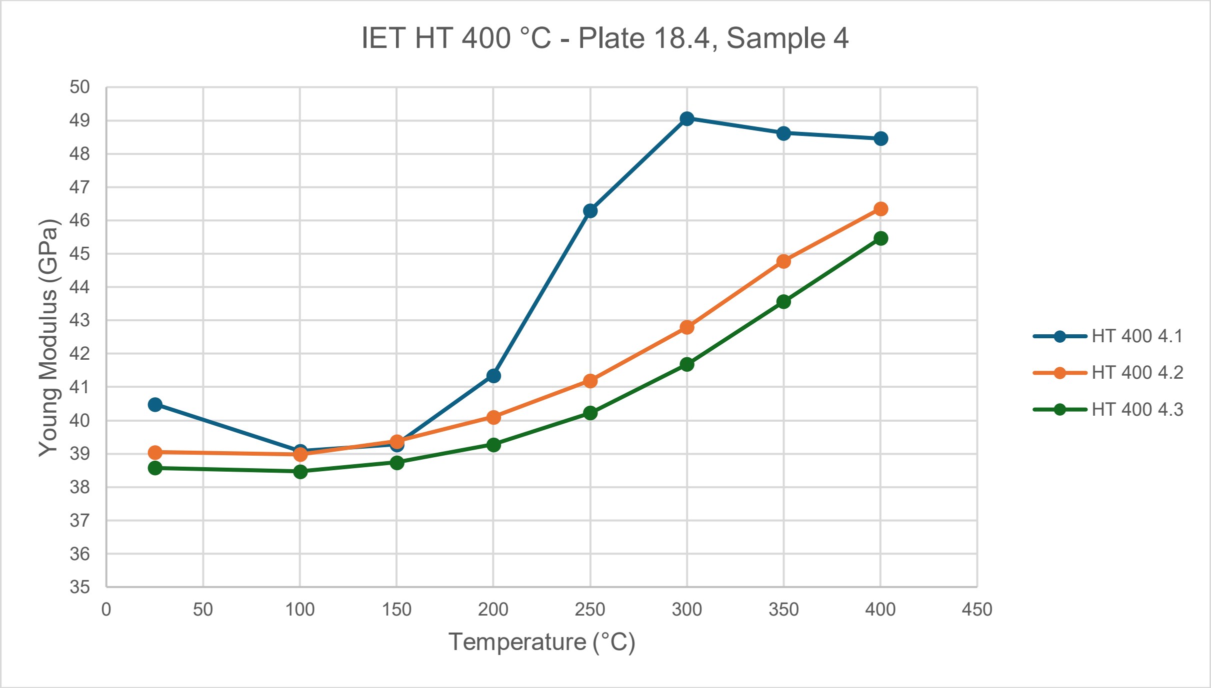

Figure 4.33. Variation of E (GPa) from HT 400 tests for sample 4 of plate 18.4.

Also for this type of tests were collected the changes of sample mass after the 3 repetitions of the cycle, as it is possible to see in the **Table 4.13**.

Table 4.13. Mass variation of HT 400 tested samples

PLATE	SAMPLE	MASS (g)	MASS AFTER 3° TEST (g)	MASS LOSS (%)
6	4	70.84	70.73	0.16
18.3	4	163.96	163.64	0.20
18.4	4	159.16	158.85	0.19

.

4.5 *BUILDING UP OF IET SET UP IN THE BSCCB LABORATORY*

During the experience gained at the BSCCB laboratory, there was a desire to replicate the measurement principle of IET tests but with different instruments and work environments. The goal was to recreate the IET RT tests at the BSCCB laboratory, both to compare them with those obtained with the RFDA HT1600 machine at the J-Tech laboratory of the Polytechnic University of Turin and to create a new non-destructive method for measuring the Young's modulus, which is important to avoid unnecessary material waste.

The process began by attempting to adapt the workstation used for modal analysis or FRF on entire brake discs to a setup for analyzing samples of the aforementioned dimensions. Two nylon wires were then tied to the existing supports, which were connected to weights that, once suspended, provided sufficient tension in the wires. Additionally, graduated scales were glued to the side supports to allow precise adjustment of the distance between the wires, corresponding to the distance between the nodes where the material is supported. Essentially, the RT setup described earlier and illustrated in Figure 4.5 was recreated. The final result is depicted below in **Figure 4.34**.

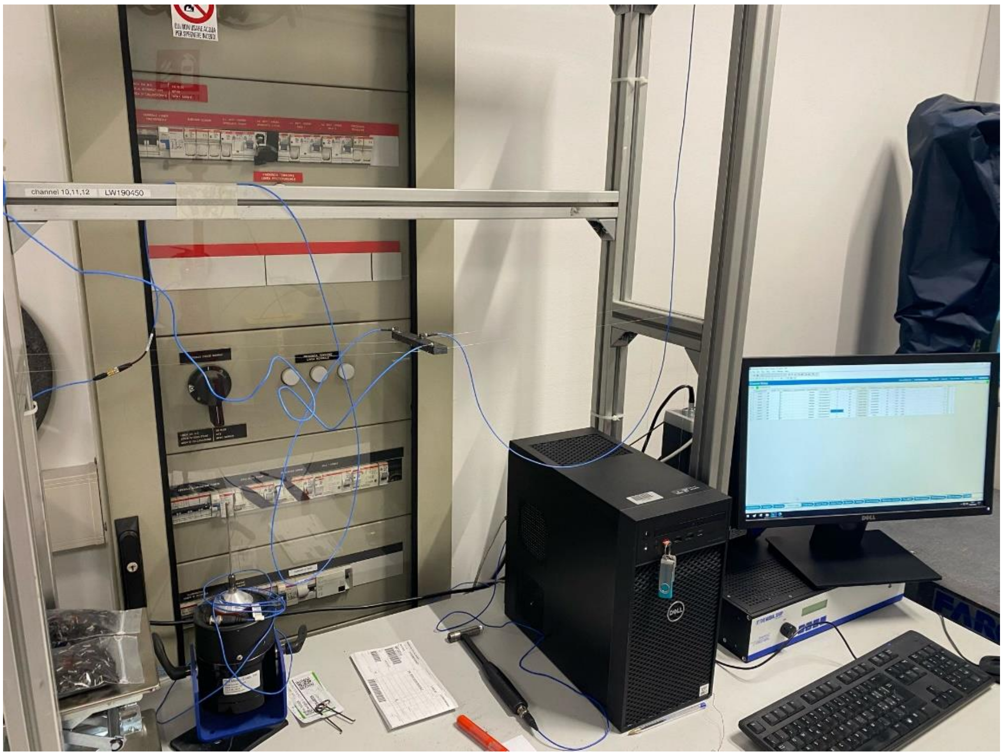

Figure 4.34. IET RT set up in BSCCB laboratory.

The main difference between the two setups lies in the system used for acquiring vibration frequencies. In the RT setup used at the J-Tech@PoliTO (Politecnico di Torino) laboratories, vibrations were captured by a microphone, whereas in the setup used at the BSCCB laboratories, they were detected by accelerometers directly in contact with the sample itself. These accelerometers can be seen in Figure 4.35 as blue wires attached to the sample with resin. From field experiments, it was observed that the position of the accelerometers does not significantly affect the acquisition of vibration frequencies, especially for small-sized samples like those used in this study. Thanks to the oscillations of the accelerometer positions following the impact on the specimen, the software captured the vibration frequencies of the sample. The procedure used for sample placement is the same as that used with the RT setup at J-Tech@PoliTO [18]; thus, the guidelines of ASTM E 1876 were followed, as explained earlier in chapter 4.1.2.

Figure 4.35. Accelerometers (blu wires) used in IET RT set up in BSCCB laboratory.

Another difference between the two setups is the excitation system. While in the previous case, an automatic system was used, in this setup, a manual method was employed using a specialized hammer, as shown in **Figure 4.36**. Adhering to ASTM E 1876 standards, the impact was applied at the center of the sample, which is as far away from the nodes as possible.

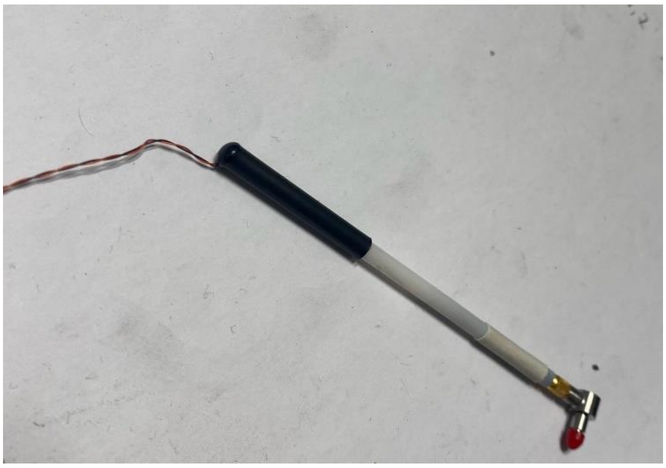

Figure 4.36. Hammer used in IET RT set up in BSCCB laboratory.

The input parameters for the software used in this case primarily included the geometry and the positions of the accelerometers. Once these were set, along with the frequency acquisition limits (set at 12000 Hz) and resolution (0,3 Hz), five impacts were applied using the hammer. The software then averages the frequency spectra from each excitation, creating a single spectrum. An example of this spectrum is provided in **Figure 4.37.**

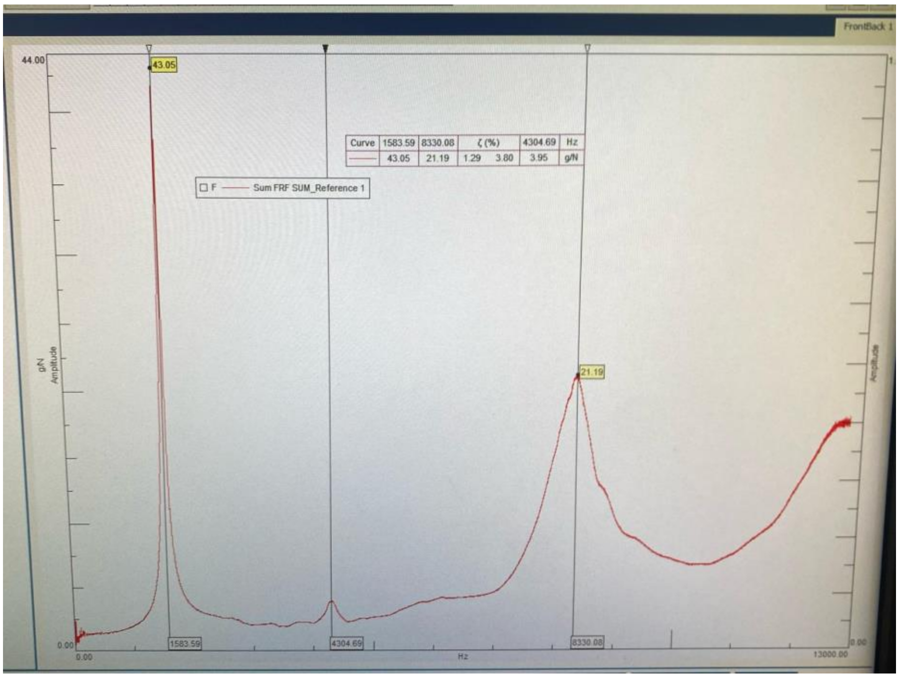

Curve	1583.59	8330.08	ζ (%)		4304.69	Hz
—	43.05	21.19	1.29	3.80	3.95	g/N

Figure 4.37. Example of frequency spectrum resulting from an IET test with BSCCB set up.

Once this spectrum is obtained, the frequency corresponding to the first peak, representing the fundamental vibration modes of the material, is extracted. This frequency value is then used in the relationship provided by the ASTM E 1876 standard, as depicted in **Figure 4.4**. Of course, the geometric parameters of each sample are also measured and inserted into the formula. This process allowed for the calculation of Young's moduli for several samples, both from plates previously tested using the RT setup at J-Tech@PoliTO and from plates not yet tested. This enabled a comparison between the two experimental methods.

4.5.1 RESULTS

In the following figures (**Figure 4.38**, **Figure 4.39**, **Figure 4.40**) are shown the calculated Young’s moduli of samples of different plates.

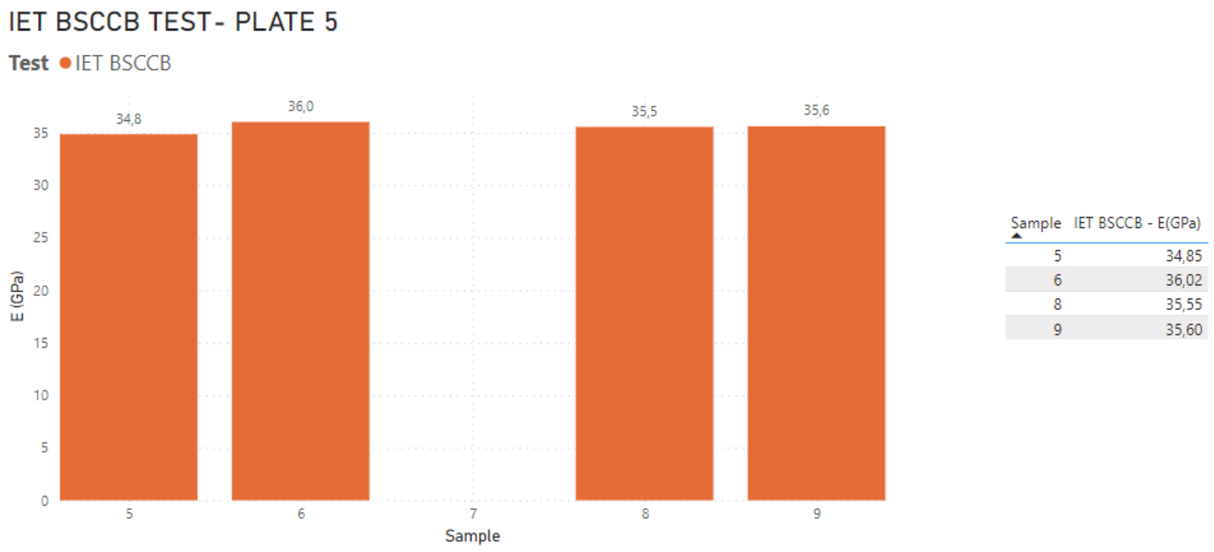

Sample	IET BSCCB - E(GPa)
5	34,85
6	36,02
8	35,55
9	35,60

Figure 4.38. Calculated Young’s moduli of samples of plate 5 from an IET test with BSCCB set up.

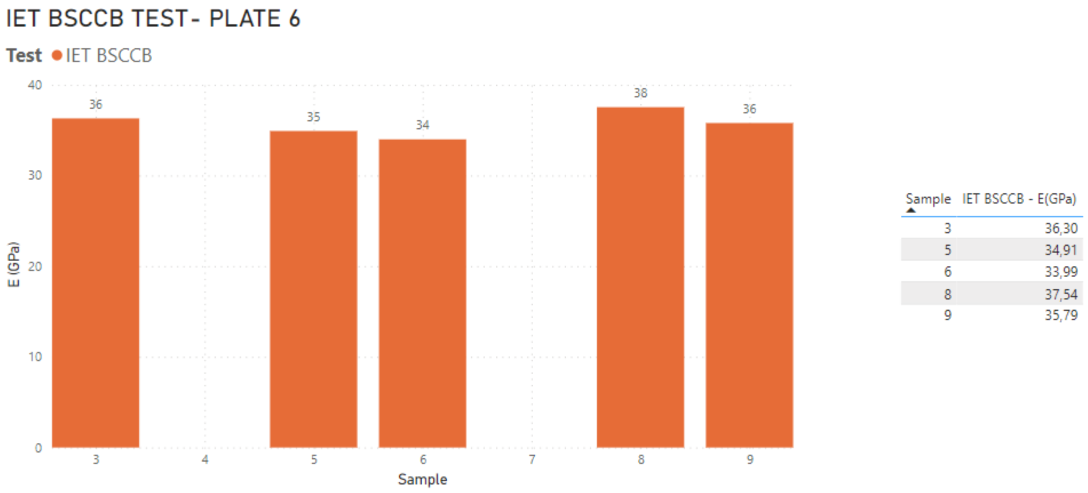

Sample	IET BSCCB - E(GPa)
3	36,30
5	34,91
6	33,99
8	37,54
9	35,79

Figure 4.39. Calculated Young's moduli of samples of plate 6 from an IET test with BSCCB set up.

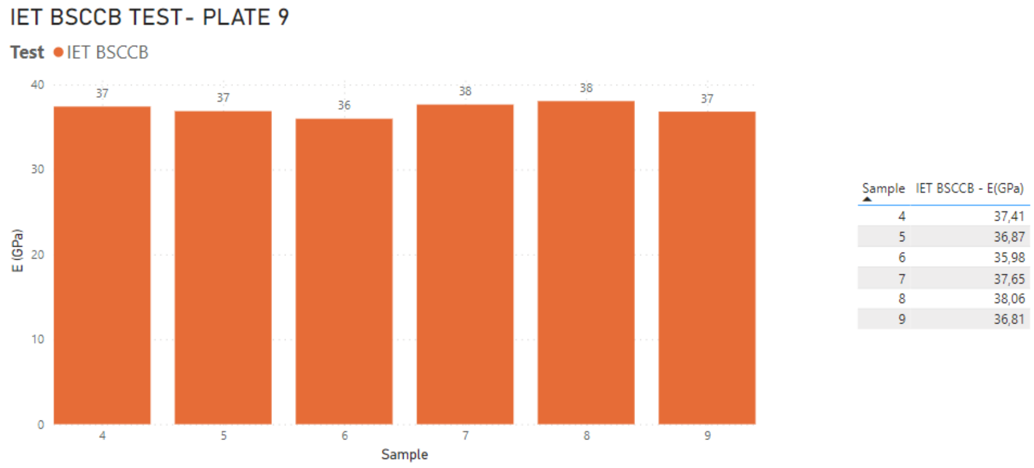

Sample	IET BSCCB - E(GPa)
4	37,41
5	36,87
6	35,98
7	37,65
8	38,06
9	36,81

Figure 4.40. Calculated Young's moduli of samples of plate 9 from an IET test with BSCCB set up.

In the final chapter, the modulus values calculated using the two different setups will be compared, and appropriate considerations will be made.

5. STATIC THREE-POINT BENDING TESTS

5.1. *INTRODUCTION*

Three-point bending tests are used to obtain mechanical characterization of various materials. They are based on the application of a load, and depending on the material's behavior, different information can be obtained from stress-strain curves, such as flexural strength or Young's modulus, and in general whether the material exhibits a more ductile or more linearly elastic behavior.

In this study, three-point bending tests (referred to as 3PB) will be conducted on prism-shaped specimens using the Instron 5965 (**Figure 5.1**).

Figure 5.1. Instron 5965, used for 3-point bending tests.

The reference standard upon which this study is based, and the standard used by the Instron 5965 software for calculating flexural stress, is ASTM C1161-02c [20]. The setup used is depicted in the standard, and below, in **Figure 5.2**, a schematic representation of it is shown.

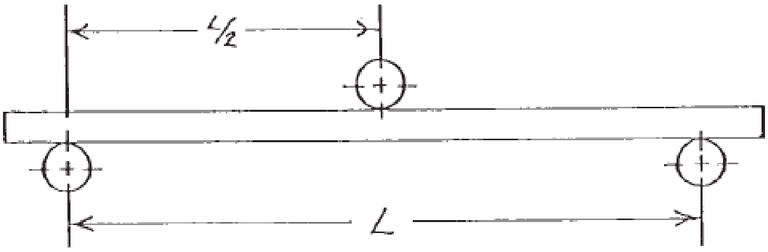

Figure 5.2. Schematic view of the set up used for 3-point bending tests [20].

L is the span, which is the distance between the supports on which the specimen is placed. It depends on the geometric parameters of the specimen and is determined based on specific geometric ratios derived from the normative BS ISO 6721-5:2019 [21], as shown below:

$L/b > 3$

$L/d > 8$

Where:

b = specimen width

d = specimen thickness.

These ratios are related to a simply supported specimen, that is the set-up of the present study. These recommended geometry relations are proposed to limit the influence of shear stresses during the test; a low span-thickness ratio increases the probability that the sample will fail in shear.

Regarding the flexural stress, it is derived from the formula (5.1) proposed below, also derived from ASTM C1161-02c standard.

$$S = \frac{3PL}{2bd^2} \tag{5.1}$$

Where:

P = break force

L = outer (support) span

b = specimen width

d = specimen thickness.

It's important to note the strong dependency of this parameter on the specimen's geometry, which is why precision is crucial both in the specimen manufacturing phase and in the measurement of its dimensions.

In this study, the three-point static bending tests were used for two purposes:

1. To obtain an average rupture load value of the samples for using it as a reference in dynamic tests with DMA (Dynamic Mechanical Analysis); the samples were subjected to bending until rupture, and the average rupture load for the material was derived from the different maximum stress values reached.
2. To derive Young's modulus from the stress-strain curves for comparison both with that measured by IET tests and with the storage modulus obtained from DMA tests. In this case, the stress was not pushed to the sample's rupture, but only until reaching 20% of the rupture load, which was determined by the previous static tests.

5.2. EXPERIMENTAL TESTS

For both tests, Instron 5965, shown in **Figure 5.1**, was used.

For the first purpose, all samples belonging to three plates were brought to rupture: plates 1, 2, and 8. The first two were porous, while the 8th was non-porous. The dimensions of the samples were the same as those used for the IET tests, namely: 160x20x10 mm. Plates with different porosity were tested to see if this parameter could influence the mechanical properties of the tested samples. In **Figure 5.3** and **Figure 5.4**, presented below, the results of these initial tests are reported.

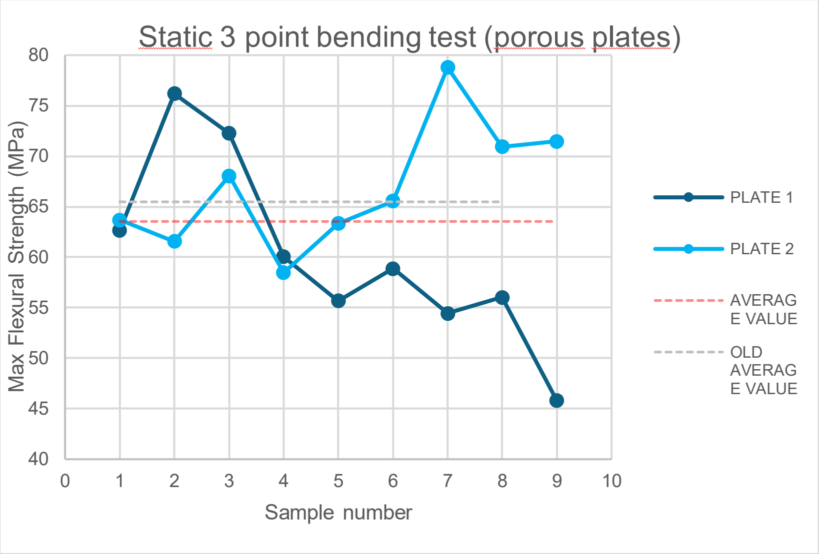

Figure 5.3. Static 3-point bending test for porous plates (1,2).

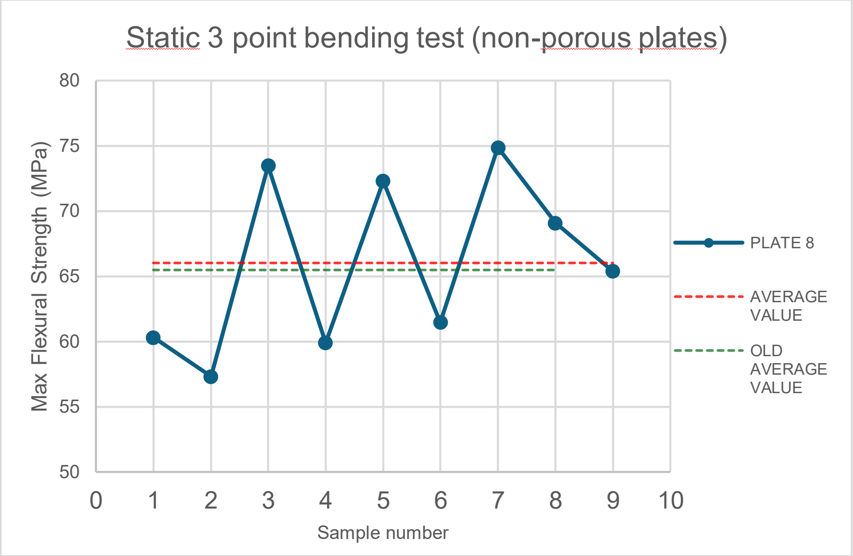

Figure 5.4. Static 3-point bending test for non-porous plate (8).

Table 5.1 provides an overview of all the data collected for this purpose.

Table 5.1. Average maximum strength values for plates 1,2,8 and comparison with old values.

		Average value of maximum strength (MPa)	**Standard deviation (MPa)**
New values	Porous plates (1,2)	63,54	8,37
	Non porous plate (8)	66,02	6,61
Old values		65,48	14,62

From **Table 5.1**, it is evident that the averages of rupture stresses are very similar between porous and non-porous plates, demonstrating that this amount of porosity does not significantly affect the flexural strength of these material. Additionally, in the last row, the values from static flexural tests on the same types of samples but obtained by a different operator are reported; the rupture stress is comparable to the new values collected in the present study. In the subsequent DMA tests, 64 MPa was used as a reference for maximum rupture stress.

Moving to the second purpose for which static three-point flexural tests were used, six samples from plate 9 were tested, also of the dimensions specified previously. Additionally, a steel bar with dimensions of 200x25x4 mm was tested (**Figure 5.5**); this was done to have a point of comparison between the tests conducted with the material under investigation and another material with known characteristics, thus providing an idea of the effectiveness of the various testing methods. The maximum stress set for these tests is 20% of the average rupture load, which is 64 MPa, approximately corresponding to 13 MPa. Therefore, the software of Instron 5965 was set up to stop the test upon reaching this stress, thus avoiding irreversible damage to the material. For the steel bar, the same load limit used for the composite samples was used to ensure consistent loading conditions; however, since it corresponds to 20% of the rupture load of the composite specimens, it may not correspond to 20% of the actual rupture load of the steel bar, which understandably will have higher rupture stress than the composite.

Figure 5.5. Steel bar tested with 3PB.

In the final chapter, the values of Young's modulus and storage modulus obtained from the various tests (IET, DMA, 3PB) will be compared, and using a different material like steel allows for an understanding of the reproducibility of the obtained values on other materials.
Below are the curves related to the static three-point bending tests and Young's modulus values derived, for six samples from plate 9 and from the steel bar (**Figures 5.6 - 5.9**).

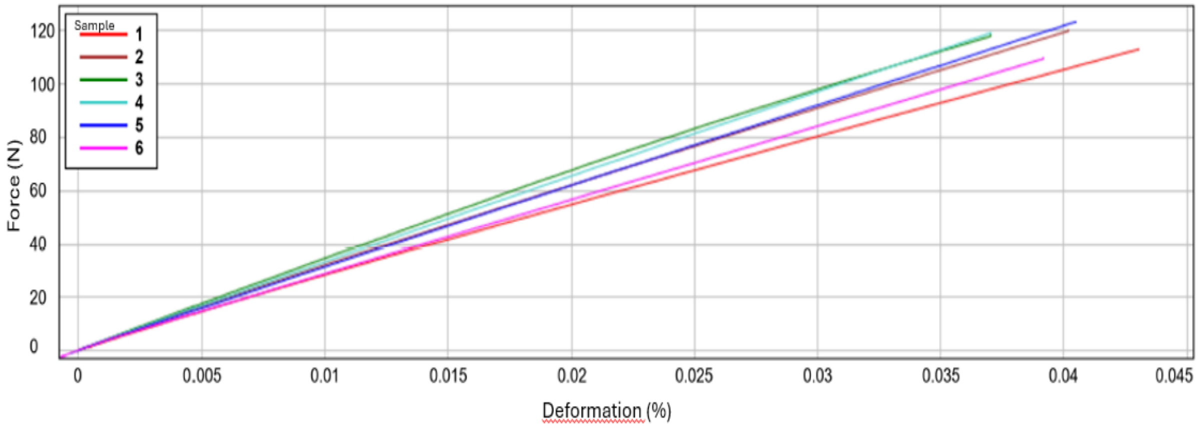

Figure 5.6. Force-deformation curves for six samples of plate 9.

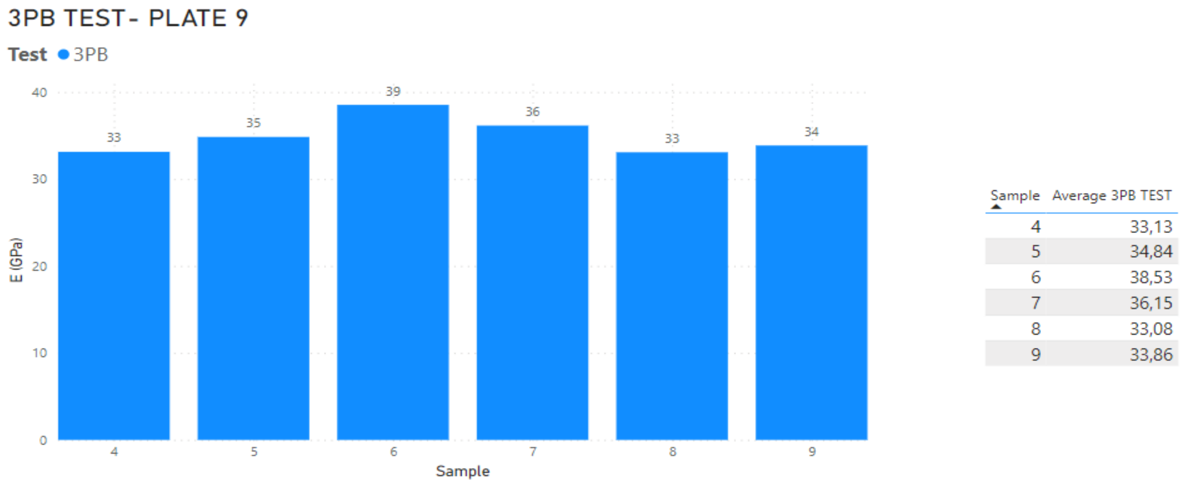

Sample	Average 3PB TEST
4	33,13
5	34,84
6	38,53
7	36,15
8	33,08
9	33,86

Figure 5.7. Young's modulus values calculated from force-deformation curves of tested samples of plate 9.

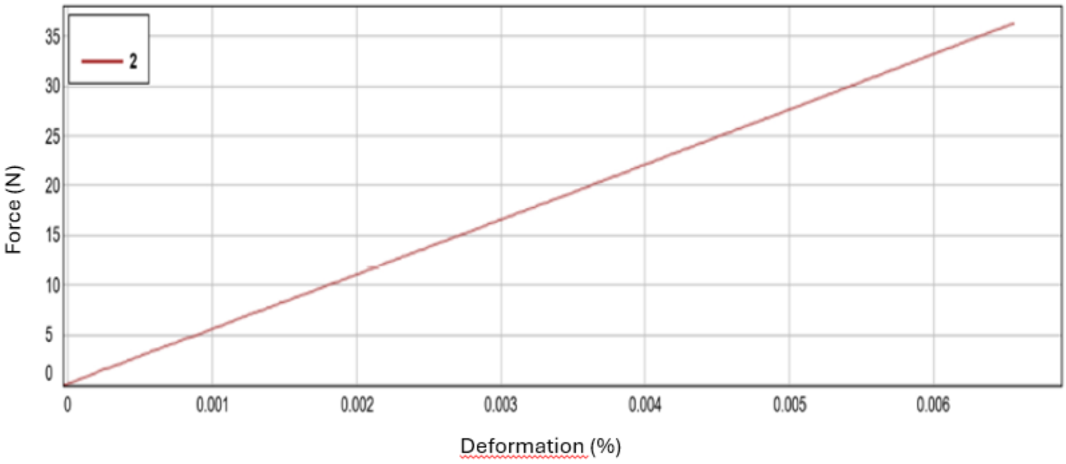

Figure 5.8. Force-deformation curve for the steel bar.

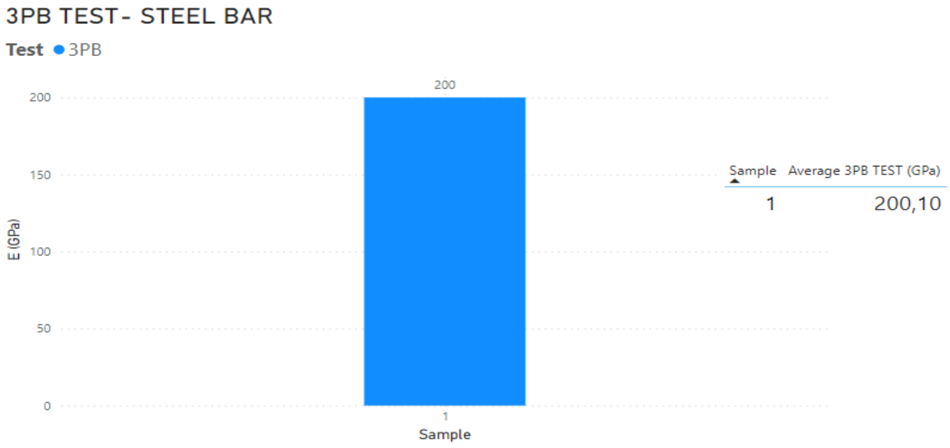

Figure 5.9. Young’s modulus value calculated from force-deformation curve of tested steel bar.

6. DYNAMIC MECHANICAL ANALYSIS (DMA)

6.1. *INTRODUCTION*

Dynamic Mechanical Analysis (DMA) is based on the application of dynamic stress to a specimen to determine various properties. The main purpose is the study of the viscoelastic behavior of intrinsic polymer materials or even composites. In this study, however, DMA is used to characterize the mechanical behavior of a ceramic matrix composite material, which does not fully correspond to the usual scope of this type of test. Nevertheless, it provides useful information on how the material reacts to cyclic stresses. The principle underlying DMA is shown in **Figure 6.1** [22].

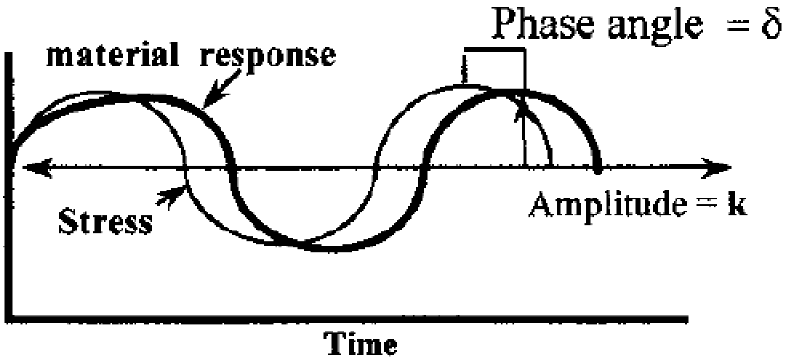

Figure 6.1. Schematic representation of sinusoidal stress and corresponding strain of the material [22].

The material is subjected to a sinusoidal stress of amplitude k, with a certain frequency ω, and based on its mechanical characteristics, it responds by deforming sinusoidally but not in phase with the stress, with a phase shift given by δ, that is the phase angle. The closer the phase angle δ is to zero, the more the material's deformation will be in phase with the applied stress, implying a tendency toward elastic behavior; the closer δ is to 90°, the more the material tends to behave viscously. Based on this parameter, important information about the material's behavior can be obtained. **Figure 6.2** represents deformation curves in relation to stress curves in the extreme cases of complete elasticity (a) and complete viscosity (b).

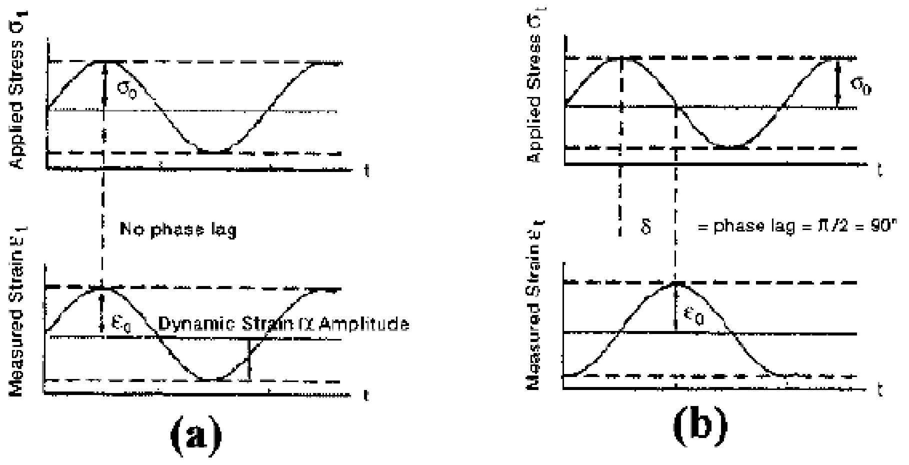

Figure 6.2. Deformation curves for total elastic material (a) and for completely viscous material (b) [22].

Materials like polymers tend to have a phase angle δ significantly greater than more brittle materials like ceramics. Specifically, the ceramic matrix composite material studied in this project is quite close to the case of complete elasticity.

From a more mathematical perspective, DMA is based on a sinusoidal stress represented by the following equation:

$$\sigma = \sigma_0 \sin \omega t \qquad (6.1)$$

This stress corresponds to a strain:

$$\varepsilon(t) = \varepsilon_0 \sin(\omega t + \delta) \qquad (6.2)$$

Which can be rewritten as:

$$\varepsilon(t) = \varepsilon_0 [\sin(\omega t)\cos\delta + \cos(\omega t)\sin\delta] \qquad (6.3)$$

By dividing equation (6.3), the in-phase and out-of-phase deformations, corresponding to the curves presented in Figure 6.2 (a and b) can be derived, resulting in the following relationships:

$$\varepsilon' = \varepsilon_0 \sin\delta \qquad (6.4)$$

$$\varepsilon'' = \varepsilon_0 \cos\delta \qquad (6.5)$$

The first equation (6.4) relates to in-phase deformation, which corresponds to the deformation induced by the accumulation of energy resulting from the stress, while the second (6.5) is related to the deformation associated with the loss of energy in the form of heat or rearrangements of the sample's internal structure. In this way, these deformations can be correlated with corresponding stiffness moduli, defining the storage modulus (E') and the loss modulus (E''), which respectively express a material's tendency to absorb energy elastically and to dissipate it following the application of a dynamic load.

Below are the equations for the two moduli, derived from mathematical treatments of the phenomenon. The first one concerns the storage modulus E' (6.6), while the second one concerns the loss modulus E'' (6.7).

$$E' = (\sigma_0 / \varepsilon_0) \cos \delta \tag{6.6}$$

$$E'' = (\sigma_0 / \varepsilon_0) \sin \delta \tag{6.7}$$

These two quantities together constitute the dynamic or complex modulus E*, which also depends on the frequency of application of the sinusoidal stress (ω).

$$E^*(\omega) = E'(\omega) + iE''(\omega) \tag{6.8}$$

Finally, from the tangent of the phase angle, the two quantities can be correlated to express damping, and thus how much the material tends to dampen the stress it undergoes through modifications of its internal molecular structure.

$$\tan\delta = E''/E' \tag{6.9}$$

After presenting the principles underlying a dynamic mechanical test, the present study focused on the storage modulus of the material (E'), as it is the predominant component of the complex modulus, since the behavior of the ceramic matrix composite is almost elastic. The experimental DMA tests were conducted both at room temperature (RT) and at high temperatures (HT), up to 250°C, to analyze the material's behavior at different temperatures.

6.2. EXPERIMENTAL TESTS

6.2.1 INTRODUCTION

To perform DMA tests, Instron 8802 (**Figure 6.3**) was used.

Figure 6.3. Instron 8802 for DMA 3-point bending tests.

The DMA-tested specimens are of the same type as those seen in previous chapters, with the "small" geometry, i.e., 160x20x10 mm, as depicted in Figure 6.12 (left). The setup is the same as for the three-point bending tests seen in Chapter 7; thus, a span of 140 mm was used to comply with the ratios prescribed by the standard BS ISO 6721-5:2019 [21] to limit the influence of shear stresses on the test.

Each DMA test was conducted at a frequency of 20 Hz and 10000 load cycles, to have a good balance between the quantity of collected data and the acquisition time. A lower frequency, such as 1 Hz with the same number of load cycles, implies a greater amount of data collected over time but also an increase in the duration of each test. The software of Instron 8802 allowed for tests where different loads were applied successively or in a specific order, enabling an analysis of the specimen's behavior under various test conditions.

The procedure for determining the loads to be applied to the specimens starts with the acquisition of the maximum bending stress, determined from the three-point bending tests until failure seen in Chapter 5. As shown, for the studied specimens, the maximum stress was found to be around 64 MPa. From this value and using the relationship regarding the bending stress for rectangular cross-section specimens proposed in Chapter 5 (formula 5.1), the corresponding maximum force that the specimens can withstand was determined to be approximately 605 N. To have an idea of the storage modulus (E') and loss modulus (E") of the specimen without reaching failure, it is necessary to apply a dynamic load that does not exceed 50% of the failure load. Therefore, for each specimen, load values corresponding to 20%, 30%, 40%, and 50% of the failure load were used. As can be seen from formula 1 in Chapter 5, these values depend on the geometry of the specimen and are therefore specific to each one, although the values are quite similar. Each type of applied load was dynamically imparted with a semi-amplitude of the sinusoidal stress of 10%, i.e., half of the load itself. An example of the loads used in the DMA tests is provided in **Table 6.1** below.

Table 6.1. Example of DMA load values for a “small” geometry sample.

% Load	% Range	Stress (MPa)	Load (N)	Half amp	Half amplitude (N)	Load min (N)	Load max (N)
10	10±5%	6	57	0.05	29	27	86
20	20±10%	13	113	0.10	58	55	172
30	30±10%	19	170	0.10	58	111	228
40	40±10%	25	226	0.10	58	168	285
50	50±10%	32	283	0.10	58	225	341

Loads lower than 20% were not applied. The reason for this choice is that the Instron 8802 mounts a load cell of 100 kN, and therefore, a 10% load would be difficult to apply because it is too small for such a load cell; as seen from the table, with such a load, the minimum applied force reaches 27 N, which is approximately 0.03% of the maximum load that can be applied with the load cell. In general, even loads from 20% to 50% are very small for a machine of this capacity but are more feasible.

Before proceeding with the DMA tests, it is necessary to perform PID (Proportional, Integral, and Derivative) control of the machine [23]. In practice, the conditions of the DMA test to be conducted are simulated by imposing sinusoidal stress with a certain frequency (in this study, a load of 500 N with a semi-amplitude of 55 N and a frequency of 1 Hz) on a sample identical to those that will be tested, and the PID controller allows the machine to be set based on the nature of the tested material, proposing coefficients (P, I, D) to be inserted into the system software so that the output data are corrected directly by these coefficients. In summary, PID adjusts the output results based on:

- the value of the error signal (Proportional action-P);
- how the error signal varies (Integral action-I);
- how quickly the error signal varies (Derivative action-D).

For a sample of CCM material with small geometry, the values resulting from the PID control are:

P = 41; I = 10.031; D = 0.22

Once the Instron 8802 is set up, the sample is placed on the steel supports to comply as accurately as possible with the 140 mm span; the final setup is shown in **Figure 6.4**.

Figure 6.4. Set up of DMA 3-point bending test at room temperature with Instron 8802.

6.2.2 TEST DMA ROOM TEMPERATURE (RT)

With the setup shown in **Figure 6.4**, various types of tests were conducted at room temperature to study the material's response to varying dynamic load intensities. The frequency and number of load cycles remained unchanged (20 Hz and 10000 cycles), only the load value and the types of application of the different loads varied.

The conducted tests will be referred to by numerical identifiers to better identify the applied load method. Below, in **Figure 6.5**, a schematic view of all the DMA RT tests is presented:

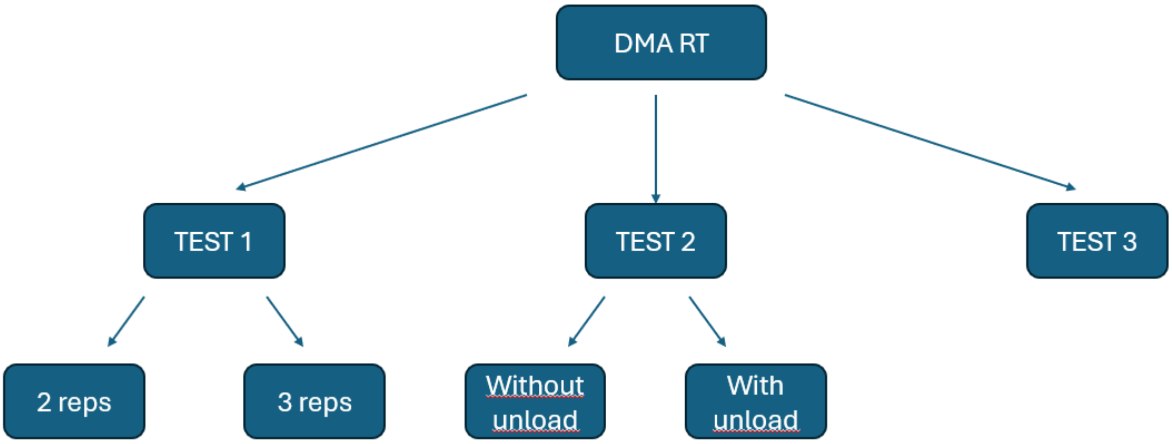

Figure 6.5. Schematic view of all the DMA RT tests.

TEST 1: This test involves applying a load cycle where the specimen is subjected to increasing loads from 20% to 50%, as depicted in the schematic representation below (**Figure 6.6**).

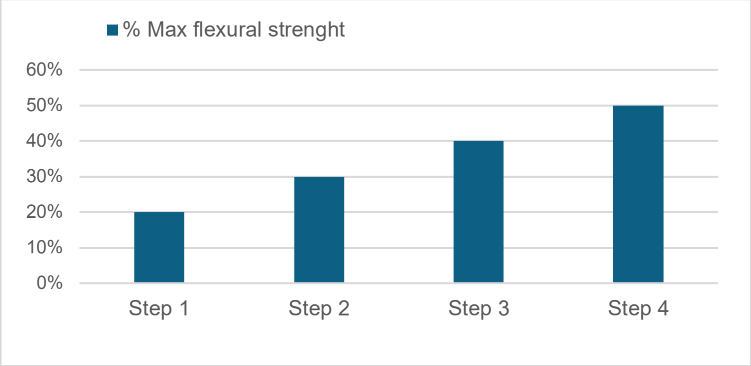

Figure 6.6. Schematic view of the complete load cycle test (TEST 1).

Some specimens underwent two repetitions of the entire load cycle while others underwent three. This approach aims to gather information on how the specimen responds to increasing dynamic load intensity.

The software outputs a graph showing the variation of the storage modulus (E') and loss modulus (E") with the number of load cycles, which are 10000 for each load value (**Figure 6.7**).

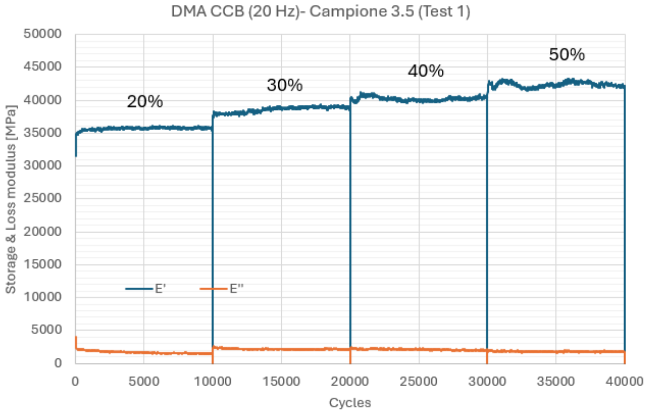

Figure 6.7. Example of Storage and Loss modulus charts from TEST 1.

From the curves shown in **Figure 6.7**, it can be observed that the load increased every 10000 cycles. For each load step, the average values of E' and E" were obtained with their respective standard deviations for each tested specimen and consequently for the entire plate.

The resulting graphs with all the collected data are shown in **Figure 6.8** for specimens that underwent two repetitions of the complete cycle and in **Figure 6.9** for those that underwent three repetitions. Only E' is displayed in these graphs as it is more central to the thesis objectives.

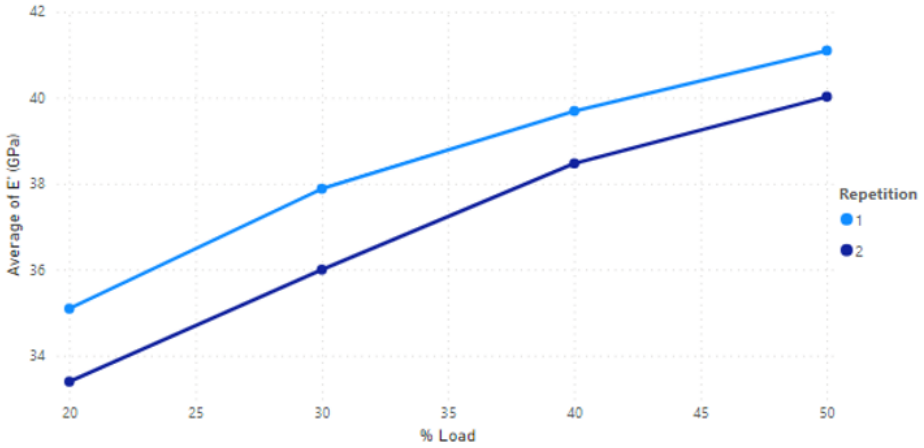

Figure 6.8. Variation of the average storage modulus E’ with the load for a TEST 1 with 2 reps.

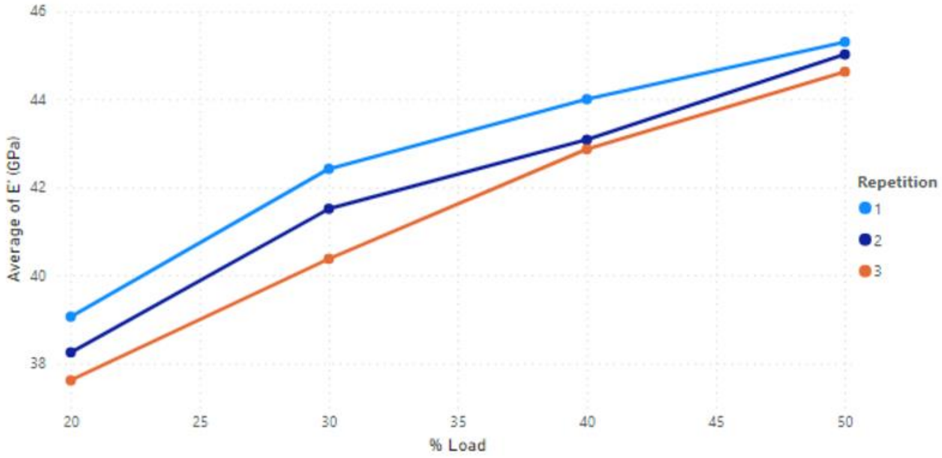

Figure 6.9. Variation of the average storage modulus E’ with the load for a TEST 1 with 3 reps.

The numerical values and variations of E' between repetitions are collected in the following tables (**Table 6.2** and **Table 6.3**).

Table 6.2. Average E’ for each load and each repetition with standard deviation and variation between the repetitions (TEST 1- 2 reps).

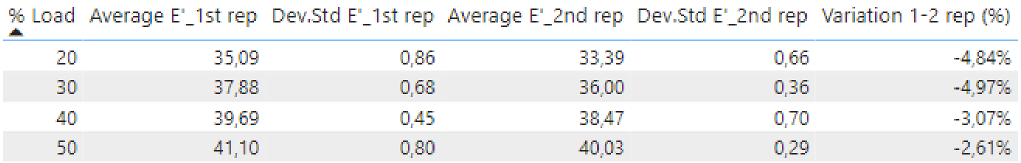

% Load	Average E'_1st rep	Dev.Std E'_1st rep	Average E'_2nd rep	Dev.Std E'_2nd rep	Variation 1-2 rep (%)
20	35,09	0,86	33,39	0,66	-4,84%
30	37,88	0,68	36,00	0,36	-4,97%
40	39,69	0,45	38,47	0,70	-3,07%
50	41,10	0,80	40,03	0,29	-2,61%

Table 6.3. Average E’ for each load and each repetition with standard deviation and variation between the reps (TEST 1- 3 reps).

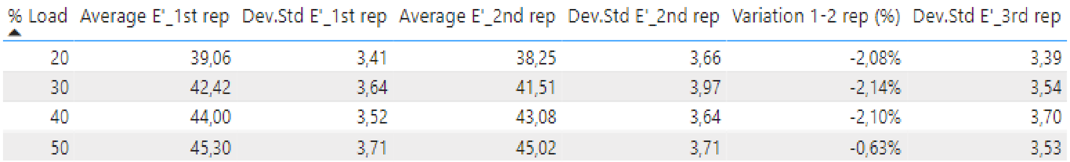

% Load	Average E'_1st rep	Dev.Std E'_1st rep	Average E'_2nd rep	Dev.Std E'_2nd rep	Variation 1-2 rep (%)	Dev.Std E'_3rd rep
20	39,06	3,41	38,25	3,66	-2,08%	3,39
30	42,42	3,64	41,51	3,97	-2,14%	3,54
40	44,00	3,52	43,08	3,64	-2,10%	3,70
50	45,30	3,71	45,02	3,71	-0,63%	3,53

It can be observed from the two curves that the maximum variation in the storage modulus occurs at 20%. This indicates that each load cycle damages the material more, compromising its initial stiffness. Another important piece of information is the increasing trend of the curves; E' tends to increase with the load intensity because dynamic stresses cause a compaction effect on the material structure. However, this effect occurs only during the loading cycle, and once it ends, the material relaxes and it is irreversibly damaged.

TEST 2: This test involves repeating the same load two or three times before moving on to the next one. It was conducted in two modes:

- Continuous cycle (**without unloading**): In this mode, the load transitions from one intensity to the next without any interruptions or unloading phase between the steps. The schematic representation of this test is shown in **Figure 6.10**.

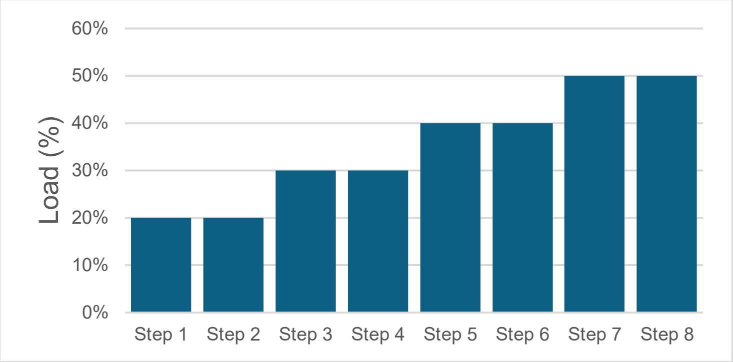

Figure 6.10. Schematic view of TEST 2 without unloading.

The results for this type of test were collected from the following curves (**Figure 6.11**). Two repetitions of the load cycle described were applied to each tested specimen, as shown in **Figure 6.10**.

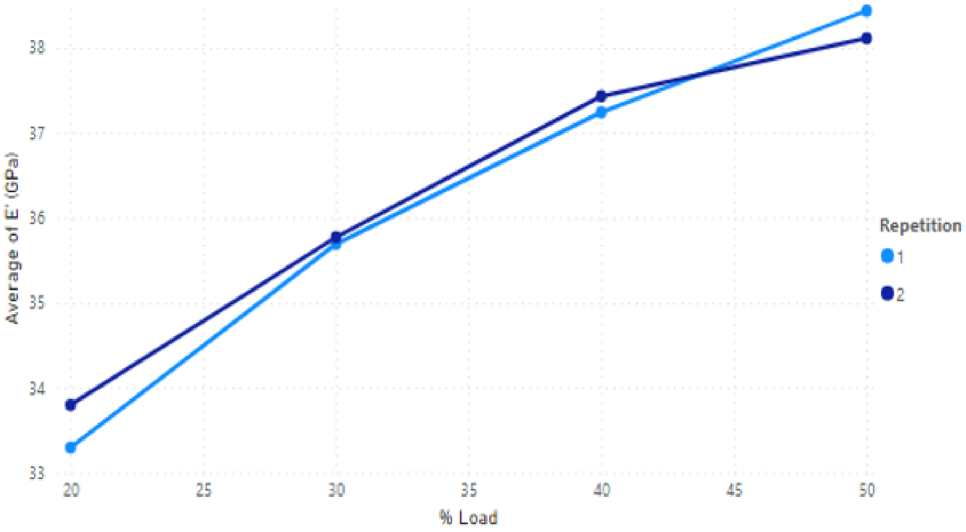

Figure 6.11. Results from TEST 2 without unloading.

These results were obtained from tests conducted on two specimens from plate 4. The variations between the average E' values are shown in the following table (**Table 6.4**).

Table 6.4. Average E’ values from two repetitions of TEST 2 without unloading and percentage variation.

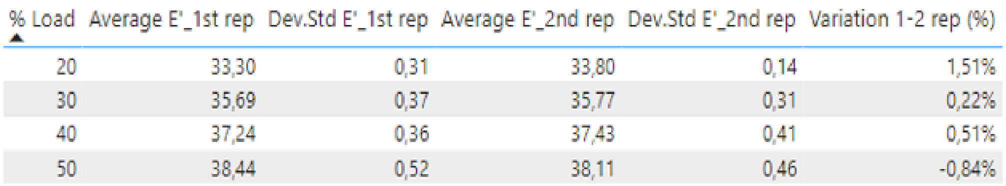

% Load	Average E'_1st rep	Dev.Std E'_1st rep	Average E'_2nd rep	Dev.Std E'_2nd rep	Variation 1-2 rep (%)
20	33,30	0,31	33,80	0,14	1,51%
30	35,69	0,37	35,77	0,31	0,22%
40	37,24	0,36	37,43	0,41	0,51%
50	38,44	0,52	38,11	0,46	-0,84%

In this case, as seen in TEST 1, an increase in the modulus with the load, is observed. There is a relatively small variation between the repetitions of the load cycle. The notable aspect is the increase in the modulus at 20% of the load between the first and second repetitions, indicating that the initial load cycle tends to stiffen the material's crystalline structure. However, as the cycle continues, there is a progressive decrease in E'.

- **With unloading** between each load application (**Figure 6.12**).

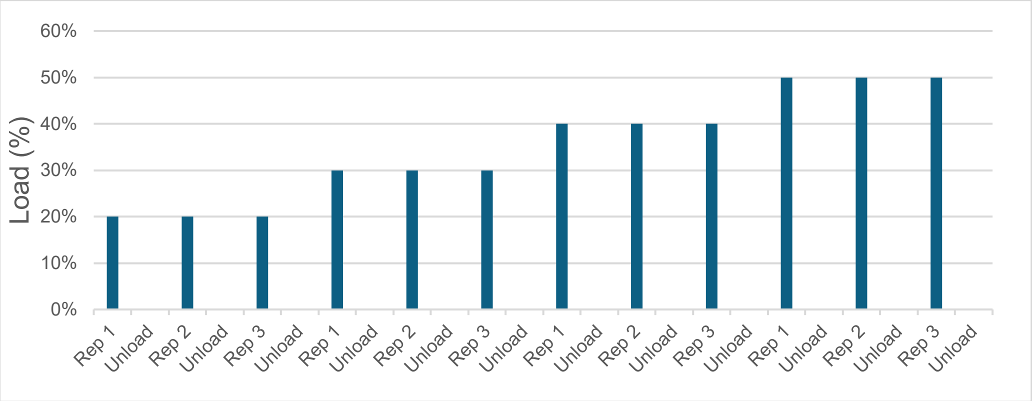

Figure 6.12. Schematic view of TEST 2 with unload.

As seen in **Figure 6.12**, three repetitions of the same load were conducted before moving on to the next one. The results obtained from the unloading phase pertain to three different specimens from the same plate. **Figure 6.13** presents the data concerning only one of three tested specimens, as the others give similar results.

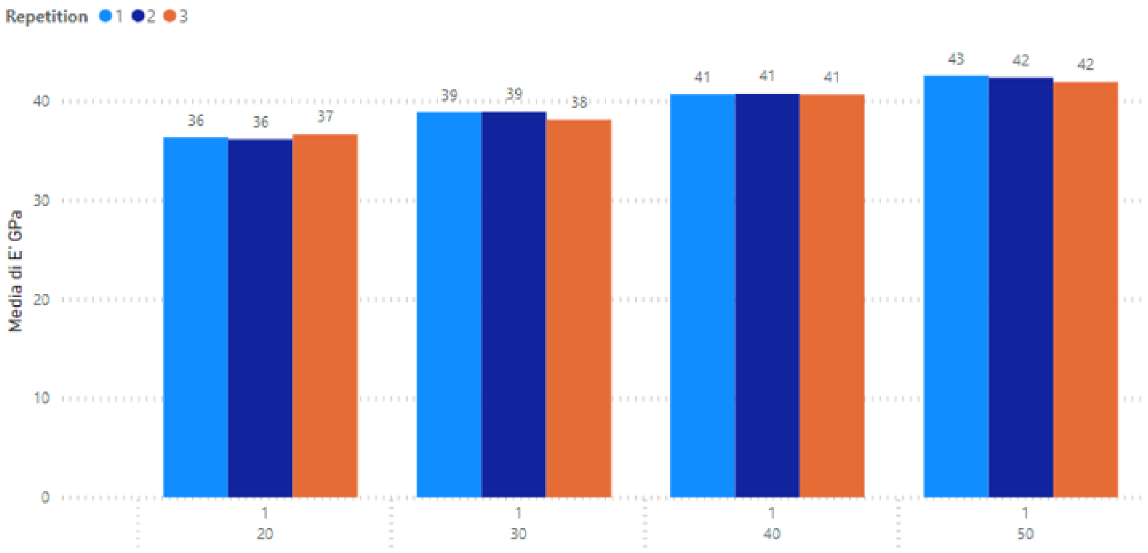

Figure 6.13. Results of TEST 2 with unloading.

Table 6.5 summarizes all the results and also includes the variations between the E' values.

Table 6.5. Average E’ values from TEST 2 without unloading and percentage variation.

SAMPLE 1				
%LOAD	REPETITION	E'(GPa)	Dev std E' (Gpa)	TOTAL VARIATION OF E' 1-3 (%)
20	1	36.31	0.77	0.91%
	2	36.12	0.35	
	3	36.64	0.31	
30	1	38.86	0.33	-1.96%
	2	38.90	0.18	
	3	38.10	0.47	
40	1	40.68	0.23	-0.07%
	2	40.72	0.17	
	3	40.66	0.15	
50	1	42.53	0.41	-1.50%
	2	42.35	0.46	
	3	41.89	0.19	

It is noted that in this case as well, the specimen stiffens under higher loads, but the individual load does not influence the storage modulus significantly; indeed, its value remains relatively constant across different repetitions of the same load. Thanks to the unloading phase, the specimen is not affected by the repetition of the same load but only by its intensity.

TEST 3: It is based on progressively applying load cycles in which a higher load is added to each repetition. To better understand the structure of this test, a schematic view is shown below (**Figure 6.14**).

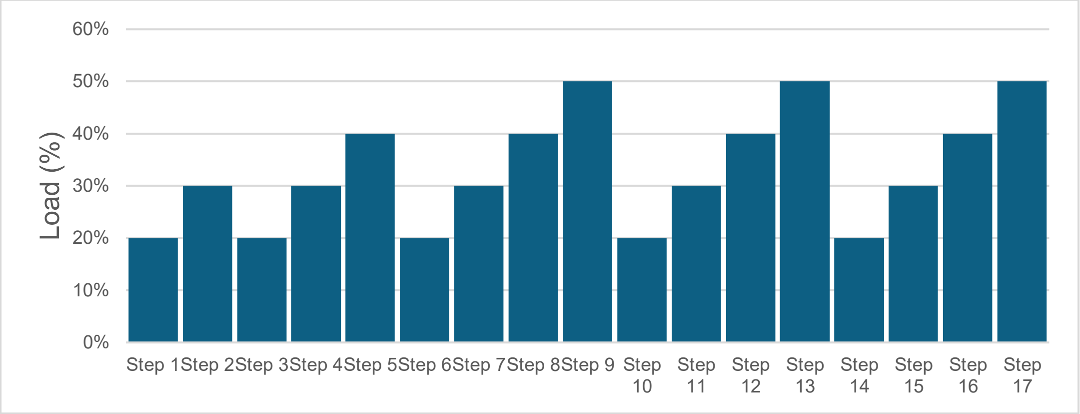

Figure 6.14. Schematic view of TEST 3.

In practice, the stress cycle is progressively implemented with higher loads until reaching the 50% load. Subsequently, two complete cycles from 20% to 50% load are applied. The entire process is carried out continuously, without an unloading phase between repetitions. The purpose is to study which load is most detrimental to the specimen, or at which load a more pronounced variation in the storage modulus occurs. Three specimens from a plate were tested in this manner, and the results obtained are summarized in the following diagram (**Figure 6.15**).

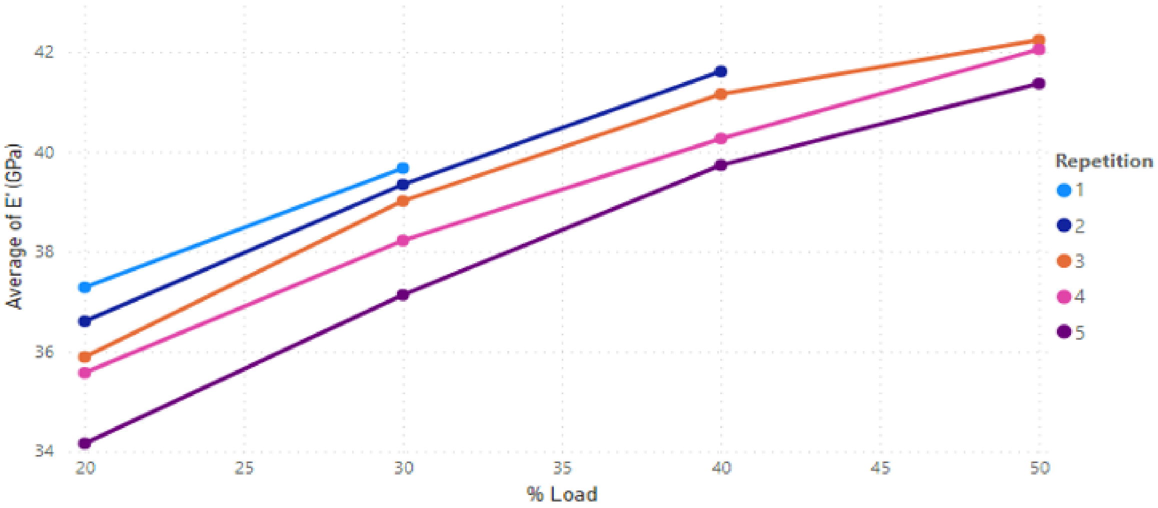

Figure 6.15. Results from TEST 3.

It can be observed that the load that seems to have the most influence on E' is 40%, as between the second and third repetitions, the value of the storage modulus at 20% experiences a more pronounced decrease compared to other loads. Finally, from the E' value at 20% for the fifth repetition, it is demonstrated how the repetition of multiple complete load cycles significantly damages the specimen, confirming the results obtained from TEST 1. This is evident in **Table 6.6**, where the percentage variations of E' for each load between the repetitions of the stress cycles are collected.

Table 6.6. Percentage variations of E’ between the repetition from TEST 3.

% Load	Variation 1-2 rep (%)	Variation 2-3 rep (%)	Variation 3-4 rep (%)	Variation 4-5 rep (%)
20	-1.80%	-1.97%	-0.89%	-3.97%
30	-0.83%	-0.84%	-2.03%	-2.84%
40	x	-1.11%	-2.16%	-1.31%
50	x	x	-0.43%	-1.63%

Finally, the average E' values are detailed in **Table 6.7** for TEST 3.

Table 6.7. Resume of E' values with related standard deviation for all the samples tested with TEST 3.

Repetition	% Load	Average E' (GPa)	Dev.Std E' (GPa)
1	20	37.28	2.54
	30	39.67	2.91
2	20	36.61	2.66
	30	39.34	3.09
	40	41.61	3.21
3	20	35.89	2.51
	30	39.01	3.01
	40	41.15	2.95
	50	42.23	3.43
4	20	35.57	2.69
	30	38.22	3.24
	40	40.26	3.21
	50	42.05	3.42
5	20	34.16	0.42
	30	37.13	0.29
	40	39.73	0.24
	50	41.36	0.23

6.2.3 TEST DMA HIGH TEMPERATURE (HT)

After analyzing the material's behavior through dynamic tests at room temperature, an experimental study was conducted on the samples' response to dynamic three-point bending loads at elevated temperatures. These tests aim to provide further insights into the temperature-dependent behavior of the carbon-ceramic material and allow obtaining results comparable to those from the HT tests conducted using IET. This approach helps confirm how the material responds to high temperatures. Additionally, applying a dynamic load at high temperatures

simulates the operational conditions of the brake disc. Indeed, discs are often subjected to successive braking events that approximate dynamic loads and can generate significant heat.
To perform the DMA tests at high temperatures, an Instron 8802 was used, the same one used for room temperature tests, around which a furnace capable of applying a temperature gradient was mounted (**Figure 6.16**).

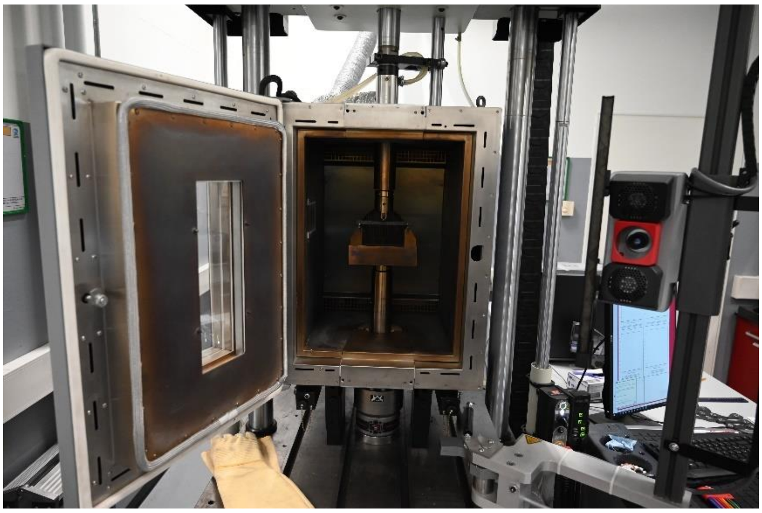

Figure 6.16. Instron 8802 with DMA HT set up.

The operational setup, including arrangement of samples in the machine, geometry of the samples, and settings of dynamic loads (oscillation frequency and number of cycles), are identical to those used in the DMA RT tests.
Two types of tests were conducted in the DMA HT experiments.
TEST HT 1: This test involves applying 20% of failure load on a sample while imposing a temperature gradient ranging from 25 °C to 250 °C. The target temperatures are 25 °C, 100 °C, 150 °C, 200 °C, and 250 °C. These temperatures were chosen to compare the results with those of the IET HT tests up to 250°C. After waiting for the furnace temperature to stabilize around the set value, a cyclic load equivalent to 20% ± 10% of the rupture load was applied (1000 cycles at 20 Hz) three times, unloading at the end of each application. This procedure collected three average values of E' for each temperature, providing a more reliable average storage modulus value. **Figure 6.17** provides a schematic representation of TEST HT 1.

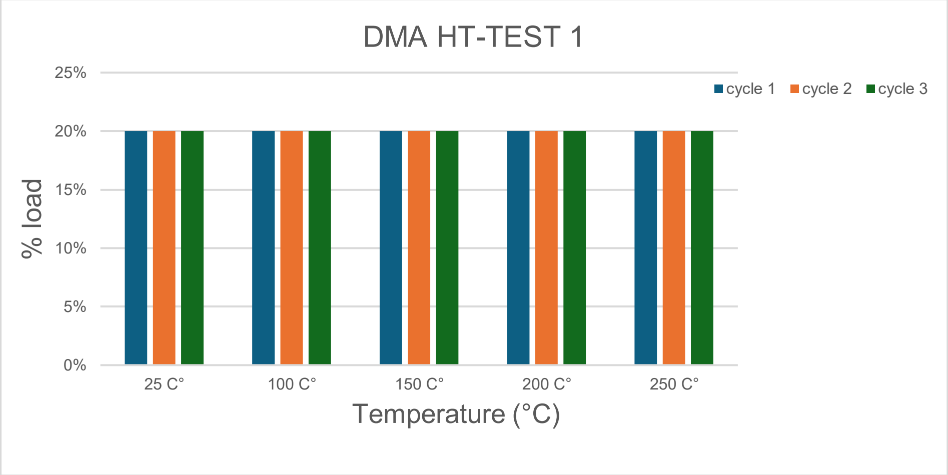

Figure 6.17. Schematic view of TEST HT 1.

The entire TEST HT 1 was applied three times on the same sample to analyze the effect of temperature on the material properties, as previously done with the IET tests.

Figures 6.18 and **6.19** display the results obtained for samples 1 and 2 of plate 11, along with the corresponding tables summarizing the data obtained for all cycles (**Tables 6.8** and **6.9**).

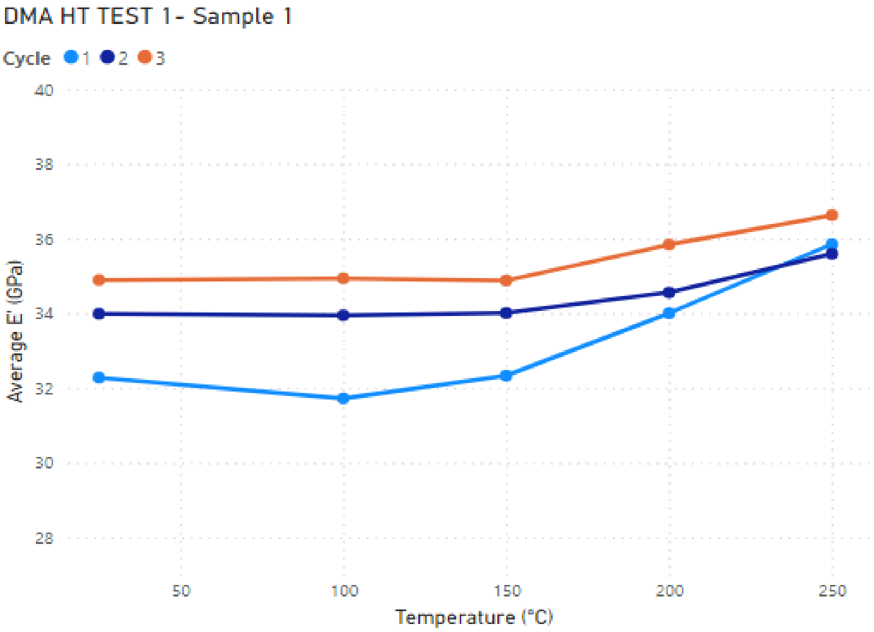

Figure 6.18. Storage modulus curves from TEST HT 1 applied to sample 1 of plate 11.

Table 6.8. Results from TEST HT 1 applied to sample 1 of plate 11.

Temperature (°C)	Average E' (GPa)						Variation 1-2 %	Variation 2-3 %
	cycle 1	dev. Std 1	cycle 2	dev. Std 2	cycle 3	dev. Std 3		
25	32.28	0.60	33.99	0.20	34.89	0.53	5.0%	3.0%
100	31.72	0.46	33.95	0.18	34.94	0.37	7.0%	2.9%
150	32.33	0.47	33.97	0.20	34.88	0.34	5.1%	2.7%
200	34.00	0.32	34.56	0.22	35.84	0.34	1.6%	3.7%
250	35.85	0.36	35.59	0.28	36.63	0.31	-0.7%	2.9%

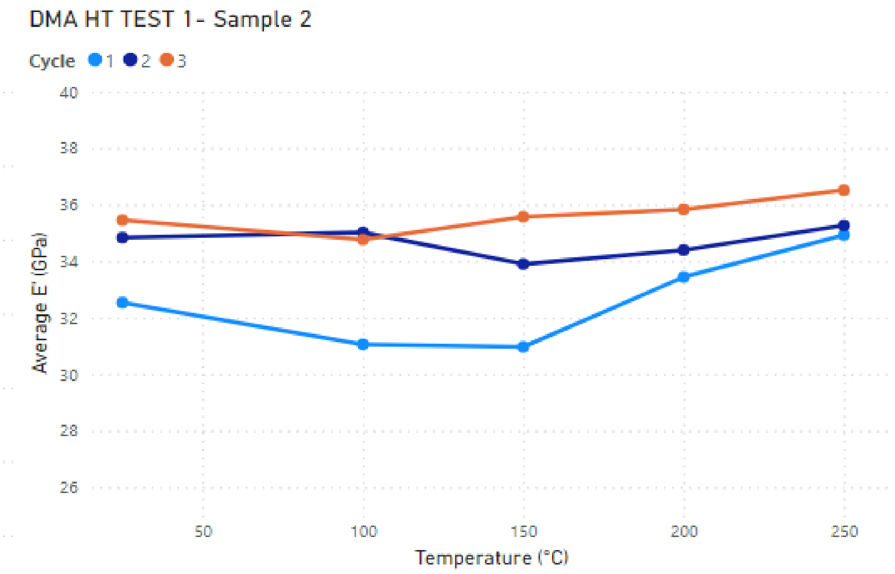

Figure 6.19. Storage modulus curves from TEST HT 1 applied to sample 2 of plate 11.

Table 6.9. Results from TEST HT 1 applied to sample 2 of plate 11.

Temperature (°C)	Average E(GPa)						Variation 1-2 %	Variation 2-3 %
	cycle 1	dev. Std	cycle 2	dev. Std	cycle 3	dev. Std 3		
25	32.54	0.24	34.84	0.24	35.46	0.37	7.1%	2.0%
100	31.06	0.23	35.02	0.18	34.76	0.36	12.7%	-0.7%
150	30.97	0.24	33.90	0.28	35.58	0.29	9.5%	5.0%
200	33.44	0.29	34.40	0.26	35.84	0.28	2.9%	4.2%
250	34.93	0.27	35.27	0.24	36.51	0.33	1.0%	3.5%

The average curves obtained from the two samples are proposed below (**Figure 6.20**).

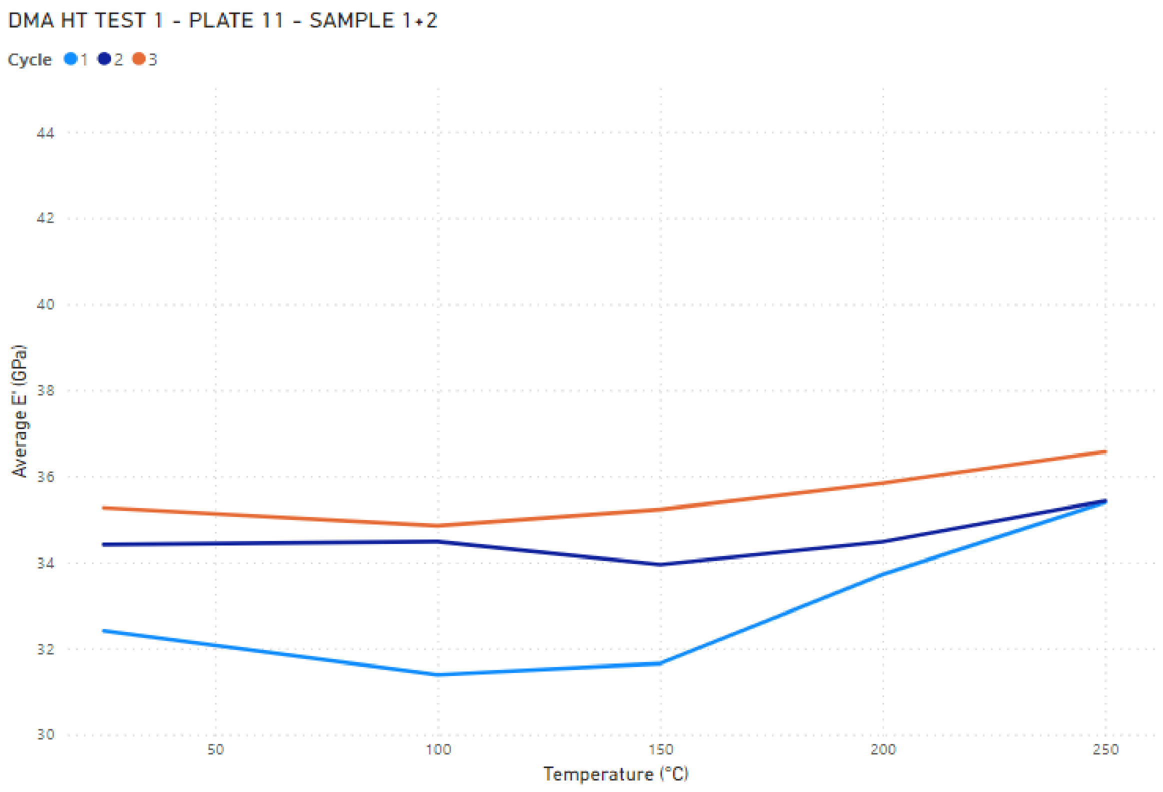

Figure 6.20. Average curves from TEST HT 1 applied to samples 1 and 2 of plate 11.

In the next chapter, we will discuss these results, comparing them with the temperature tests conducted using the IET system.

TEST HT 2: This test is based on the application of increasing load at a constant temperature. First, the furnace containing the sample is brought to the target temperature, and then a dynamic load gradient ranging from 20 to 50% of the failure load is applied. Three load cycles with unloading at the end of each cycle were applied to each sample, while keeping the target temperature constant throughout. To better understand this test, **Figure 6.21** below provides a schematic representation of the test.

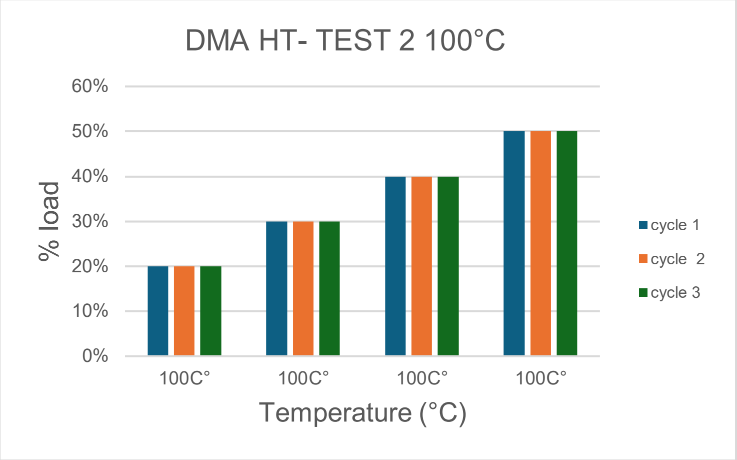

Figure 6.21. Schematic view of TEST HT 2 at 100°C.

For each target temperature (100 °C, 150 °C, 200 °C, 250 °C), two samples from the same plate were tested. This approach allows us to gather information on the effect of increasing load while the material is subjected to a specific temperature. Below are shown the graphs (**Figures 6.22-6.25**) and the corresponding tables (**Table 6.10-6.13**) where all the results of the TEST HT 2 conducted at 100 °C, 150 °C, 200 °C, 250 °C are presented. The curves in each graph, as well as the data tables, represent the average of the experimental values obtained from two different samples from the same plate.

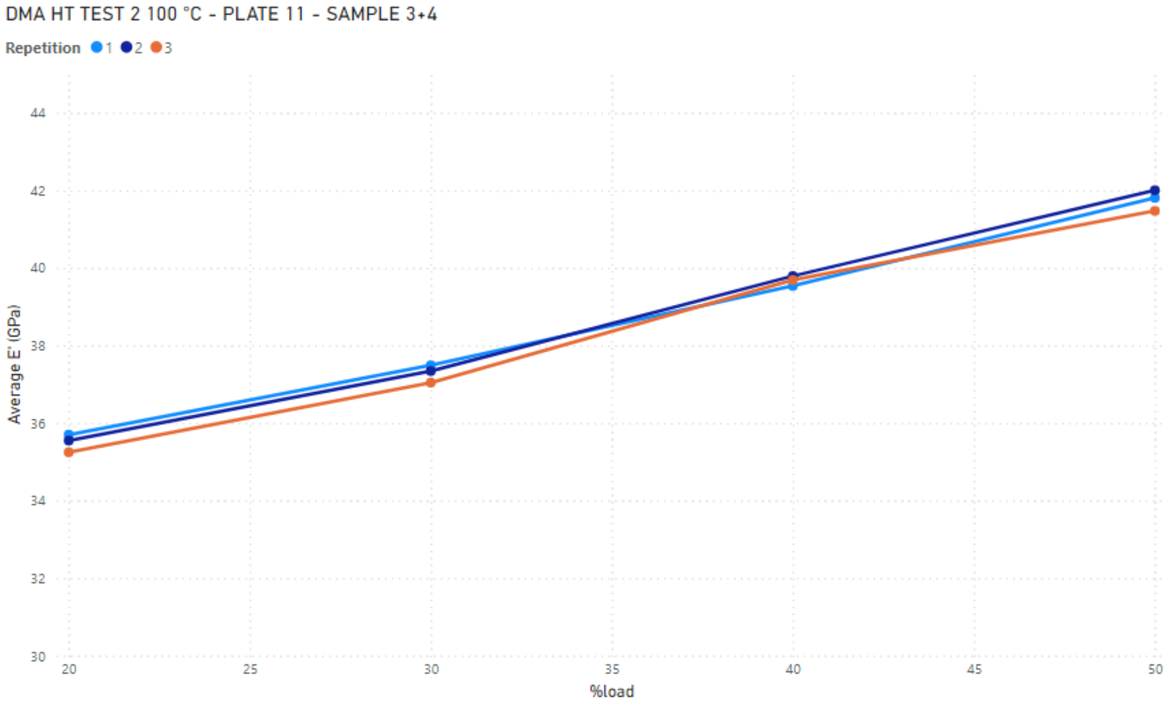

Figure 6.22. Average curves from TEST HT 2 - 100°C applied to samples 3 and 4 of plate 11.

Table 6.10. Results from TEST HT 2 - 100°C applied to samples 3 and 4 of plate 11.

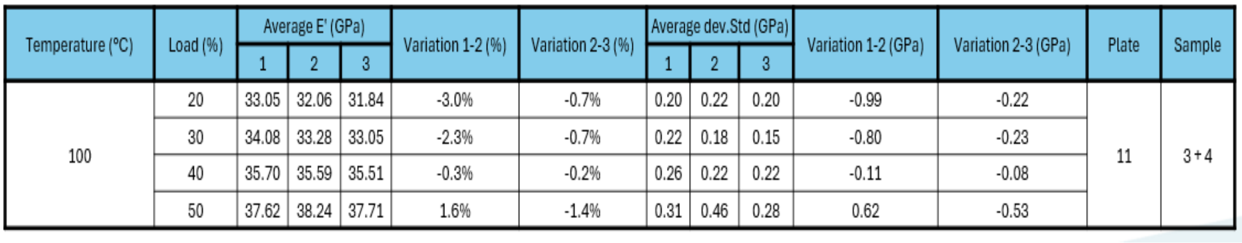

Temperature (°C)	Load (%)	Average E' (GPa)			Variation 1-2 (%)	Variation 2-3 (%)	Average dev.Std (GPa)			Variation 1-2 (GPa)	Variation 2-3 (GPa)	Plate	Sample
		1	2	3			1	2	3				
100	20	33.05	32.06	31.84	-3.0%	-0.7%	0.20	0.22	0.20	-0.99	-0.22	11	3+4
	30	34.08	33.28	33.05	-2.3%	-0.7%	0.22	0.18	0.15	-0.80	-0.23		
	40	35.70	35.59	35.51	-0.3%	-0.2%	0.26	0.22	0.22	-0.11	-0.08		
	50	37.62	38.24	37.71	1.6%	-1.4%	0.31	0.46	0.28	0.62	-0.53		

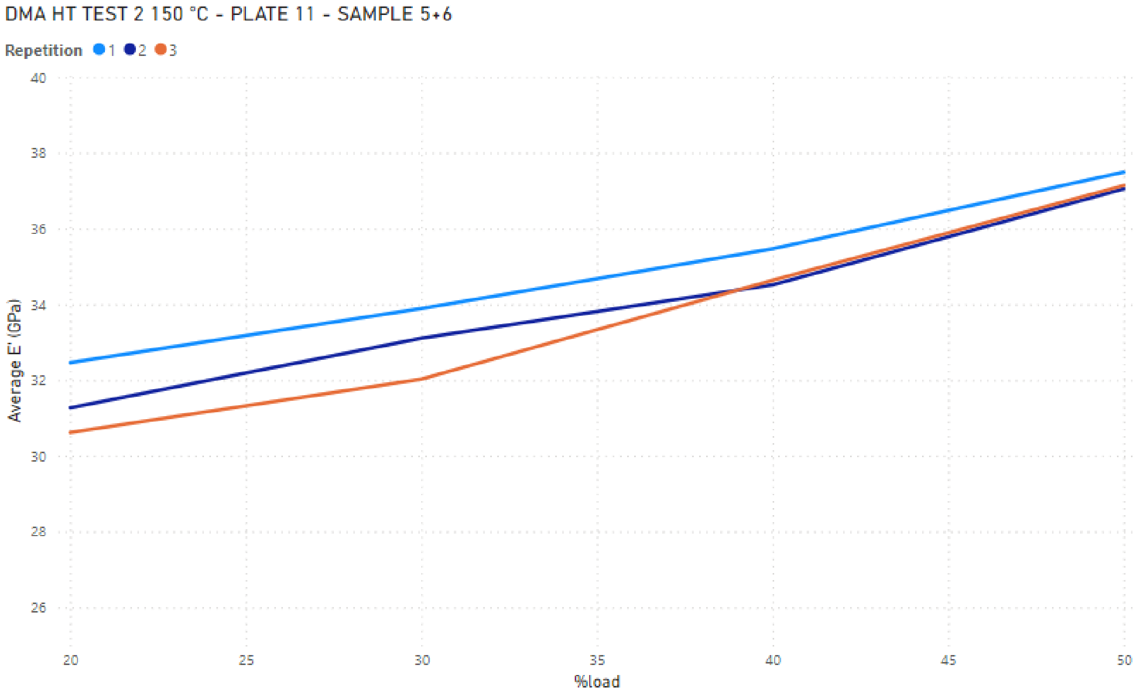

Figure 6.23. Average curves from TEST HT 2 - 150°C applied to samples 3 and 4 of plate 11.

Table 6.11. Results from TEST HT 2 - 150°C applied to samples 5 and 6 of plate 11.

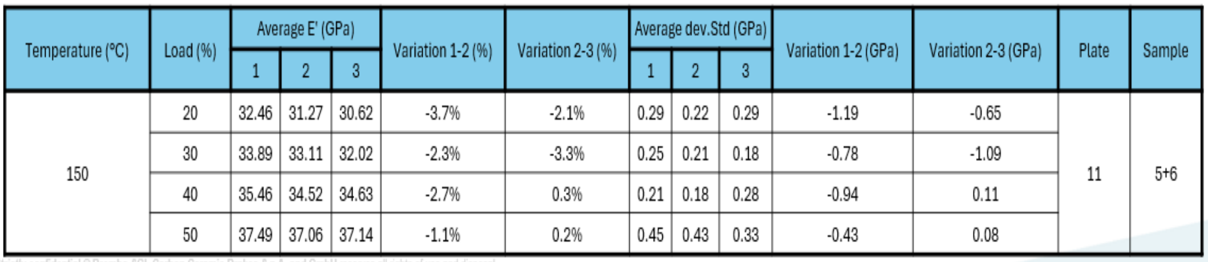

Temperature (°C)	Load (%)	Average E' (GPa)			Variation 1-2 (%)	Variation 2-3 (%)	Average dev.Std (GPa)			Variation 1-2 (GPa)	Variation 2-3 (GPa)	Plate	Sample
		1	2	3			1	2	3				
150	20	32.46	31.27	30.62	-3.7%	-2.1%	0.29	0.22	0.29	-1.19	-0.65	11	5+6
	30	33.89	33.11	32.02	-2.3%	-3.3%	0.25	0.21	0.18	-0.78	-1.09		
	40	35.46	34.52	34.63	-2.7%	0.3%	0.21	0.18	0.28	-0.94	0.11		
	50	37.49	37.06	37.14	-1.1%	0.2%	0.45	0.43	0.33	-0.43	0.08		

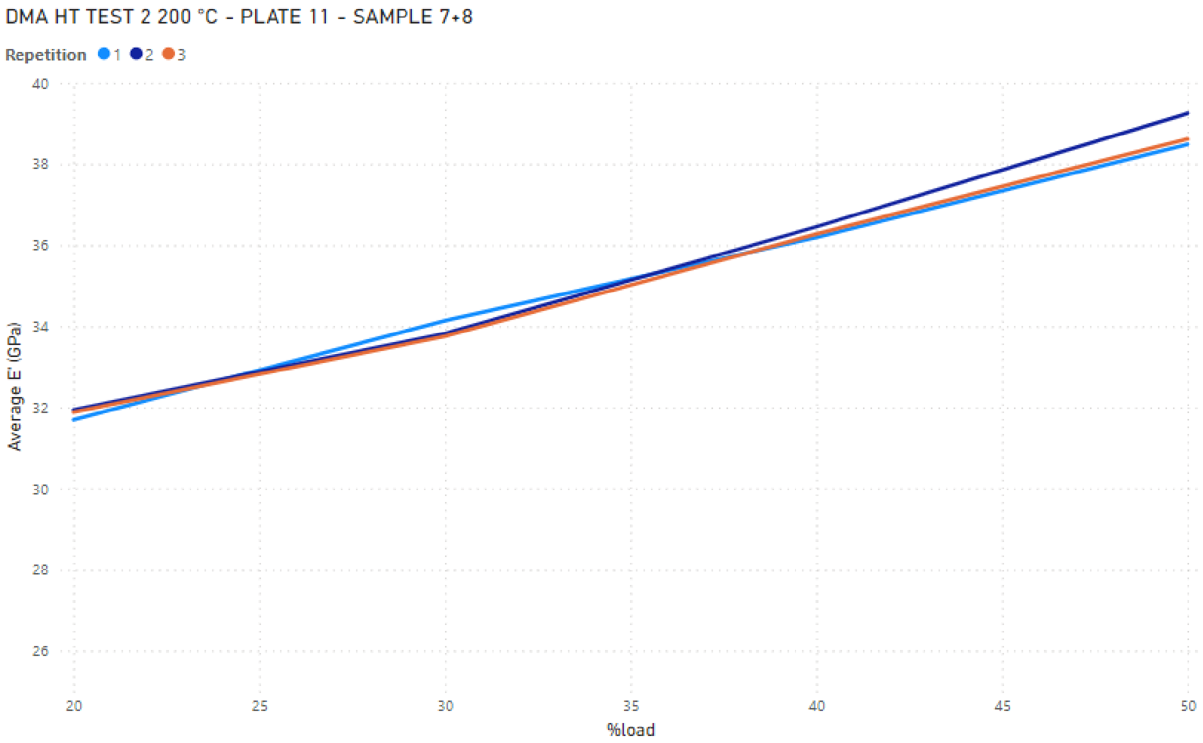

Figure 6.24. Average curves from TEST HT 2 - 200°C applied to samples 7 and 8 of plate 11.

Table 6.12. Results from TEST HT 2 - 200°C applied to samples 5 and 6 of plate 11.

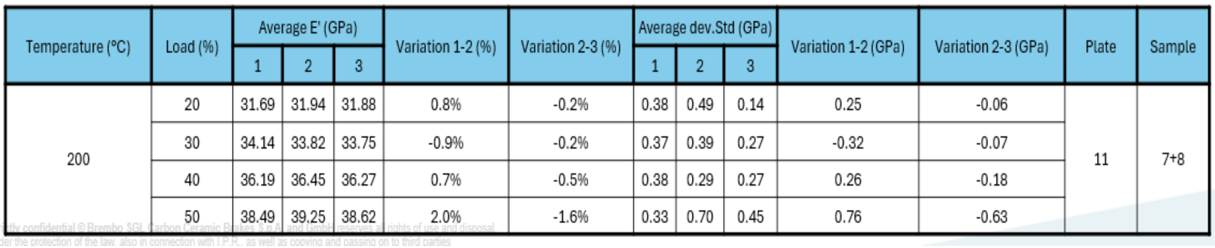

Temperature (°C)	Load (%)	Average E' (GPa)			Variation 1-2 (%)	Variation 2-3 (%)	Average dev.Std (GPa)			Variation 1-2 (GPa)	Variation 2-3 (GPa)	Plate	Sample
		1	2	3			1	2	3				
200	20	31.69	31.94	31.88	0.8%	-0.2%	0.38	0.49	0.14	0.25	-0.06	11	7+8
	30	34.14	33.82	33.75	-0.9%	-0.2%	0.37	0.39	0.27	-0.32	-0.07		
	40	36.19	36.45	36.27	0.7%	-0.5%	0.38	0.29	0.27	0.26	-0.18		
	50	38.49	39.25	38.62	2.0%	-1.6%	0.33	0.70	0.45	0.76	-0.63		

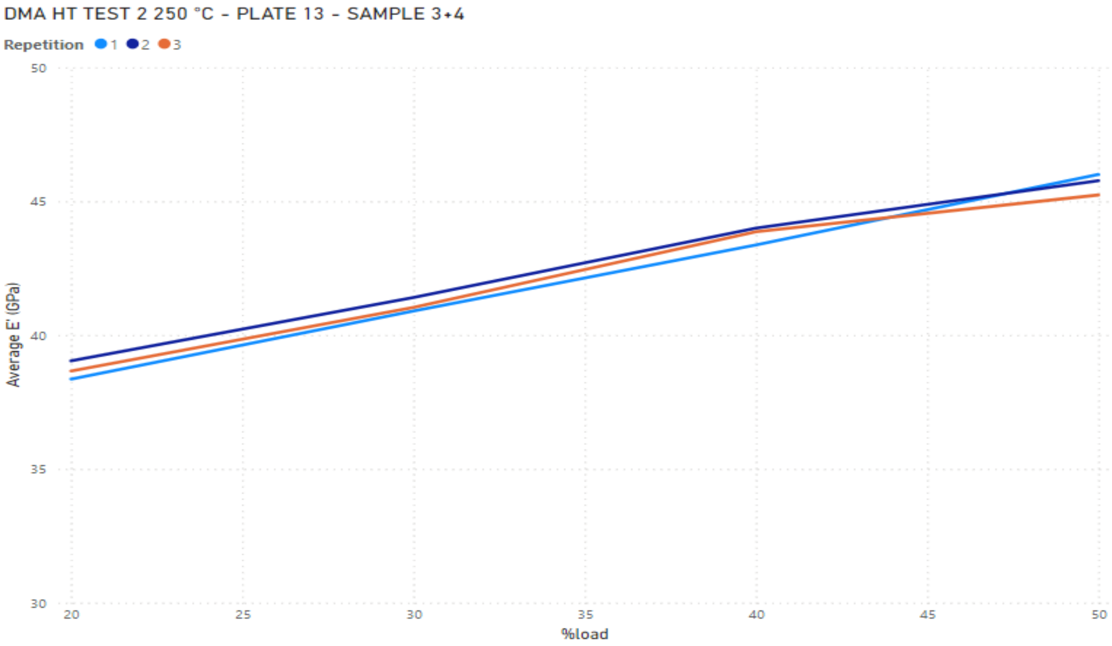

Figure 6.25. Average curves from TEST HT 2 - 250°C applied to samples 3 and 4 of plate 13.

Table 6.13. Results from TEST HT 2 - 250°C applied to samples 3 and 4 of plate 13.

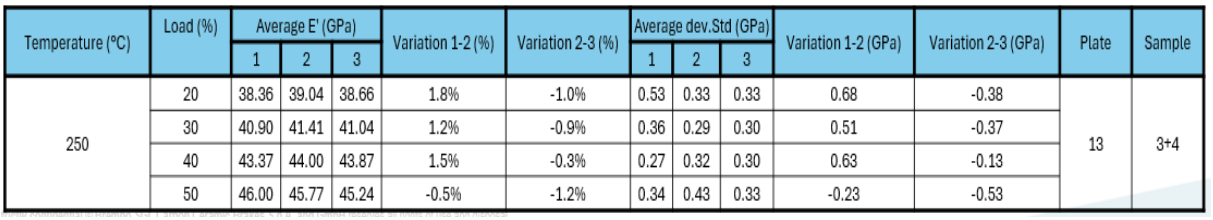

Temperature (°C)	Load (%)	Average E' (GPa)			Variation 1-2 (%)	Variation 2-3 (%)	Average dev.Std (GPa)			Variation 1-2 (GPa)	Variation 2-3 (GPa)	Plate	Sample
		1	2	3			1	2	3				
250	20	38.36	39.04	38.66	1.8%	-1.0%	0.53	0.33	0.33	0.68	-0.38	13	3+4
	30	40.90	41.41	41.04	1.2%	-0.9%	0.36	0.29	0.30	0.51	-0.37		
	40	43.37	44.00	43.87	1.5%	-0.3%	0.27	0.32	0.30	0.63	-0.13		
	50	46.00	45.77	45.24	-0.5%	-1.2%	0.34	0.43	0.33	-0.23	-0.53		

7. EXPERIMENTAL DATA DISCUSSION AND COMPARISON

7.1 ROOM TEMPERATURE DATA

To analyze the material behavior at room temperature, various testing methodologies were employed, compared below. Focusing on methods based on vibration frequencies, a comparison graph between Young's modulus data collected using IET tests with the RFDA system at the J-Tech@PoliTO (Politecnico di Torino), and those obtained using the system developed at the BSCCB laboratory, will be presented. Data from the RFDA system will be referred to as "IET POLI," and data from the BSCCB laboratory as "IET BSCCB." In **Figures 7.1** and **7.2** below, comparison graphs between IET POLI and IET BSCCB data for two different plates are presented, along with a summary of Young's modulus values obtained using the two methods.

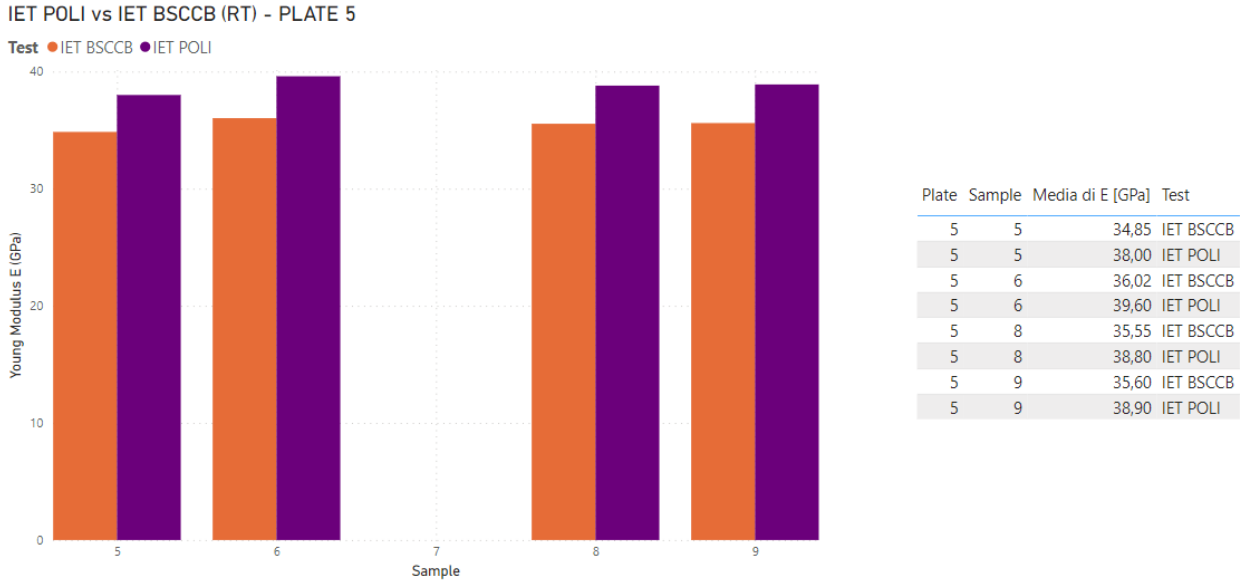

Plate	Sample	Media di E [GPa]	Test
5	5	34,85	IET BSCCB
5	5	38,00	IET POLI
5	6	36,02	IET BSCCB
5	6	39,60	IET POLI
5	8	35,55	IET BSCCB
5	8	38,80	IET POLI
5	9	35,60	IET BSCCB
5	9	38,90	IET POLI

Figure 7.1. Comparison of Young’s modulus data of plate 5 from IET POLI and IET BSCCB (RT).

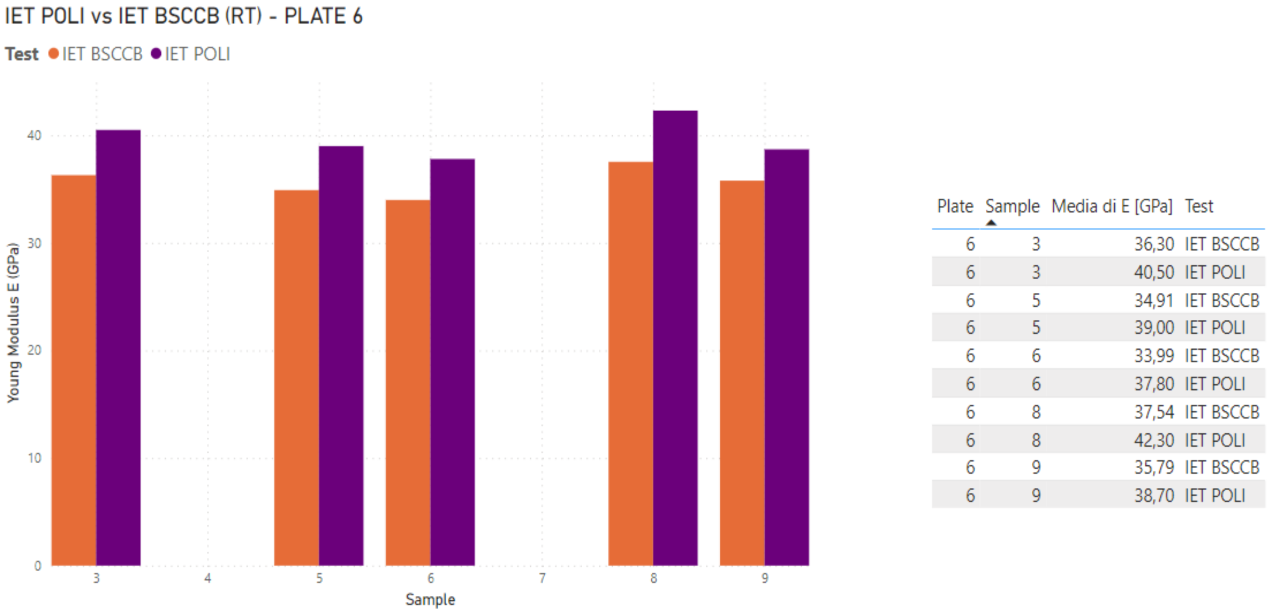

Plate	Sample	Media di E [GPa]	Test
6	3	36,30	IET BSCCB
6	3	40,50	IET POLI
6	5	34,91	IET BSCCB
6	5	39,00	IET POLI
6	6	33,99	IET BSCCB
6	6	37,80	IET POLI
6	8	37,54	IET BSCCB
6	8	42,30	IET POLI
6	9	35,79	IET BSCCB
6	9	38,70	IET POLI

Figure 7.2. Comparison of Young's modulus data of plate 6 from IET POLI and IET BSCCB (RT).

Below, the numerical variations between the modulus values for each sample of plates 5 and 6, collected through the two methods, are reported (**Table 7.1** and **7.2**).

Table 7.1. Difference and percentage variation of plate 5 Young modulus values taken from IET BSCCB and IET POLI.

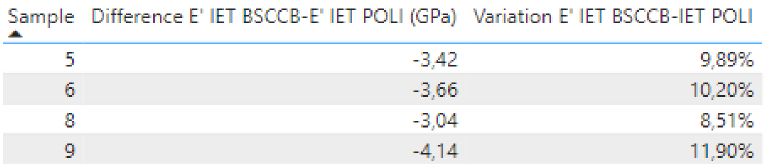

Sample	Difference E' IET BSCCB-E' IET POLI (GPa)	Variation E' IET BSCCB-IET POLI
5	-3,42	9,89%
6	-3,66	10,20%
8	-3,04	8,51%
9	-4,14	11,90%

Table 7.2. Difference and percentage variation of plate 6 Young modulus values taken from IET BSCCB and IET POLI.

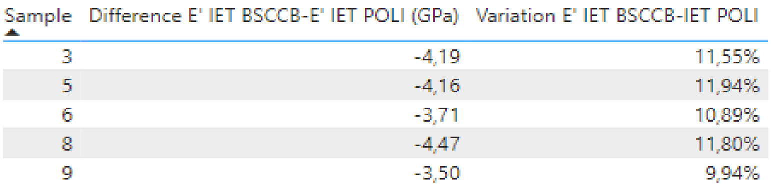

Sample	Difference E' IET BSCCB-E' IET POLI (GPa)	Variation E' IET BSCCB-IET POLI
3	-4,19	11,55%
5	-4,16	11,94%
6	-3,71	10,89%
8	-4,47	11,80%
9	-3,50	9,94%

As can be seen, the two experimental methods provide different modulus values, but always with a difference of 4 GPa, indicating the reliability of the individual systems as they provide values of the same order of magnitude. However, the overlap and equivalence of the two systems are not confirmed as they show values with a significant difference, around 10%. This difference in value is certainly related to the different nature of the acquisition systems of the two experimental methods; while the IET POLI system detects frequencies using a dedicated microphone, the IET BSCCB system detects them using accelerometers directly in contact with the sample. The hypothesis is that, while using a microphone, the vibration frequencies following the impact are not disturbed by any instrumentation, with the use of accelerometers instead, they can be dampened, resulting in less intense values compared to those detected with the IET POLI system setup. In fact, in the formula shown in **Figure 4.4**, used to calculate Young's modulus, it can be noted that it depends on the frequency raised to the second power; therefore, even a slight variation in this parameter can lead to significant differences in the final calculated modulus.

The other methods used to characterize the stiffness of the material at room temperature are based on the application of three-point bending stress on the sample both statically and dynamically. These tests will be referred to respectively as "3PB 20%" and "DMA 20%". To avoid damaging the material and thus obtaining a modulus value unaffected by the load, 20% of the material's rupture load shown in **Table 5.1** was used in both tests. The two tests return different quantities because with the dynamic test, the storage modulus is obtained, while with the static test, the Young's modulus is obtained. However, the material under study is mainly rigid, which excludes a viscoelastic behavior that could result in a difference between the two quantities. To compare different experimental methods, samples from plate 9 were tested both with the IET BSCCB method and with the DMA and 3PB tests. In **Figure 7.3** both a graphical comparison of the data collected from the different tests and a summary of the modulus values obtained are shown.

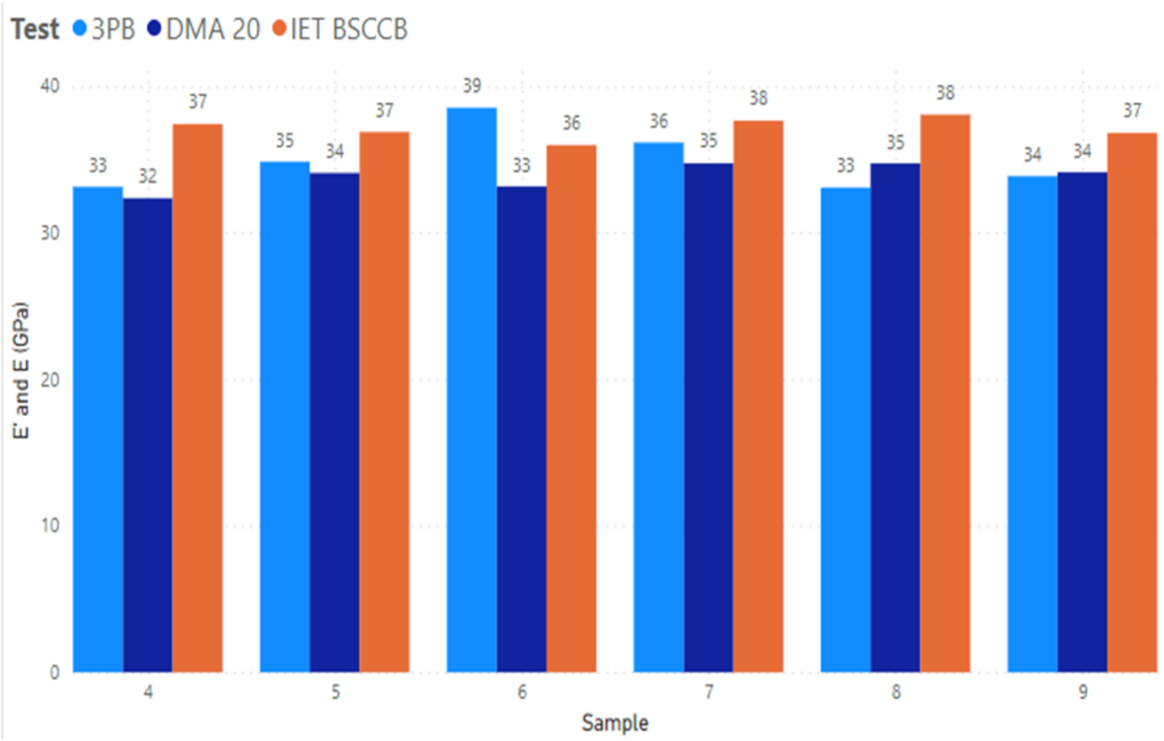

Figure 7.3. Comparison of E and E’ data of plate 9 from different experimental methods: 3PB 20%, DMA 20%, IET BSCCB (RT).

In the following table (**Table 7.3**), the values of E and E' obtained are collected.

Table 7.3. E and E’ values from a 3PB 20%, DMA 20%, IET BSCCB of plate 9 samples.

Sample	Average E - 3PB TEST (GPa)	Average E’ - DMA 20 (GPa)	Average E - IET BSCCB (GPa)
4	33.13	32.36	37.41
5	34.84	34.08	36.87
6	38.53	33.16	35.98
7	36.15	34.74	37.65
8	33.08	34.73	38.06
9	33.86	34.12	36.81

To analyze the differences between the methods, **Table 7.4** shows the variations between the data derived from them.

Table 7.4. Difference and percentage variation of E and E' values taken from IET BSCCB, 3PB 20% and DMA 20% of plate 9 samples.

Sample	Difference DMA 20%-IET BSCCB (GPa)	Variation DMA 20% - IET BSCCB (GPa)	Difference DMA 20%-3PB 20% (GPa)	Variation DMA 20%-3PB 20% (GPa)	Difference IET BSCCB-3PB 20% (GPa)	Variation IET BSCCB-3PB 20% (GPa)
4	-5.06	15,63%	-0.77	2,39%	4.28	-11,45%
5	-2.80	8,21%	-0.76	2,24%	2.03	-5,51%
6	-2.82	8,52%	-5.37	16,21%	-2.55	7,09%
7	-2.91	8,39%	-1.41	4,07%	1.50	-3,98%
8	-3.33	9,58%	1.65	-4,76%	4.98	-13,08%
9	-2.69	7,89%	0.26	-0,77%	2.95	-8,02%

As noted in **Figure 7.3**, the IET BSCCB tends to detect higher modulus values compared to the other methods, but always with a difference on the order of 4 GPa. This difference is also confirmed by another study on C/C-SiC composite materials [24]. In this article, a comparison was made with data from an RFDA machine, thus using the same IET test methodology conducted at the laboratories of the Polytechnic University of Turin, with those derived from static four-point bending tests applied to the same samples. The bending tests, measured values almost comparable, demonstrating that the mode of applying the load does not substantially influence the resulting modulus value. In summary, the application of both bending and impulse loads induces a slightly different response in the material, but the mode of applying the bending load is not influential.

To further validate the magnitude of the modulus variations obtained with the different methods, another type of material was also tested, a steel bar whose characteristics were described in **Chapter 5.2**. Below are presented: the comparison graph of the data (**Figure 7.4**), the summary of the modulus values (**Table 7.5**), and the differences between the obtained values (**Table 7.6**).

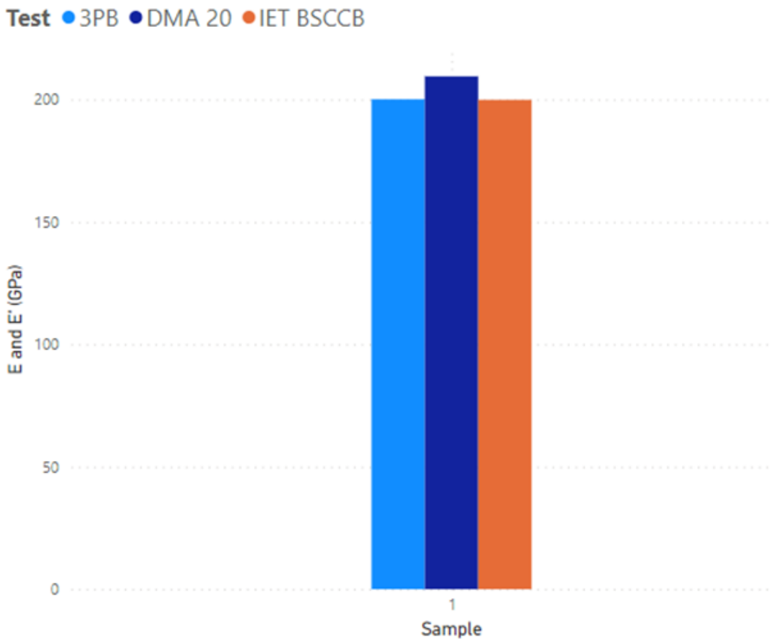

Figure 7.4. Comparison of E and E' data of a steel bar from different experimental methods: 3PB 20%, DMA 20%, IET BSCCB (RT).

Table 7.5. E and E' values from a 3PB 20%, DMA 20%, IET BSCCB of a steel bar.

Sample	Average E: 3PB TEST (GPa)	Average E': DMA 20 (GPa)	Average E: IET BSCCB (GPa)
1	200.10	209.50	199.89

Table 7.6. Difference and percentage variation of E and E' values taken from IET BSCCB, 3PB 20% and DMA 20% of a steel bar.

Sample	Difference DMA 20%-IET BSCCB (GPa)	Variation DMA 20% -IET BSCCB (GPa)	Difference DMA 20%-3PB 20% (GPa)	Variation DMA 20%-3PB 20% (GPa)	Difference IET BSCCB-3PB 20% (GPa)	Variation IET BSCCB-3PB 20% (GPa)
1	9.61	-4,59%	9.40	-4,49%	-0.21	0,10%

For the metal bar, it is noticeable that the variations between the three experimental methods are less significant compared to the case of the ceramic composite material. This is undoubtedly due to the different nature of the materials, as steel is a much more homogeneous material than the carbon ceramic composite. The composite material is undoubtedly more sensitive both to the experimental method used and to how it is carried out due to its strongly anisotropic nature and its close dependence on the arrangement of defects within each specific sample.

7.2 HIGH TEMPERATURE DATA

The high-temperature tests conducted on the carbon ceramic material under study show how it responds to the temperatures that can develop under operating conditions during braking. The temperature ranges studied (25-250 °C; 25-400 °C; 25-600 °C) were chosen to comprehensively analyze the material's response to different temperatures and derive useful information from it. Tests up to 250 °C were performed using both the IET technique and DMA technique, allowing the comparison of data sets derived from different experimental methods to verify that the material's behavior is consistent and independent of the testing methodology.

Comparing data from different experimental methods was not possible for other temperature ranges because the instrument for conducting DMA tests at high temperatures allowed temperatures up to 250 °C and not higher.

Comparing the data derived from the IET HT 250 °C tests and DMA HT TEST 1, it is observed that the material's behavior from room temperature up to 250 °C is confirmed by both experimental methods. Indeed, as can be seen from Figure 7.5, which presents the curves related to the data collected with the two different tests, the carbon ceramic material responds with an increase in stiffness as the temperature rises

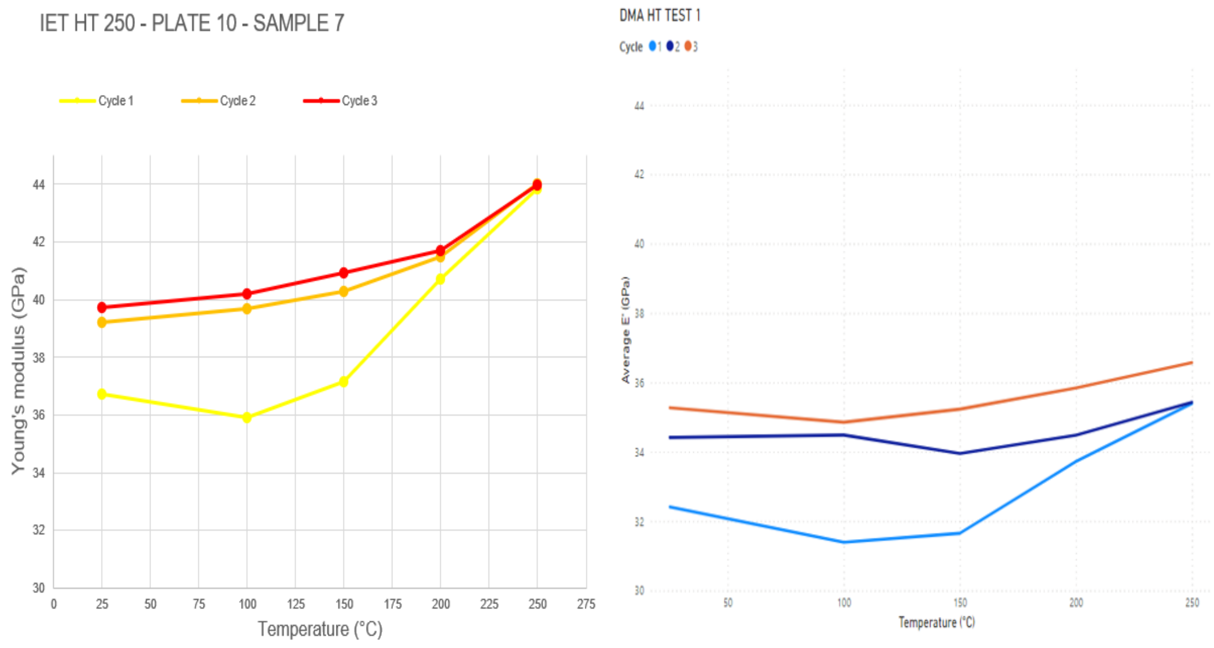

Figure 7.5. Comparison of E and E’ data of carbon ceramic samples from IET and DMA until 250 °C.

In addition, there is an increase in stiffness at the end of the thermal cycle; this is evident from the stiffness value measured at room temperature after the thermal cycle. In fact, for each thermal cycle, it is observed that the material starts with higher stiffness values compared to those of the previous cycle. The increase in stiffness with successive cycles becomes less significant until it levels off; indeed, as can be seen from **Figure 7.5**, the curves related to the second and third cycles overlap more than those between the first repetition and the second.

A hypothesis explaining this behavior is that during heating, the thermal expansion of the materials (C fibers and SiC matrix) present in the carbon ceramic sample tends to compact the structure, reducing the size of the internal porosity and inducing residual stress states of compression and tension that stiffen the structure.

However, the increase in the stiffness of the material's internal structure is limited, and already with the third repetition of the high-temperature test, there is a leveling of Young's modulus and storage modulus values. The only difference presented by the data collected with the two methods lies in the numerical value of the stiffness moduli, but this is due to the different instrumentation used, as previously stated in **Chapter 7.1** regarding room temperature tests.

As for the other IET HT tests up to 400 °C and 600 °C, different conclusions can be drawn from the results. As can be seen from the IET tests up to both 400 °C and 600 °C, the material exhibits a consistent behavior with increasing temperature. Referring to **Figures 4.30**, **4.31**, **4.32**, and **4.33**, it can be noted that the trend of the curve related to the first thermal cycle peaks around 350-400 °C, followed by a decrease up to 600 °C. The peak stiffness occurs around the temperature of 400 °C because at this temperature, the carbon fibers present in the sample start to to oxidize and degrade, contributing less to the reinforcement of the matrix. In fact, as reported in **Chapter 3.3.2**, during the production process of carbon-ceramic brake discs by Brembo Spa, an antioxidant treatment is provided specifically to limit the effect of fiber oxidation that would compromise the product. Unlike commercially sold brake discs, the samples used for this experimental study do not undergo this treatment and are therefore sensitive to this phenomenon starting from 400 °C.

Another conclusion that can be drawn from the experimental results is that once 400 °C is reached, the material is irreversibly damaged; in fact, both in tests up to 400 °C (**Figures 4.31-4.33**) and in those up to 600 °C (**Figure 4.30**), subsequent applications of thermal cycles start at lower values of E at room temperature. It can be noted that the decrease in Young's modulus after a cycle at 600 °C is much more significant than a cycle interrupted at 400 °C, as the material is subjected to higher temperatures, but in both cases, the sample is damaged.

Further analysis needs to be conducted regarding the trend of the curves for cycles after the first. Indeed, the graphs show a trend that deviates from the first cycle; while during the first test, the modulus curve shows a bell-shaped trend with a maximum around 400 °C, in subsequent tests, there is an increasing trend of the modulus even up to 600 °C. This behavior is difficult to interpret, but the most likely hypothesis is that the oxidation that occurred in the first cycle significantly increased the porosity inside the sample, allowing the material to compact and stiffen following thermal expansion with temperature constantly even beyond 250 °C and 400 °C. Furthermore, the damage between repetitions after the first is much less severe than that caused by the first application of the temperature gradient.

The high-temperature tests analyzed so far in this chapter aim to study the stiffness behavior of the material when subjected to a temperature gradient. With the DMA TEST HT 2, on the other hand, as mentioned in **Chapter 6.2.3**, the effect on the material of applying an increasing dynamic load at a constant temperature (from 100 to 250 °C) is analyzed.

Interesting information can be drawn from **Figures 6.21 - 6.24**. It can be noted how the effect of temperature and load compete with each other, and depending on the applied temperature, one tends to prevail over the other. In particular, it is observed how the damage caused by the application of a load cycle on the sample tends to decrease more and more as the temperature increases because it exerts a stiffening action that counteracts it. In fact, it is observed how at 100 and 150 °C, the load curves are shifted relative to each other towards lower storage modulus values with the progress of repetitions. At 200 °C, however, they are almost overlapping, indicating that at this temperature, the damage caused by the applied load is compensated by the stiffening effect of high temperature. Finally, once 250 °C is reached, the effect of temperature tends to prevail over the load, and therefore there is an increase in E' between load cycles.

This behavior is consistent with what has been observed in both room-temperature DMA tests, where successive applications of increasing load cycles result in material damage (TEST 1, **Chapter 6.2.1**), and in high-temperature tests where it has been observed that up to 250 °C, the material increases its stiffness (DMA TEST HT 1, **Chapter 6.2.2**; IET HT 250 °C, **Chapter 4.4.2**).

8. CONCLUSION

Based on the considerations drawn from the experimental data collected, it can be stated that the carbon ceramic material tends to change its behavior based on the conditions under which it operates, both in terms of external stresses applied to it and the temperature to which it is subjected. In particular, it has been observed that the temperature stiffens the material up to 250 °C, which allows it to counteract even the effect of dynamic loads up to 50% of its failure load. This behavior is highly compatible with the intended use in which carbon-ceramic brake discs operate. Indeed, during vehicle motion, the disc undergoes cyclic and dynamic loads from the brake pads during braking, which also leads to an increase in temperature due to friction. Therefore, temperature and cyclic loads are factors that operate simultaneously during the operational conditions of the brake disc, and it is interesting how these factors tend to balance out in this material up to 250 °C. Furthermore, by comparing data from different experimental methods, the validity and comparability of such methods have been demonstrated. In particular, this thesis demonstrates how with non-destructive tests based on vibration frequencies, like the system developed in the BSCCB laboratory (IET BSCCB), information on material stiffness comparable to that obtained with destructive tests such as three-point bending can be obtained. The main advantage of using such non-destructive methods lies in the reduction of material waste and consequent reduction in both production and disposal costs, in addition to the simplicity and speed of the experimental test, which also shortens analysis times. However, it must be considered that the material in question is a composite and therefore methods such as IET, which are based on frequencies, are still somewhat influenced by the strongly anisotropic nature of the material.

Leaving aside the considerations derived from the experimental tests, the carbon ceramic material under study generally possesses good thermal dissipation and high resistance to temperatures typical of ceramics, excellent mechanical resistance given by the combination of two very resistant materials such as SiC and carbon fibers, all combined with a low density that significantly reduces the weight of products made from such material. This makes this composite material highly performing and innovative for car brake disk applications. The main critical points, however, lie in the sensitivity to high-temperature oxidation of the carbon fibers, and it is essential to carry out antioxidant treatments to increase the operating range of the brake disc. The material in question has a very important ceramic part (the SiC matrix) and therefore is affected by the pronounced statistical nature of this category of materials. Indeed, they are materials that are very sensitive to the production process; each product and sample has a specific distribution of defects that results in a certain combination of properties. Over the years, more and more attention and innovation have been devoted to the production process to make the products as uniform as possible and consequently ensure products with similar properties. Brembo Spa has played a fundamental role in this, as over the years it has transformed a very promising idea into a top-quality product, making the company increasingly at the forefront of the braking systems sector.

BIBLIOGRAPHY

[1] - “Materiali compositi per l’ingegneria”, Claudio Badini, Celid, 2013, ISBN: 978-88-7661-992-2

[2] - https://vehiclecue.it/dischi-freno-carboceramici-brembo-prezzo-mtb/26000/

[3] - https://www.ade.pt/silicon-carbide/

[4] - Houyem Abderrazak and Emna Selmane Bel Hadj Hmida (2011). Silicon Carbide: Synthesis and Properties, Properties and Applications of Silicon Carbide, Prof. Rosario Gerhardt (Ed.), ISBN: 978-953-307-201-2

[5] - https://top-seiko.com/it/guide/graph/

[6] - https://chimicamo.org/chimica/grafite/

[7] - https://it.wikipedia.org/wiki/Poliacrilonitrile

[8] - http://www.sbai.uniroma1.it/~mauro.pasquali/page2/page9/page10/files/05-00.pdf

[9] - “Design, Fabrication, Characterization and Simulation of PIP-SiC/SiC Composites “, S. Zhao1, Zichun Yang, X.G. Zhou, X.Z. Ling4, L.S. Mora, D. Khoshkhou and J. Marrow, Tech Science Press, CMC, vol.42, no.2, pp.103-124, 2014

[10] - “Il manuale del disco freno”, Pompon Jean-Paul, Giorgio Nada, 09/1998, ISBN:8879111914

[11] - https://www.gommeblog.it/news-gomme-e-cerchi/9676/freni-carboceramici/

[12] - https://ledpro.it/tabella-conducibilita-termica-materiali-strisce-led/

[13] - https://web.archive.org/web/20120121153847/http://www.virtualcar.it/dischi-freni-carboceramici/

[14] - https://www.britannica.com/science/phenol-formaldehyde-resin

[15] - https://www.youtube.com/watch?v=3D9ayaGQiV4

[16] - https://www.brembo.com/it/auto/primo-impianto/prodotti/dischi-carbo-ceramici

[17] - RFDA HT1600 Manual, Installation - Operation Version 2.1, www.imce.net

[18] - J D Lord, R Morrel , “ Measurement Good Practice Guide No.98, Elastic Modulus Measurement”, 2007

[19] - ASTM E 1876-08, Standard Test Method for Dynamic Young’s Modulus, Shear Modulus, and Poisson’s Ratio by Sonic Resonance

[20] - ASTM C1161-02c, Standard Test Method for Flexural Strength of Advanced Ceramics at Ambient Temperature

[21] - BS ISO 6721-5:2019, Plastics — Determination of dynamic mechanical properties

[22] - Kevin P. Menard, Dynamic Mechanical Analysis: A Practical Introduction, 2ª ed., CRC Press, 2008

[23] - https://it.wikipedia.org/wiki/Controllo_PID

[24] - Honig S, Koch D, Weber S, et al. Evaluation of dynamic modulus measurement for C/C-SiC composites at different temperatures. *Int J Appl Ceram Technol*. 2019; 16:1723–1733. https ://doi.org/10.1111/ijac.13293